UNICA

UNIVERSITÀ
DEGLI STUDI
DI CAGLIARI

Ph.D. DEGREE IN
INDUSTRIAL ENGINEERING

Cycle XXXVIII

TITLE OF THE Ph.D. THESIS

Dynamic Modelling and Optimization of Hydrogen Refuelling Stations and Their Integration with Renewable Microgrids

Scientific Disciplinary Sector(s)

ING-IND/09

Ph.D. Student:	ROBERTA TATTI
Supervisor	MARIO PETROLLESE

Final exam: Academic Year 2024/2025
Thesis defence: February 2026 Session

Index of Contents

Index of Figures

Index of Tables

Abbreviations

Symbols

A	Area	[m^2]	P	Electric Power	[W]
c	Specific heat	[J/kg K]	Q	Heat transfer	[kW]
Cc	Cilinder Clearence	[-]	r	Radius	[m]
D	Diameter	[m]	R	Gas constant	[J/kg K]
DOD	Depth of Discharge	[-]	Ra	Rayleigh number	[-]
E	Energy	[Wh]	Re	Reynolds number	[-]
f	Derating Factor	[-]	SOC	State Of Charge	[%]
g	Gravity acceleration	[m/s^2]	t	Time	[h]
GI	Global Irradiance	[W/m^2]	T	Temperature	[K]
h	Enthalpy	[J/kg]	TCI	Total Capital Investment	[€]
HHV	Higher Heating Value	[kJ/mol]	u	Internal energy	[J/kg]
IR	Interest Rate	[%]	V	Volume	[m^3]
k	Heat transfer Coeff.	[W/m^2 K]	W	Electric Work	[W]
L	Length	[m]	Z	Compressibility factor	[-]
m	Mass	[kg]	γ	Temperature Coeff.	[-]
$\dot{m}$	Mass Flow Rate	[kg/s]	η	Efficiency	[-]
MM	Molar mass	[kg/mol]	λ	Thermal conductivity	[W/m K]
Nu	Nusselt number	[-]	μ	Dynamic viscosity	[Pa s]
OM	Operating/Maintenance	[€]	ρ	Density	[kg/m^3]
p	Pressure	[MPa]	τ	Isobaric expansion	[1/K]

Subscripts

BC	Battery Charge	*int*	Internal conditions
BD	Battery Discharge	*INV*	Inverter
BOP	Balance of Plant	*is*	Isentropic
BS	Battery Storage	*NOCT*	Nominal Operating Cell Temperature
C	Composite layer	*NOM*	Nominal Conditions
cum	Cumulative	*out*	Outside conditions
d	Hydrogen delivered	*STC*	Standard Test Conditions
EC	Engineering Cost	*TG*	To Grid
ext	External conditions	*v*	Volumetric
FG	From Grid	*y*	Years
H_2	Hydrogen	w	Tank Wall
in	Initial Conditions		

Acronyms			
APRR	Average Pressure Ramp Rate	LCOE	Levelized Cost of Energy
BEV	Battery Electric Vehicle	LCOH	Levelized Cost of Hydrogen
EMS	Energy Management Strategy	LPT	Low pressure tank
FCEV	Fuel Cell Electric Vehicle	PEC	Purchase Equipment Cost
GHG	Greenhouse Gases	PEM	Proton Exchange Membrane
GHI	Global Horizontal Irradiance	PG	Public Grid
HC	Hydrogen Compressor	PV	Photovoltaic
HG	Hydrogen Generator	SOC	State of Charge
HPT	High pressure tank	SSR	Self-Sufficiency Rate
HRS	Hydrogen Refueling Station	VT	Vehicle Tank
HT	Hydrogen Tank	WT	Wind Turbine
ICE	Internal Combustion Engine		

Abstract

The transport sector generates more than 20% of global CO_2 emissions, with road transport as the main contributor. The urgent need to reduce the environmental impact of mobility has promoted the development of sustainable vehicles, such us Battery Electric Vehicles (BEVs) and Fuel Cell Electric Vehicles (FCEVs). While BEVs have achieved widespread adoption, FCEVs are increasingly regarded as a viable alternative for heavy-duty applications thanks to their short refueling times and high gravimetric energy density. However, the implementation of FCEVs requires the design of efficient hydrogen refueling stations (HRS) capable of ensuring safe, fast, and complete refueling, in compliance with international protocols, such as SAE J2601-5.

In this context, this thesis presents a dynamic modelling of Hydrogen Refueling Stations modelling and their integration into optimized renewable microgrid, addressing both technical performance, techno-economic and environmental feasibility. The main objectives concern the development of comprehensive dynamic models of HRS (35 MPa and 70 MPa) and onboard Hydrogen Storage Systems (HSS) for heavy-duty vehicles (ensuring compliance with SAE J2601-5 safety protocols), the integration of HRS into renewable microgrids with multi-objective optimization (to minimize levelized cost of hydrogen (LCOH) while maximizing self-sufficiency ratio (SSR)) and the evaluation of techno-economic feasibility and environmental sustainability through comparative analysis of different energy management strategies and CO_2 emissions quantification.

In particular, the research is structured in three main investigations. The first investigation focuses on a 35 MPa HRS designed to supply an urban fleet of hydrogen buses. A validated Matlab-Simulink model (pressure and temperature prediction errors below 1% in hydrogen tanks) was developed, integrating all main HRS components (hydrogen tanks, compressor and pre-cooling units). A parametric analysis and a more realistic simulation were analysed. The parametric analysis identified optimal initial conditions to maximize consecutive refuelings in one hour (5÷8 refuelings with 3÷7 minute refueling times), while the realistic simulation, based on actual fleet demand and seasonal variations, demonstrated continuous station operability with 3÷4 minute refueling times throughout the year, maintaining compliance with SAE J2601-5 limits through adaptive thermal management strategies.

The second investigation focused on the integration of the 35 MPa HRS into a renewable energy microgrid. Three Energy Management Strategies (EMS) were analysed: Green EMS (100% renewable hydrogen production), Mixed EMS (combined renewable and grid production), and Grid EMS (grid-only production). Multi-objective optimization results showed initial LCOH values close to 25 €/kg (Green EMS) and higher than 23 €/kg (Mixed EMS) for 100% SSR. When accounting for surplus electricity sales at 0.137 €/kWh, costs decreased significantly to almost 17 €/kg for both EMS. Parametric analysis with projected electrolyser cost reductions indicated that renewable-based production could reach just a bit more than 11 €/kg by 2050, becoming more cost-competitive than grid-based production (close to 13 €/kg in the case study analysed). Environmental analysis revealed that FCEV adoption could reduce CO_2 emissions by 55% even

with grid-only hydrogen production, while Green EMS would achieve a 99% reduction compared to the current diesel fleet (36.84 kt CO_2/y).

The last investigation examines a 70 MPa HSS for heavy-duty vehicles, modelling the complete infrastructure from dispenser to onboard tanks. Different layouts were proposed, also varying the type of tank, to find the best solution to reduce refueling times. A comprehensive sensitivity analysis was conducted varying key parameters, such as APRR, dispenser and ambient temperatures, pipe length and diameter, tank type and number. Results identified Type III tanks as the best performing configuration (10.11 min refueling time, 221 g/s mass flow rate), with only minor differences compared to Type IV and V tanks (within one minute). The analysis demonstrated that increasing APRR and component diameters improved performance, while higher temperatures and longer pipes increased refueling times. A final compromise was found, in order not to exceed the limits of the SAE J2601-5 protocol.

This thesis is organized into four main chapters. Chapter 1 provides an overview of the role of hydrogen vehicles in greenhouse gas emission reduction; Chapter 2 presents the dynamic modeling and management of a Hydrogen Refueling Station (HRS); Chapter 3 addresses HRS integration into a renewable microgrid considering three Energy Management Strategies (EMS); Chapter 4 focuses on thermodynamic modeling and sensitivity analysis of a 70 MPa hydrogen storage system for heavy-duty vehicles.

1. The Role of Hydrogen Vehicles in GHG Emission Reduction

The global context of recent years has been increasingly marked by the effects of climate change, which are manifesting with growing intensity and frequency. The main causes of these changes are linked to rising CO_2 emissions, attributable to various sectors such as fossil fuel combustion, transportation, industry, buildings, deforestation, and intensive agriculture and livestock farming [1–3]. Specifically, in 2019, approximately 79% of global Greenhouses Gas (GHG) emissions came from the sectors of energy, industry, transport, and buildings together, while 22% from agriculture, forestry and other land use [4].

To mitigate the effects of climate change, the primary approach has been to reduce GHG emissions. In recent decades, significant international agreements have been reached int this regard: with the Kyoto Protocol (1997), industrialized countries committed to reducing emissions by 5.2% compared to 1990 levels in the period 2008–2012 [5]. Subsequently, with the Paris Agreement (2015), nearly all countries agreed to limit global warming well below 2°C, aiming ideally for 1.5°C [6]. In recent years, the Conferences of the Parties (COP) have progressively strengthened global climate commitments. COP26 (2021) called for a reduction in coal use and the elimination of inefficient fossil fuel subsidies [7]. COP27 (2022) established a loss and damage fund for vulnerable countries, while COP28 (2023) marked the first agreement explicitly mentioning a fossil fuel phase-out and a pledge to triple renewable energy capacity by 2030 [7]. More recently, COP29 (2024) introduced a new climate finance goal and finalized rules for international carbon markets. Looking ahead, COP30 (2025) is expected to drive more ambitious national climate plans and emphasize nature-based solutions and the energy transition [7].

One of the most significant indicators of the impact of climate change is the rise in the average global surface temperature. Figure 1.1 shows the observed temperature trend from 1900 to 2020, with projections up to 2100 relative to the 1850–1900 reference period.

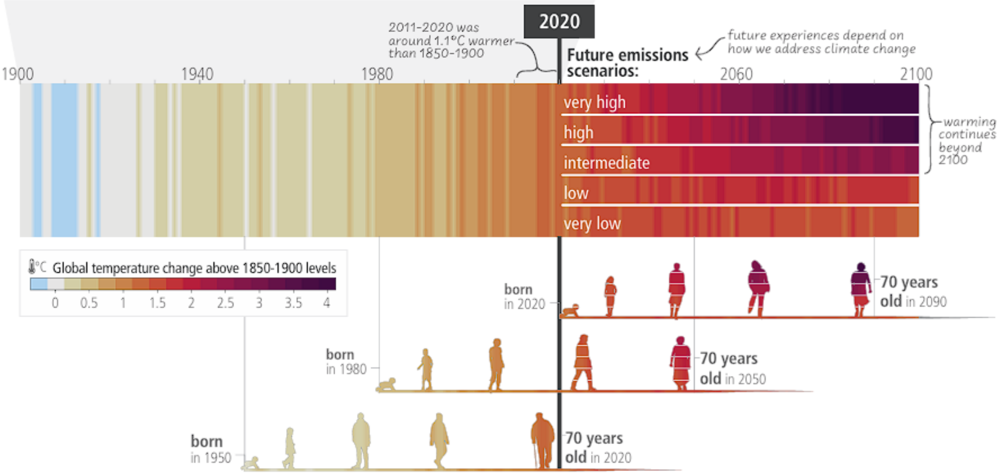

Figure 1.1 - Observed (1900–2020) and projected (2021–2100) changes in global surface temperature (relative to 1850-1900) [4].

The figure clearly illustrates that the climate has already changed, with an average increase of about +1.1°C compared to the pre-industrial era, and that this trend is expected to continue throughout the lives of three representative generations (1950, 1980, 2020). Future scenarios range from very high emissions (+4°C) to more optimistic ones, compatible with an increase limited to +1.5°C, in line with global goals. However, if no effective measures are taken to reduce emissions, intermediate or even high-emission scenarios are more likely.
The rise in temperature has significant consequences, particularly in three key areas: heat-humidity risks to human health, food production impacts, and risk of species losses, with particularly severe effects in developing countries [4]. Figure 1.2 illustrates how increasing temperatures will affect annual maximum temperature, average soil moisture, and wettest-day precipitation, always relative to the 1850–1900 period.

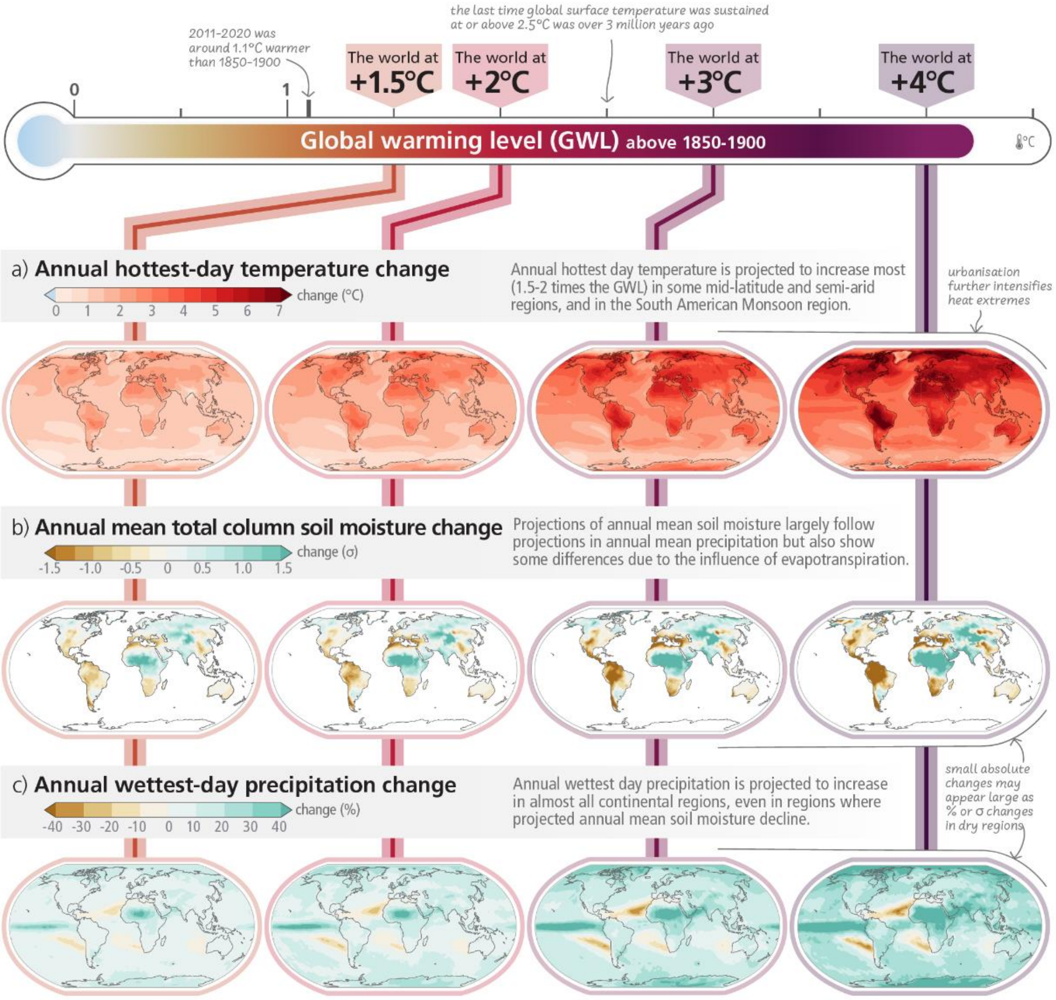

Figure 1.2 - Projected changes of annual maximum daily maximum temperature (a), annual mean total column soil moisture (b) and annual maximum 1-day precipitation (c) at global warming levels of 1.5°C, 2°C, 3°C, and 4°C relative to 1850–1900 [4].

Maximum daily temperatures are expected to rise sharply, especially in mid-latitude regions, semi-arid areas, and the South American monsoon region. Soil moisture will follow a similar trend, with some differences due to evapotranspiration. Wettest-day precipitation will increase across most continental regions, including those where average annual soil moisture is projected to decline.

These data highlight the urgent need to reduce GHG emissions, particularly CO_2, in order to limit future environmental impacts. In the following, a more detailed overview of GHG emissions at global, European and national level by sector is provided. Specifically, a comprehensive overview of the role of hydrogen vehicles in reducing greenhouse gas emissions is provided, starting with an analysis of global and regional greenhouse gas emissions and focusing on the transportation sector. Sustainable vehicle technologies are also examined, comparing battery electric vehicles (BEVs) and fuel cell electric vehicles (FCEVs), and hydrogen storage systems, refueling stations, and their integration into renewable microgrids are presented. Finally, the SAE J2601-5 protocol is introduced, laying the foundation for subsequent analyses, before describing the objectives of the thesis.

1.1 From global to regional GHG emissions

In 2023, GHG emissions reached 52.96 Gt of CO_2 equivalent, as illustrated in Figure 1.3. This represents a 28% increase compared to 2005 and a 62% rise since 1990 [8]. The sectors contributing most significantly to these emissions were power industry (14.95 Gt CO_2 eq./y) and industrial combustion and processes (11.37 Gt CO_2 eq./y). Other sectors, such as transport (8.5 Gt CO_2 eq./y), agriculture (6.45 Gt CO_2 eq./y), fuel exploitation (5.84 Gt CO_2 eq./y), buildings (3.69 Gt CO_2 eq./y), and waste (2.16 Gt CO_2 eq./y) are characterized by lower emissions. All sectors have experienced an increase in emissions since 1990 [8]. The power industry and industrial combustion and processes nearly doubled their emissions (over +90%), followed by the transport sector with a 78% increase. Fuel exploitation and waste saw more moderate increases (+48% and +56%, respectively), while agriculture and buildings registered smaller rises (+20% and +1%, respectively). Compared to 2005, emissions have also increased across all sectors, although to a lesser extent, ranging from +3% (buildings) to +41% (industrial combustion and processes).

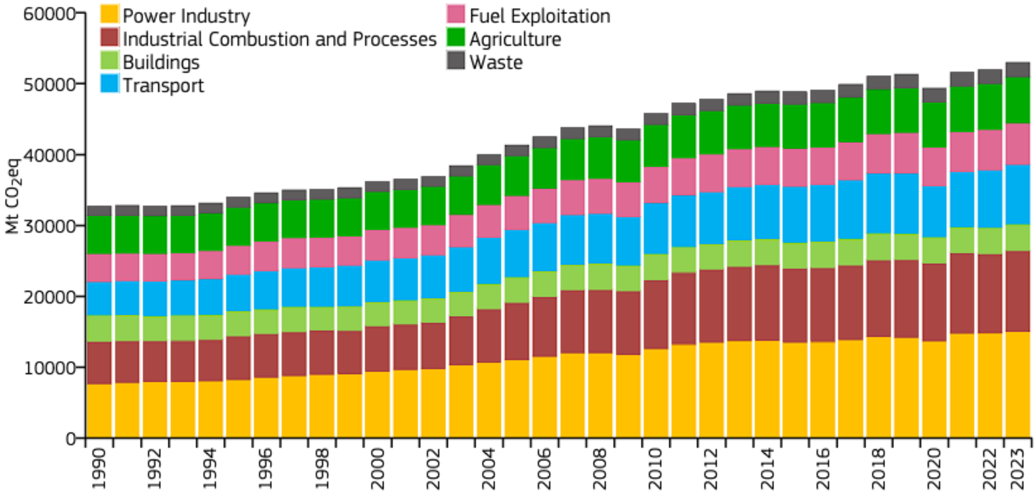

Figure 1.3 - Global GHG emissions per sector between 1990 and 2023 [8].

In contrast, Europe has seen a reduction in CO_2 equivalent emissions over the same period, as shown in Figure 1.4 [8]. Specifically, emissions decreased by 34% compared to 1990 and by 29% compared to 2005. In 2023, European emissions amounted to 3.22 Gt CO_2 eq./y, accounting for just over 6% of global emissions. The most impactful sectors were transport (776.77 Mt CO_2 eq./y), power industry (641.03 Mt CO_2 eq./y), industrial combustion and processes (610.86 Mt CO_2 eq./y), buildings (460.03 Mt CO_2 eq./y), agriculture (384.62 Mt CO_2 eq./y), fuel exploitation (196.08 Mt CO_2 eq./y), and waste (150.83 Mt CO_2 eq./y).

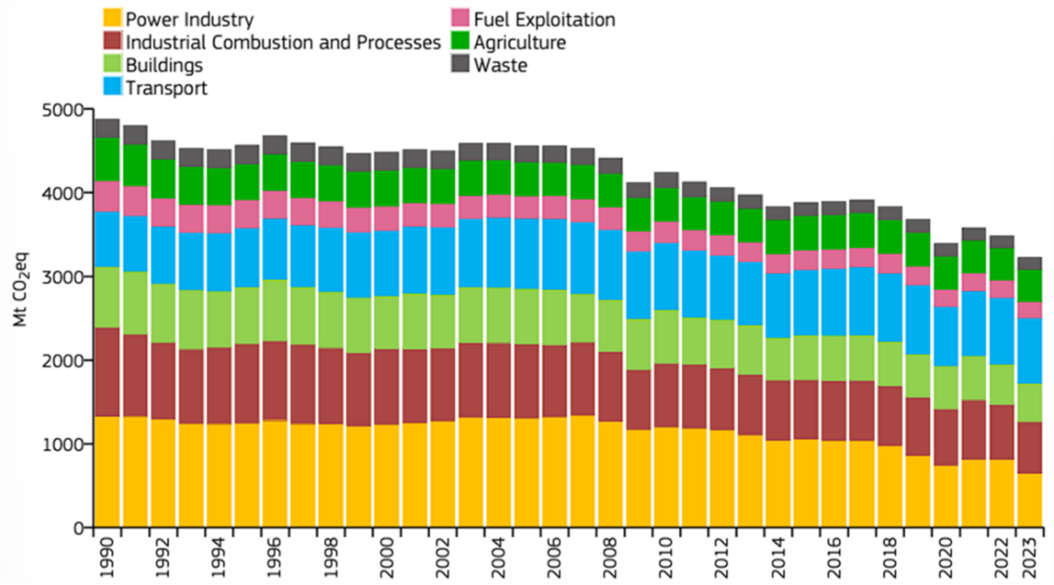

Figure 1.4 - European GHG emissions per sector between 1990 and 2023 [8].

Compared to 1990, only the transport sector saw an increase (+19%), while all other sectors experienced reductions ranging from -51% (power industry) to -27% (agriculture). When compared to 2005, emissions decreased across all sectors, with reductions between -50% (power industry) and -6% (transport and agriculture).

Italy followed a similar trend to Europe, with a decrease in CO_2 equivalent emissions, as shown in Figure 1.5 [8]. In 2023, emissions were 374.12 Mt CO_2 eq./y, representing 11.62% of European emissions and 0.71% of global emissions. This marks a 32% reduction compared to 1990 and a 47% decrease compared to 2005. Emission trends in Italy have fluctuated more noticeably, with significant drops in 1994, 2009 and 2020 (due to the COVID-19 pandemic). The most impactful sectors in 2023 were transport (103.83 Mt CO_2 eq./y), power industry (84.53 Mt CO_2 eq./y) and industrial combustion and processes (68.91 Mt CO_2 eq./y). Other sectors, such as buildings (55.13 Mt CO_2 eq./y), agriculture (30.32 Mt CO_2eq./y), fuel exploitation (16.54 Mt CO_2 eq./y) and waste (15.62 Mt CO_2 eq./y) impact less.

As in Europe, emissions in Italy decreased across all sectors except transport, which saw a 6% increase compared to 1990. Compared to 2005, all sectors experienced a reduction in emissions.

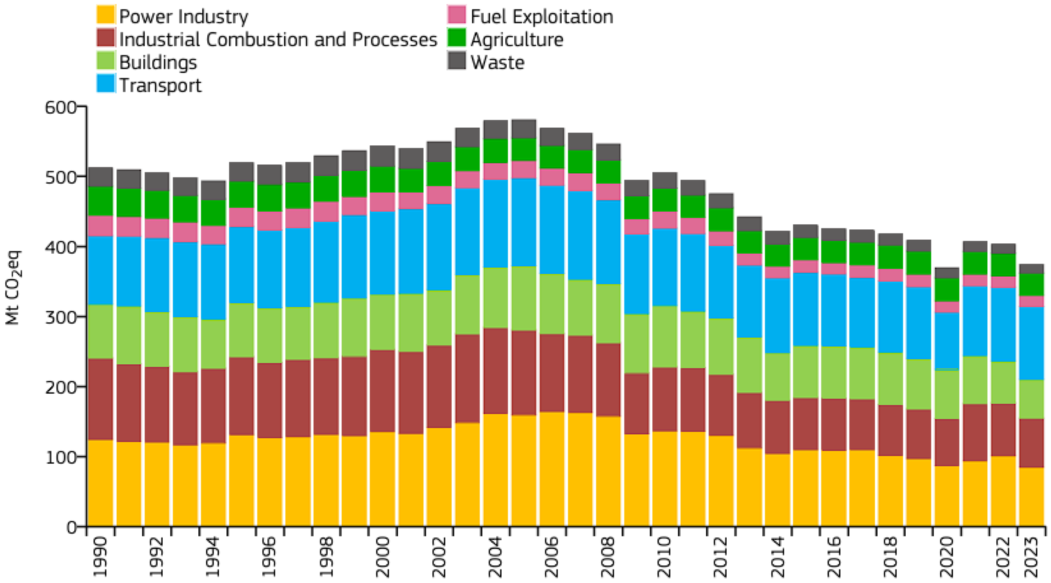

Figure 1.5 - Italy, San Marino and Vatican GHG emissions per sector between 1990 and 2023 [8].

At the regional level, Sardinia reported its most recent emissions data in 2021, with a total of 17.43 Mt CO_2 eq./y [9], accounting for 4.66% of Italy's emissions, 0.54% of Europe's, and 0.033% of global emissions. Sardinia also followed the national and European trend of decreasing emissions, with a 15.56% reduction compared to 1990 and a 36.84% decrease compared to 2005 [9]. The most impactful sectors in 2021 were the energy sector (13.53 Mt CO_2 eq./y [10]), non-road transport (2.91 Mt CO_2 eq./y [11]) and agriculture (2.19 Mt CO_2 eq./y [12]).

Among the sectors most responsible for emissions, transport plays a particularly significant role. This is illustrated in detail in the following sections, which provide a detailed overview of emissions in this sector and by type of vehicle.

1.2 Focus on GHG emissions from the transport sector

Focusing on the transport sector, emissions in 2023 amounted to 8.5 Gt CO_2 eq./y globally (16.05%), 776.77 Mt CO_2 eq./y in Europe (24.12%), and 103.85 Mt CO_2 eq./y in Italy (27.7%). As reported previously, in both Europe and Italy transport was the sector responsible for the highest share of GHG emissions.

Emissions by vehicle type are illustrated in Figure 1.6, which shows global (left) and European (right) transport emissions trends from 1990 to 2019. Globally, emissions rose from 5.1 Gt CO_2 eq./y in 1990 to 8.9 Gt CO_2 eq./y in 2019, before slightly decreasing to 8.5 Gt in 2023, as reported by [8]. Road transport account for 69% of these emissions, followed by aviation and maritime transport, each contributing around 11% when combining international and domestic categories.

In Europe, emissions increased from 0.94 Gt eq./y in 1990 to 1.12 Gt CO_2 eq. in 2019, then declined to 0.777 Gt CO_2 eq./y in 2023 [13]. Road transport was even more dominant in Europe, responsible for 86.93% of emissions.

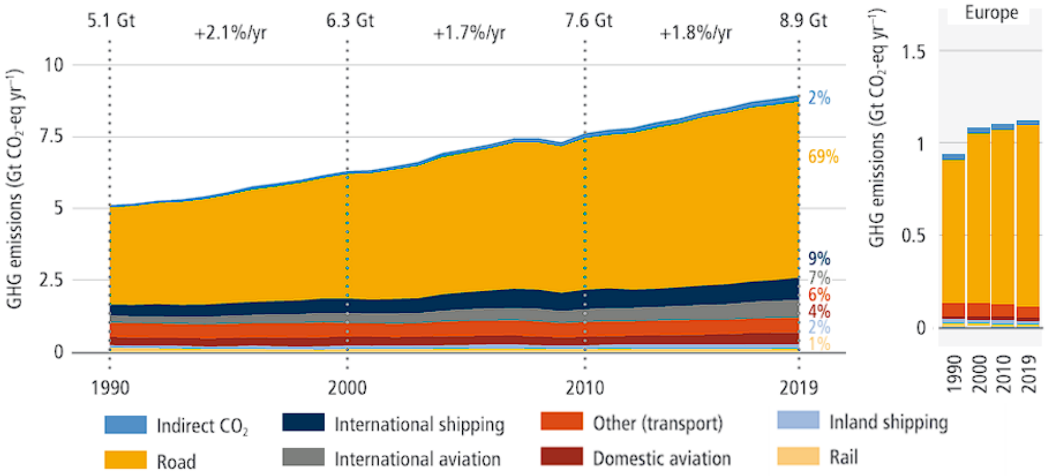

Figure 1.6 - Global (left) and European (right) transport GHG emissions trend by type of vehicle [13].

In Italy, more recent data from 2023 are available (Figure 1.7). Road transport emissions reached approximately 100 Mt CO_2 eq./y, with passenger cars contributing for 63.9%, followed by heavy-duty commercial vehicles (20.1%) and light-duty commercial vehicles (10.7%). Aviation accounted for 2.37 Mt CO_2 eq./y in 2023, up from 1.15 Mt in 1990, while maritime transport emitted 4.72 Mt CO_2 eq./y, down from 5.53 Mt in 1990. The total emissions from all transport modes in Italy amounted to 107.09 Mt CO_2 eq./y, slightly exceeding the values reported by [8], suggesting that some minor categories may have been excluded in their analysis. Road transport remained the most impactful, responsible for 93.38% of emissions.

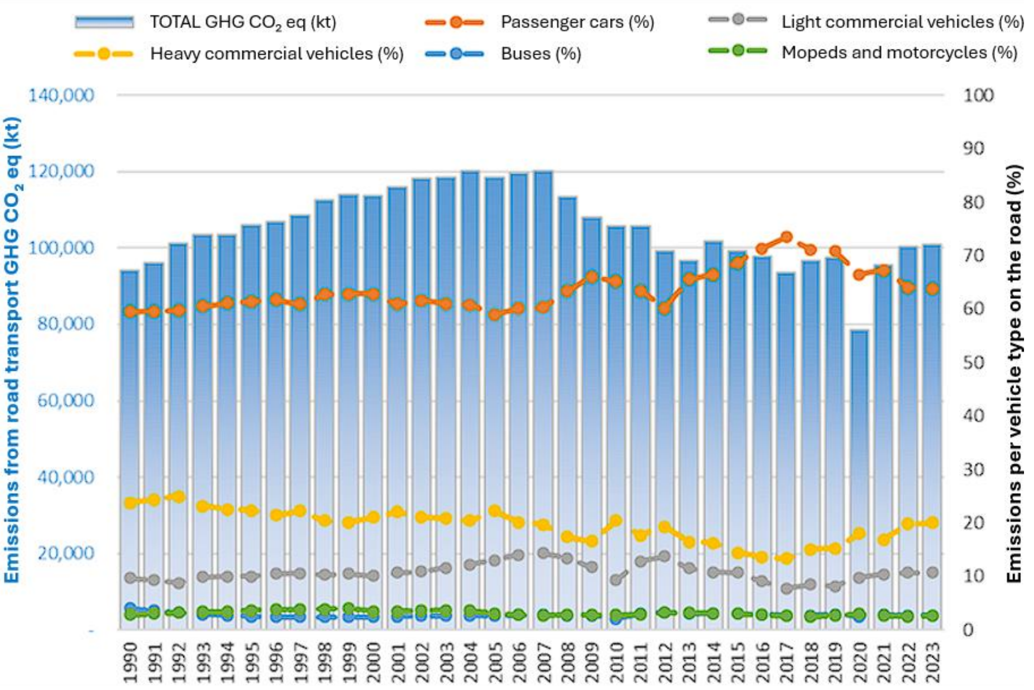

Figure 1.7 - Italian transport GHG emissions by type of vehicle from 1990 to 2023 [14].

Given the significant share of emissions from the transport sector (16% globally, 24% in Europe, and 27.7% in Italy) and the international commitments to reduce GHG emissions, substantial investments are being directed toward decarbonizing this sector.

At the European level, initiatives such as the Green Deal [15] and the RePowerEU [16] program have led to major investments aimed at reducing transport emissions. The European Investment Bank has allocated an average of €11 billion annually to sustainable mobility projects [17], with a strong focus on rail and urban transport. Additionally, €37 billion have been earmarked for biogas development and €27 billion for hydrogen, targeting hard-to-decarbonize sectors like aviation and maritime transport.

In Italy, the National Recovery and Resilience Plan (PNRR) [18] has allocated over €32 billion to sustainable mobility, rising to almost €62 billion when other funds are also considered [19]. This includes the construction of new high-speed rail lines, electrification of regional networks, procurement of thousands of electric and hydrogen-powered buses, and the development of 1 800 km of cycling infrastructure. These investments span infrastructure, vehicles, and technological innovation, marking a concrete step toward ecological transition in transport.

According to the International Energy Agency (IEA), all these efforts are expected to reduce transport emissions from 8.2 Gt CO_2 eq./y to approximately 0.9 Gt CO_2 eq./y, as shown in Figure 1.8. The figure also outlines projected phase-out dates for various vehicle categories: two- and three-wheelers by 2040, rail transport by 2050, light commercial vehicles by 2055, and cars, buses, and minivans by 2070. Aviation, maritime transport, and medium/heavy trucks are expected to remain the only significant sources of emissions due to the challenges in decarbonizing these modes.

In this context, characterized by the significant impact of the transport sector on global emissions, it is essential to explore sustainable alternatives to conventional vehicles. This will also make it easier to achieve the emissions reduction targets envisaged by the IEA, previously explained. An overview of electric vehicles will then be provided, distinguishing between Battery Electric Vehicles (BEVs) and Fuel Cell Electric Vehicles (FCEVs).

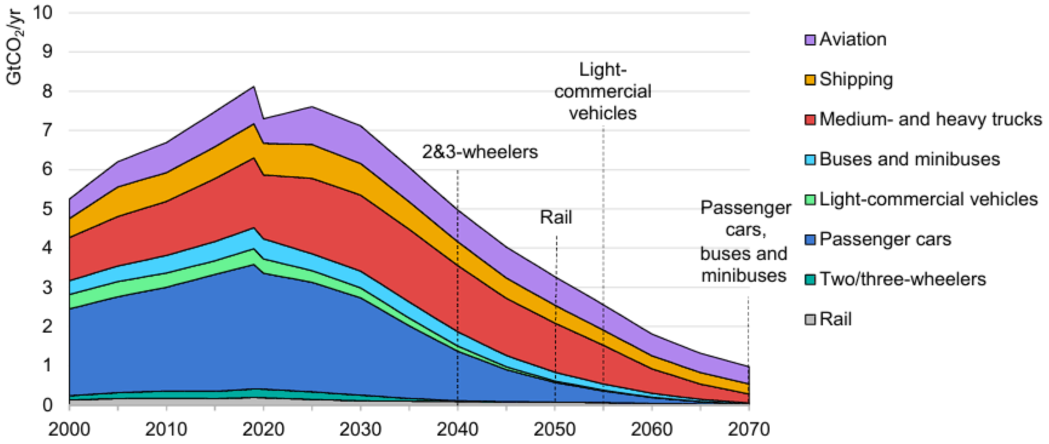

Figure 1.8 - Global CO_2 emissions in transport by mode in the Sustainable Development Scenario [20].

1.3 Sustainable vehicles overview: BEV and FCEV

In light of the urgent need to reduce GHG emissions and the substantial investments being made, particularly in the transport sector, it is clear that alternatives to conventional Internal Combustion Engine (ICE) vehicles must be developed and adopted. Currently, the vast majority of vehicles worldwide still rely on ICE, as shown in Figure 1.9 for light-duty vehicles. In 2022 diesel vehicles dominate the market (approximately 64%), followed by petrol vehicles (11%). However, in recent years both categories have seen a slight decline in favour of more sustainable options, such as BEVs (10%) and hybrids (12%).

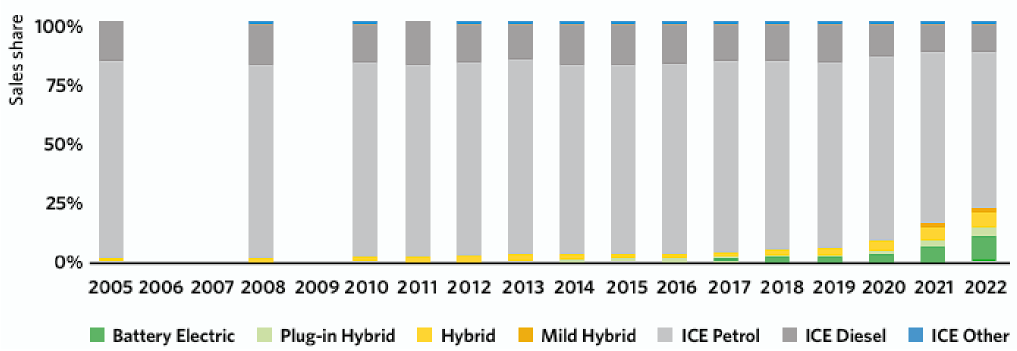

Figure 1.9 - Global Light Duty Vehicles sales shares by powertrain [21].

This trend is also evident in Europe and Italy, where ICE vehicles remain predominant. As shown in Table 1.1, ICE vehicles represent over 90% of all vehicle types in Europe, and similarly high percentages are also recorded in Italy, with the exception of passenger cars. In fact, hybrid vehicles represent around 4% of cars in Italy, while the European average is slightly lower at 3%. BEVs are most prevalent among buses in both regions. Notably, Italy has a higher share of gas-powered vehicles compared to the European average.

Table 1.1 - Percentage of vehicle type by power source in Italy and Europe in 2022 [22].

	Petrol	**Diesel**	**Battery electric**	**Plug-in hybrid**	**Hybrid electric**	**Natural gas**	**LPG**	**Other**	**Unknown**
Car (40 213 061 units in ITA, 252 237 775 units in EU)									
ITA	44.0%	42.1%	0.4%	0.0%	3.9%	2.4%	7.2%	0.0%	0.0%
EU	50.6%	40.8%	1.2%	1.0%	3.1%	0.6%	2.6%	0.1%	0.1%
Vans (4 403 430 units in ITA, 30 191 188 units in EU)									
ITA	4.8%	90.3%	0.3%	0.0%	0.8%	2.2%	1.5%	0.0%	0.0%
EU	5.9%	90.7%	0.8%	0.02%	0.3%	0.6%	0.8%	0.03%	1.0%
Trucks (969 488 units in ITA, 6 451 695 units in EU)									
ITA	0.7%	98.2%	0.0%	0.0%	0.0%	0.7%	0.2%	0.1%	0.0%
EU	0.7%	96.0%	0.1%	0.01%	0.05%	0.8%	0.1%	0.1%	2.3%
Buses (100 014 units in ITA, 720 783 units in EU)									
ITA	0.4%	92.7%	0.8%	0.0%	0.4%	5.4%	0.2%	0.1%	0.0%
EU	0.5%	90.5%	1.9%	0.1%	2.0%	4.1%	0.1%	0.1%	0.8%

As illustrated in Figure 1.9, sustainable vehicles have begun increase in recent years. Referring to electric vehicles, these are typically categorized into two main types: BEVs and FCEVs [23–25]. While both are emission-free during operation [23–25], they differ in how energy is stored and delivered. BEVs rely on batteries to supply electricity directly to the motor, whereas FCEVs use hydrogen, usually stored at high pressure, which is converted into electricity via fuel cells [23–25].
A generic scheme of the key components for both BEVs and FCEVs is reported in Figure 1.10 e Figure 1.11, respectively. As shown, BEVs are powered entirely by a large traction battery that supplies energy to one or more electric motors. They require connection to an external power source, either a wall outlet or dedicated charging infrastructure, known as Electric Vehicle Supply Equipment (EVSE), to recharge. Since BEVs operate solely on electricity, they produce zero tailpipe emissions and do not include conventional fuel system components such as a fuel tank, fuel line, or fuel pump. The key components are the batteries, charge port, DC/DC converter, electric traction motor, onboard charger, power electronics controller, thermal system (cooling), traction battery pack and transmission [26].

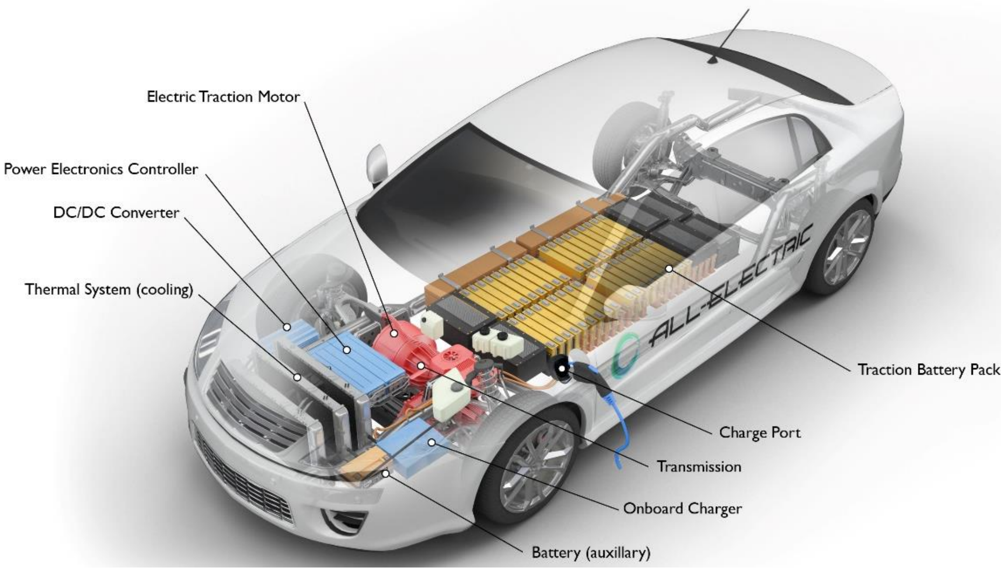

Figure 1.10 - Key components of a Battery Electric Vehicle [26].

Regarding FCEVs, they use electricity to drive an electric motor, but unlike battery electric vehicles, they generate this electricity onboard through a hydrogen-powered fuel cell rather than relying solely on stored battery energy. Vehicle performance depends on the combined sizing of the fuel cell, electric motor, and auxiliary battery. The battery primarily assists by recovering braking energy, providing additional power during acceleration, and stabilizing the energy supply, allowing the fuel cell to idle or shut down when demand is low. The vehicle’s energy capacity is determined by the size of its hydrogen tank, unlike BEVs, where both power and range depend directly on battery size. The main components distinguishing FCEVs from BEVs are the fuel cell stack, hydrogen storage tank, and fuel filler, which substitute the onboard charger, charge port, and large traction battery pack typically found in BEVs [27].

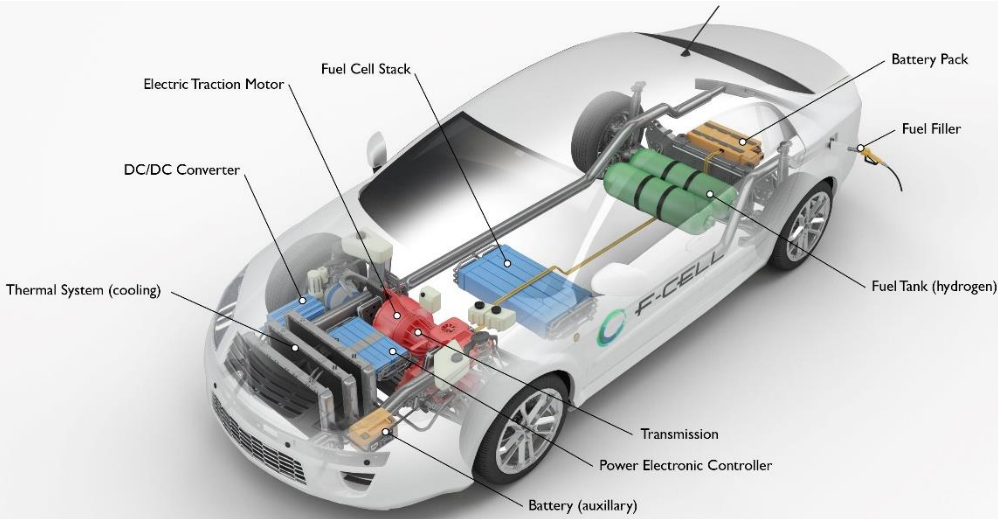

Figure 1.11 - Key components of a Fuel Cell Electric Vehicle [27].

The growth of electric vehicles is reflected in IEA data for both FCEVs and BEVs. FCEVs increased from approximately 20 000 units in 2018 to around 100 000 units in 2024 (Figure 1.12), with passenger cars leading the segment, followed by trucks, buses, and vans. The highest adoption rates are found in Asian countries (particularly South Korea, China, and Japan), followed by the United States and Europe. BEVs have experienced even more rapid growth.

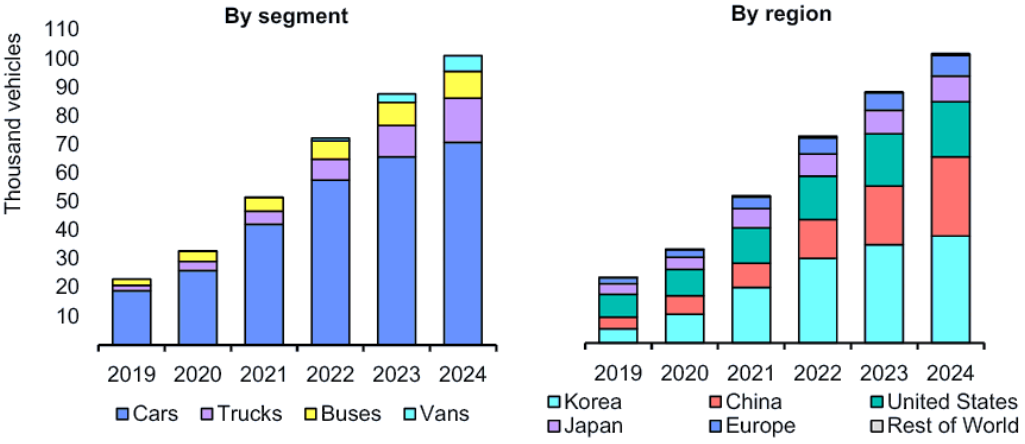

Figure 1.12 - Fuel cell electric vehicle stock by segment and region (2019-2024) [28].

Regarding BEVs, as shown in Figure 1.13, global electric car sales surged from 363 000 units in 2014 to 17.46 million in 2024. When combining BEVs and plug-in hybrids, China emerges as the leading market, followed by Europe and the United States. Heavy-duty electric vehicles, such as buses and trucks, followed a different trajectory (Figure 1.14). Both categories, in fact, saw a decline from 2018 to 2021, followed by a growing. Interestingly, the total number of electric buses decreased overall, from a peak of around 90 000 units in 2017 to 71 456 units in 2024, while electric truck numbers rose to 93 398 units in 2024. The regional distribution for both vehicle types is the same of passenger cars: China is characterized by the highest prevalence, followed by Europe, and the United States.

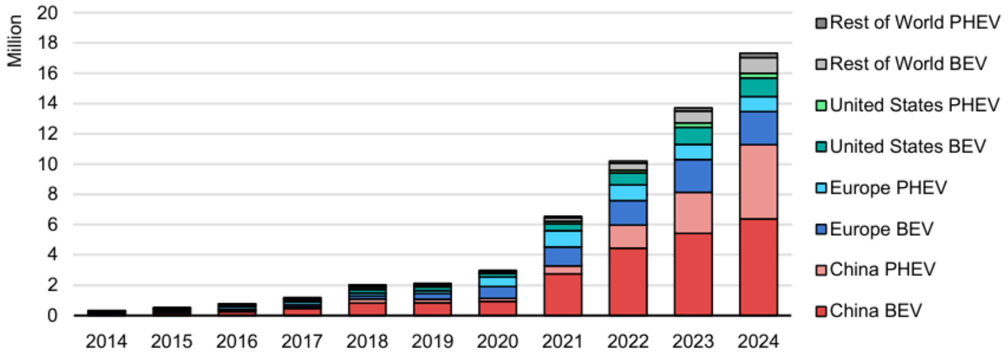

Figure 1.13 - Global electric car sales (2014-2024) [29].

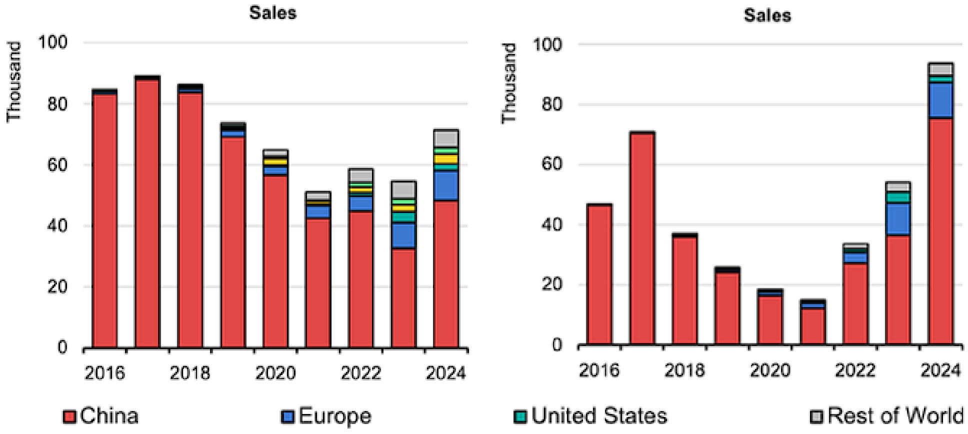

Figure 1.14 - Global electric bus (left) and truck (right) sales (2014-2024) [29].

As the adoption of electric vehicles (both BEVs and FCEVs) continues to grow, the number of refuelling stations is also increasing. Figure 1.15 shows the rise in Hydrogen Refuelling Stations (HRS) from 2020 to 2024, nearly doubling to just over 1 200 units. Most stations are located in Asia, followed by Europe and United States, consistent with vehicle distribution patterns.

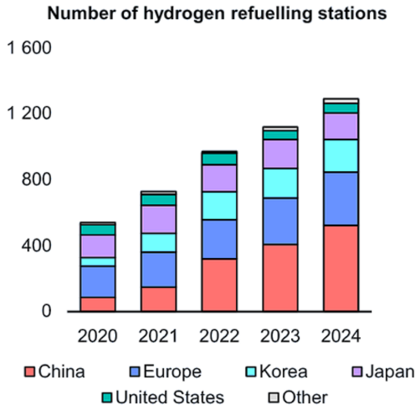

Figure 1.15 - Global number of hydrogen refuelling station [28].

Figure 1.16 presents the projected growth of electric charging stations for light-duty (left) and heavy-duty (right) vehicles through 2030. In 2024, there were just over 50 million chargers for light-duty vehicles, most of which were private. By 2030, this number is expected to exceed 200 million, with continued dominance of private investments. For heavy-duty vehicles, the number of chargers surpassed one million in 2024 and is projected to reach over 5 million by 2030, with a focus on investments on truck infrastructure.

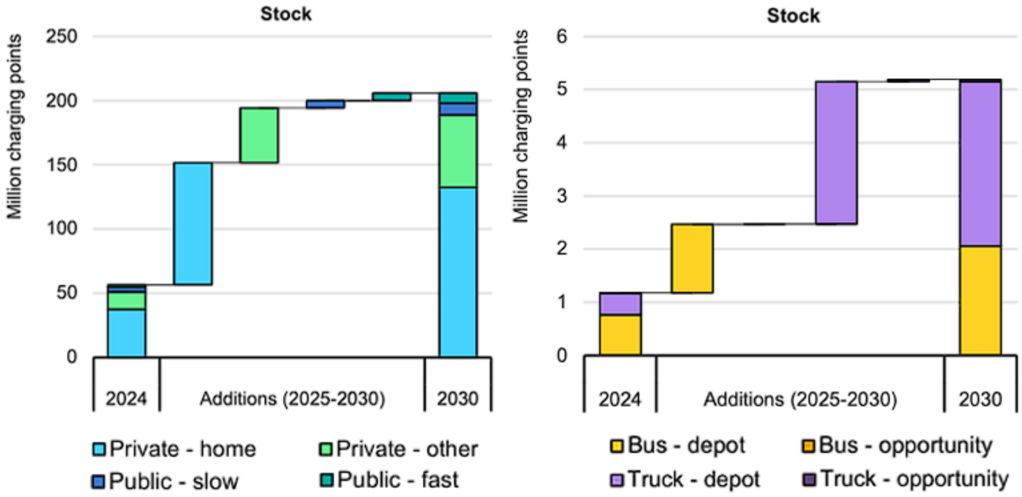

Figure 1.16 - Global number of light duty (left) e heavy duty (right) electric vehicles charger [29].

The choice between BEVs and FCEVs become particularly relevant when considering the vehicle class. For light-duty vehicles, battery weight is generally manageable, and BEVs benefit from higher energy efficiency compared to FCEVs. However, in heavy-duty applications, the mass of battery systems can become a limiting factor [30–33]. Hydrogen, with its superior gravimetric energy density, allows FCEVs to maintain a lower overall system weight, making them more suitable for long-range and high-payload operations [30,32,33].

One of the key operational advantages of FCEVs is their refuelling time. Light-duty FCEVs can be refueled in approximately 3–5 minutes, similar to conventional petrol or diesel vehicles [30,32,33], while heavy-duty models may require around 10 minutes [32]. In contrast, BEV charging times vary widely depending on charger type and vehicle specifications: fast DC charging for light-duty BEVs typically takes between 30 minutes and over an hour [30]. For heavy-duty trucks, earlier studies report charging times exceeding 1 hour even with high-power chargers [32]. Although recent technological advancements may have shortened these durations, FCEVs remain advantageous in contexts where minimizing downtime is essential.

Despite these benefits, FCEVs have not yet seen widespread adoption. Current research is focused on improving the efficiency and affordability of hydrogen fuel cells, as well as expanding the infrastructure for hydrogen production, storage, and distribution. Increasing the number of refuelling stations and reducing the costs associated with hydrogen logistics are considered essential steps toward broader deployment of FCEVs [34].

Focusing on heavy-duty vehicles and considering the advantages of FCEVs over battery-powered alternatives, the following sections will explore hydrogen storage and refueling technologies. As known, FCEVs require dedicated infrastructure, whose deployment should progress in parallel with the adoption of such vehicles. A summary of the differences between the two different electric vehicles is given in Table 1.2.

Table 1.2 - Summary of the differences between BEV and FCEV.

Characteristic	BEV	FCEV
Energy efficiency	Higher compared to FCEVs	Lower compared to BEVs
Gravimetric energy density	Lower (heavy batteries)	Superior (hydrogen)
System weight	Battery mass can be a limiting factor in heavy-duty applications	Lower overall system weight
Ideal applications	Light-duty vehicles (battery weight generally manageable)	Heavy-duty applications (long-range and high-payload operations)
Refueling/charging time (light-duty)	30 minutes to over 1 hour (fast DC charging)	Approximately 3-5 minutes (similar to conventional petrol/diesel vehicles)
Refueling/charging time (heavy-duty)	Over 1 hour (even with high-power chargers)	Around 10 minutes
Downtime	Longer due to charging times	Minimal downtime (advantage where minimizing downtime is essential)
Current adoption	Widespread	Not yet widespread
Infrastructure	More developed	Requires expansion (production, storage, distribution, refueling stations)
Technology maturity	More mature	Focused on improving efficiency and affordability

1.4 Hydrogen storage systems and refuelling stations

In the context of heavy-duty FCEVs, hydrogen storage and refuelling infrastructure play a pivotal role in ensuring both performance and safety.

Among the various hydrogen storage methods, the most widely adopted in practical applications are high-pressure gas compression and cryogenic liquefaction [34–37]. Alternative approaches, such as metal hydride storage and carbon-based adsorption (e.g., carbon nanotubes), are still in the research or prototype phase due to limitations in weight, kinetics, and scalability [34–37]. Several studies have been conducted on hydrogen storage with metal hydrides [38,39], liquefied hydrogen

[40–43] and high-pressure hydrogen gas [44,45] in heavy-duty FCEVs, with the latter method being the most widespread.

For the storage of gaseous hydrogen, five main tank types are used, each with distinct structural and performance characteristics. Type I (entirely metallic) and Type II (metal liner with partial composite wrap) are limited to pressures up to 300 bar [46]. Type III (aluminium liner with full composite wrap) and Type IV (plastic liner with full composite wrap) can reach pressures up to 700 bar and are preferred in mobility applications, due to their lower weight and higher gravimetric storage capacity [47–50]. Type V tanks, made entirely of composite material, are still under development and mainly considered for aerospace applications, with limited maturity for use in FCEVs at 700 bar [47,51,52].

A key aspect of storage tank modelling is heating transfer during refueling. In this way, semi-empirical and empirical correlations are often used, based on dimensionless numbers such as Nusselt, Reynolds, and Rayleigh [53,54]. These allow dynamic calculation of the heat transfer coefficient, which depends on parameters like mass flow rate, injection geometry, gas temperature, and pressure. Assuming a constant coefficient can lead to inaccurate predictions, especially during fast fills [55]. The refuelling of high-pressure hydrogen tanks presents significant thermodynamic challenges. Rapid gas compression and the negative Joule-Thomson effect led to a sharp temperature increase during fast fills [56–58]. This thermal rise must be carefully controlled to prevent tank deformation, material fatigue or failure. To address these risks, the SAE J2601-5 protocol, specific to heavy-duty vehicles, establishes strict safety thresholds: a maximum temperature of 85 °C and a peak pressure of 1.25 times the nominal working pressure [49,59,60]. To ensure compliance with these limits, thermodynamic modelling of HRS systems is essential.

There are several types of HRS configurations: they vary depending on how the hydrogen is stored (in liquid or gaseous phase) and where it is produced (on-site or off-site). In the case of on-site production, hydrogen is produced, stored, and used locally, whereas in the off-site configuration, hydrogen is produced at a different location and subsequently transported (via pipeline or by road tankers) to the HRS, where it is then stored and used on-site. When on-site production is insufficient, a hybrid solution can be adopted to meet the demand.

Regarding storage methods, liquid hydrogen requires lower storage temperatures (-253°C) and therefore high energy consumption [61]. It is adopted when high storage density is required, for example in aeronautical or aerospace applications. Gaseous hydrogen is more common in the mobility sector, and through compression, it is possible to considerably reduce the volume of storage tanks.

Figures 1.17 and 1.18 show two different layout examples for hydrogen stored in gaseous form, characterized by cascade storage and a booster dispensing compressor, respectively. Both figures refer to a maximum refueling pressure of 70 MPa, but the considerations are analogous for 35 MPa refueling. Moreover, both consider different production methods: on-site (1) and off-site (2,3).

In the case of a cascade system (Figure 1.17), a compressor compresses low-pressure hydrogen up to the maximum pressure (4). Hydrogen is then stored in tanks (5) and, if necessary, supplemented with externally produced hydrogen (6). Due to the high temperatures resulting from compression, a precooling system (7) is required before vehicle refueling. In this case, refueling occurs through the pressure difference between storage and vehicle. In addition to the case shown in the figure, where 1 or all tanks have the same pressure, configurations with high-pressure cascade storage tanks at different pressures can be found, in order to reduce the tank volume [62].

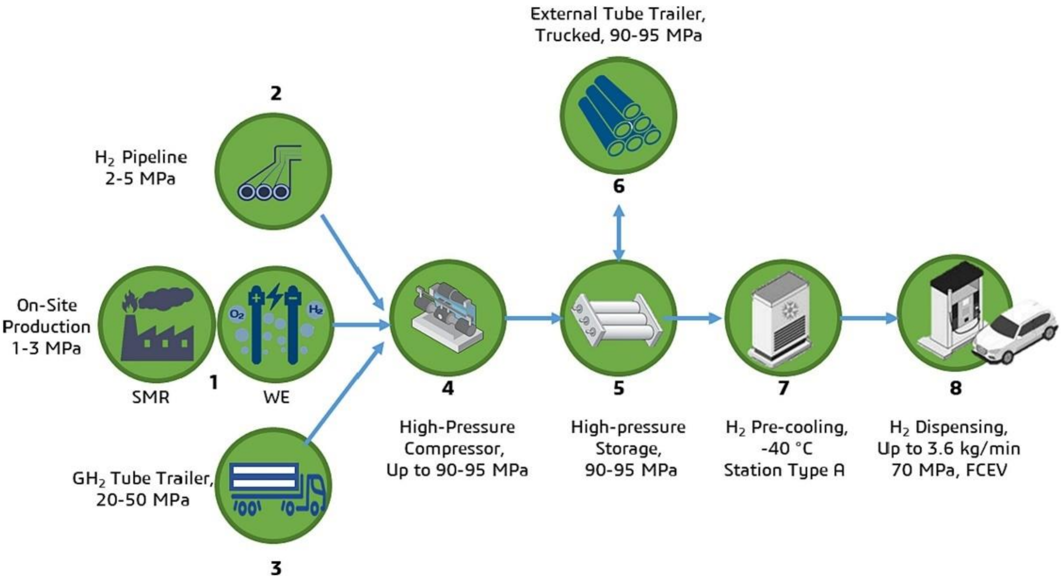

Figure 1.17 - Example of a gaseous hydrogen storage HRS layout with cascade refueling.

The layout characterized by a boosting dispensing compressor instead features a first compressor with intermediate pressure relative to the system maximum (4), medium-pressure storage tanks (5), and a second booster compressor (6) that compresses to the maximum pressure. There is also a high-pressure storage buffer (7) to meet potential demand deficits. As before, a precooling system (8) is present before refueling (9).

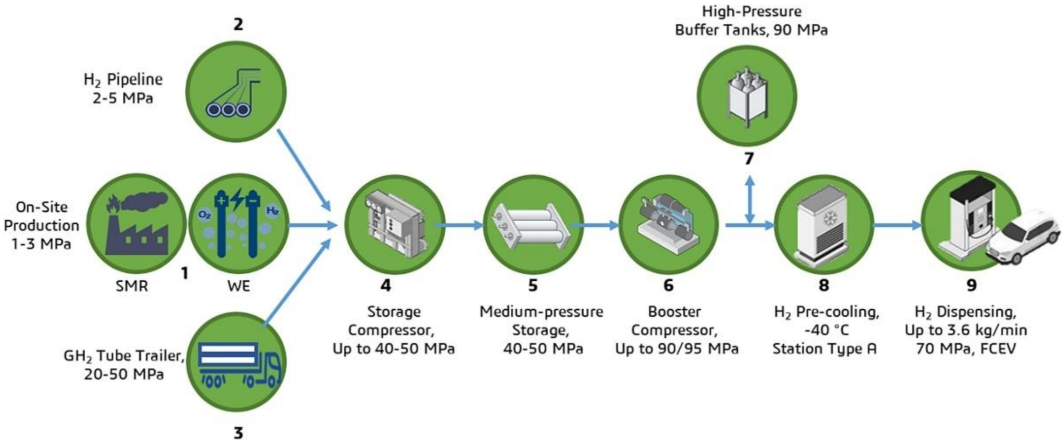

Figure 1.18 - Example of a gaseous hydrogen storage HRS layout with a booster dispensing compressor.

In the case of liquid storage, different components present in the layout are cryogenic storage tanks at -253°C and evaporators, which enable gaseous hydrogen to be obtained in a heat exchanger through the evaporation of liquid hydrogen caused by ambient heat, subsequently stored in the upper region of the cryogenic tank. The hydrogen is then compressed and stored. An alternative may be the use of a cryogenic pump placed between the cryogenic storage and the evaporator to pressurize the liquid hydrogen in the cryogenic tank located upstream of the system, which is then gasified through an evaporator and stored. All components from high-pressure gaseous storage onwards are also present in the case of liquid storage. [56–58]Numerous studies have investigated HRSs, most of them aiming to balance refuelling speed with thermal safety. De Miguel et al. [63]. Molkov et al. propose a thermodynamic model for two type III and one type IV tanks, but the study placed limited emphasis on SAE compliance. Final SOC values were below 100%, as pressure targets were reached before full fill [64]. Deng et al. focus on the correlation between initial and final temperatures during refuelling of four tanks (two type III, two type IV), using fixed refuelling times from literature (3.33–3.67 minutes), thus without calculating them directly [65]. Liu et al. study both refuelling and post-refuelling maintenance phases, highlighting the need for preliminary cooling due to final temperatures exceeding 100 °C. Refuelling times were set constant at 3 and 5 minutes, depending on the simulation [66]. Fragiacomo et al. model the refuelling of a 230 l type IV tank at 35 MPa in Matlab-Simulink, focusing on pressure losses and control valves. Refuelling times varied between 3.5 and 10 minutes, while respecting SAE J2601-2 limits [67]. Luo et al. introduce a three-stage cascade refuelling strategy, reducing refuelling time from 40 to 20 minutes. Their Matlab-Simulink model considered both single and multiple tanks at 35 MPa [68]. Xiao et al. implemented a detailed heat transfer model for type III and IV tanks, distinguishing between hydrogen, tank wall, liner, and shell. Refuelling times were around 3.5 minutes across various tank volumes (29–171 l) [69]. Tun et al. model the full HRS infrastructure for a 1400 l type IV tank at 70 MPa, using two configurations (28×50 l or 4×350 l). Refuelling times ranged from 4.7 to 9 minutes, depending on SOC and temperature limits [70]. Martorelli et al. also study a 25 l type III tank at 70 MPa, considering infrastructure components. Refuelling times varied between 2 and 3.72 minutes [71]. Stops et al. uniquely investigate the full hydrogen lifecycle including discharge, refuelling, and dormancy for gaseous, cryo-compressed, and liquid hydrogen. However, no specific refuelling times were reported [72]. Saferna et al. investigate the thermodynamic behaviour during rapid filling of type IV composite tanks with hydrogen, methane, and their blends. Results show hydrogen fills tanks 36% faster than methane but stores 28% less energy due to lower density. Hydrogen also generates 52% more entropy and reaches higher temperatures during filling [73]. Caponi et al. compare single-tank and multi-tank cascade hydrogen storage systems for refueling fuel cell buses using a dynamic thermodynamic model. Both systems deliver similar refueling time: about 38 minutes to dispense 37.58 kg of hydrogen per bus [74]. Galassi et al. investigate fast hydrogen filling using validated CFD simulations to assess temperature evolution and safety. Various scenarios are analysed: adiabatic, cold filling, and different pressure-rise profiles. Results show that adiabatic filling leads to a 20% higher temperature and 10% less hydrogen mass, while cold filling reduces peak temperature by 5% and increases hydrogen mass by 3.6% [75]. Li et al. present a thermodynamic study of fast filling in a 50 MPa hydrogen storage tank, focusing on temperature and pressure evolution. Shorter filling times result in higher temperature rise. In this regard, strategies combining pre-cooling and variable filling rates are proposed to reduce temperature and improve safety [76]. Hall and Ramasamy develop a thermodynamic model to simulate gas temperature during fast filling of hydrogen cylinder. Refueling times range from 37 to 200 seconds, depending on the case [77].

The most relevant results from these studies are summarized in Table 1.3, which highlights the key parameters and result.

Table 1.3 - Studies on the thermodynamic refuelling of hydrogen tanks.

Reference	Refuelling time [min]	Tank type	Tank capacity [l]	Tank Pressure [MPa]
[63]	2.6 – 9.7	III	40	70
	4.2 – 4.3	IV	29	70
	4.8 – 8.1	IV	19	70
[64]	10.67	III	74	70
	7	III	40	70
	4.17	IV	29	77
[65]	3.33 – 3.67	IV	174	-
		III	40	77
		IV	29	77
		III	25	-
[66]	3	III	150	35
	5	IV		70
[67]	3.5 – 10	IV	230	35
[68]	17.8 – 43.3	-	90.5	35
[69]	3.5	IV	29	70
		III	171	35
		IV	72	35
		III-IV	150	35
[70]	4.9 – 9	IV	1 400	70
[71]	2 – 3.72	III	25	70
[72]	-	III	500	40
	-	-		1.6
	-	III		70
[73]	1.58 – 4.67	IV	1.2 – 350	35 – 70
[74]	38	III	4 030 – 6 700	30 – 45
[75]	4	IV	29	70
[76]	0.2 – 3.33	-	342	50
[77]	0.62 – 3.33	III – IV	28.9 – 74.3	77.5

While many studies contribute valuable insights into the thermodynamics of hydrogen refuelling, not all explicitly verify compliance with SAE J2601-5 limits. Some focus primarily on modelling the tanks or infrastructure, while others omit key parameters such as final SOC or refuelling time. This variability highlights the need for standardized approaches that integrate safety thresholds, refuelling duration, and system-wide thermal behaviour to support the modelling and development of reliable and efficient HRS systems for heavy-duty applications. Furthermore, to compete with traditional ICE vehicles, it would be appropriate to study solutions with a high hydrogen storage capacity, so as to bring the autonomy of hydrogen vehicles closer to that of diesel or petrol ones.

As previously mentioned, the use of FCEVs is advantageous if the hydrogen used is produced without GHG emissions, i.e., from renewable sources. The next section therefore provides an overview of the integration of HRS into renewable microgrids.

1.5 HRS integration into renewable microgrids

In the current context, characterized by the urgent need to replace conventional transport with more sustainable alternatives, it is reasonable to expect that future vehicles will increasingly rely on renewable energy carriers. To ensure a real reduction in GHG, hydrogen used in FCEVs must be produced sustainably. The most effective pathway is green hydrogen production through electrolysis powered by renewable sources, which avoids CO_2 emissions associated with fossil-based hydrogen [78]. Indeed, studies show that the use of green hydrogen in FCEVs results in significantly lower environmental impacts compared to diesel buses and even to hydrogen derived from natural gas or grid electricity [79].

Building on this perspective, several techno-economic and optimization studies explored different solutions for green hydrogen infrastructure including HRS. Genovese et al. investigate a hydrogen infrastructure including Hydrogen Generator (HG), Hydrogen Compressor (HC), storage, precooling and dispenser, designed to supply green hydrogen to heavy-duty vehicle fleets. Two power supply options are compared: green electricity and direct on-site solar PV. Results show that solar-powered infrastructures are more cost-effective, with a Levelized Cost of Hydrogen (LCOH) ranging from 5.5 to 27.5 €/kgH_2, versus 7.4 to 67.8 €/kgH_2 produced by green electricity [80]. Okonkwo et al. evaluate a hybrid renewable energy system with Photovoltaic (PV), Wind Turbine (WT), HG, Battery Storage (BS) and Hydrogen Tanks (HTs) for powering an HRS in Al-Kharj, Saudi Arabia. Using HOMER software, they identify an optimal configuration (characterized by lowest component sizes) with a LCOH of 9.34 $/kg and Levelized Cost of Energy (LCOE) of 0.6208 $/kWh, making it the most cost-effective solution for local green hydrogen production [81]. Parsibenehkohal et al. propose a two-stage optimization framework for coordinating networked microgrids with HRS and BEV charging stations. The model integrates renewable sources (PV, wind), thermal generators, BS, BEVs, FCEVs, HRS, HG and aims to minimize both operational costs and emissions. Results indicate a 4.77% reduction in operating costs and a 49.13% decrease in emissions when using multi-objective optimization [82]. Ancona et al. develop an optimization methodology for hybrid PV/hydrogen microgrids including PV panels, BS, HG, hydrogen storage and a fuel cell. The model, implemented in Matlab, maximizes renewable self-consumption and storage efficiency through optimal sizing and management. The best configuration includes a 3.7 kW HG, 4 kW fuel cell, and 36 kWh BS. The system achieves ~30% storage efficiency in summer and ~40% in winter, producing 87.5 kg of hydrogen annually

[83]. Safak et al. propose a multi-objective optimization model for a grid-interactive HRS integrating RESs, BS, HG, a fuel cell, and HT. RES integration improves sustainability and allows surplus hydrogen production, reducing external dependency and boosting profitability. The optimal setup yields the highest financial gain (587.83 $), though load factor maximization is only achievable without RESs due to trade-offs with grid stability [84]. Sun et al. present a load management strategy for HRS (HG, HC and storage) to support grid integration of renewable energy produced with WT. By adjusting electricity consumption in real time, the HRS reduces transformer overloading and avoids up to 92% of wind curtailment compared to passive operation. Over one year, this strategy enables 5.8 GWh of wind energy to be utilized and cuts electricity costs by 7.5%, with an additional 5% savings possible through grid service rewards [85]. Al-Sharafi investigate the techno-socio-economic feasibility of HRS powered by hybrid PV/WT systems in Saudi Arabia. The system includes PV panels, WT, HG, HC, HT, fuel cell, and cooling/dispensing units. Using real refuelling data from four area types, they optimize system sizing for off-grid and on-grid scenarios. Results show that synchronization between solar availability and hydrogen demand (STSF) significantly affects cost: the industrial area (STSF = 0.62) achieves the lowest hydrogen cost (7.81–9.62 $/kg), while the tourist area (STSF = 0.38) has the highest (7.81–9.90 $/kg) [86]. Rizk-Allah et al. present a techno-economic analysis of a standalone wind–PV power plant designed to produce green hydrogen for a refuelling station and power. The system includes PV panels, WT, HG, BS, and HTs. Using HOMER software, the optimal configuration generates 6 997 990 kWh/year and 85 595 kg/year of hydrogen, with a LCOH of 2.89 €/kg and a Net Present Cost (NPC) of 5.49 M€ [87]. Di Micco et al. present a techno-economic analysis of an on-site solar-powered HRS. The system includes a PV plant, HG, BS and HCs. The station can produce up to 450 kg/day of green hydrogen, with an annual output of 123.1 tons. The LCOH is estimated at 10.71 €/kg, with the production section contributing 89% of the total cost [88]. Barhoumi et al. analyse three PV based configurations for green HRS in Salalah, Oman. Using HOMER software, the authors compare grid-connected PV, stand-alone PV with BS, and stand-alone PV with fuel cells. Each system includes PV panels, HG, HTS and inverters. The grid-connected PV system produces 58.62 t H_2 annually at a LCOH of 5.5 €/kg, with the lowest Net Present Cost (NPC). The BS and fuel cell systems yield higher costs (5.74 €/kg and 7.38 €/kg, respectively) but offer zero emissions. The grid-connected option is identified as the most cost-effective [89]. Bahou presents a techno-economic analysis of an on-site HRS powered by grid-connected PV panels to supply fuel cell taxis. Key components include HG, low- and high-pressure tanks, and a solar system. The station is designed to produce up to 152 kg/day of hydrogen. Results show a hydrogen costs range from 9.18 to 12.56 $/kg, depending on station size [90]. Hussain at al. present an optimization model for sizing a stand-alone HRS powered by on-site WT and PV. Key components include WT, PV, HG and hydrogen storage tanks. The station is designed to meet a daily hydrogen demand of 2 tons/day, scalable to 10 tons/day. Two configurations are analysed: near-green (minimal hydrogen import) and mixed-green (up to 18% imported hydrogen). The results concern a LCOH between 2.94 to 8.99 $/kg [91]. Kavadias et al. investigate the sizing and economic viability of an HRS powered by surplus energy from a wind farm in remote Greek regions. Key components include

HG, storage tanks and buffer tanks. Economic analysis shows that scenarios with higher FCEV penetration (≥100 vehicles) are financially viable, with payback periods around 7.4–10 years and specific costs of 11.5–12.8 €/kg [92]. Gu et al. compare four solar-integrated hydrogen supply routes for refueling stations. The station includes HG, storage tanks and HCs. Route IV (on-site solar electrolysis) achieves near-zero CO_2 emissions, while Route III (liquid H_2 delivery) reduces emissions by 96%. Routes III and IV also show superior energy efficiency, consuming 27% and 38% less energy than coal-based H_2 [93]. Tang et al. evaluate the economic feasibility of HRS powered by solar PV and WT in Sweden, comparing on-grid and off-grid configurations. The HRS include HG, solar PV units, WT, and hydrogen storage tanks. Simulations across nine cities show that wind speed significantly affects hydrogen cost, while solar radiation has less impact. The LCOH ranges from 71÷153 SEK/kg (off-grid) and 35÷72 SEK/kg (on-grid). Combining solar and wind improves performance, and grid integration notably reduces LCOH, especially in low-wind regions [94].
The main results of the previous studies are summarized in Table 1.4.

Table 1.4 - Studies on hydrogen refuelling stations integrated with renewable microgrids.

Reference	**PV [kW]**	**WT [kW]**	**BS [kWh]**	**HG [kW]**	**HS [kg]**	**HS Pressure [MPa]**
[80]	1 000	-	-	1 000	400	3 – 70
[81]	270 – 520	300 – 600	70 – 100	500 – 800	100	-
[82]	100 – 750	400 – 2 300	-	-	-	-
[83]	11.4	-	36	3.7	87.5	-
[84]	500	1 000	1 000	500	1 000	-
[85]	-	1 000	-	2 900	440	-
[86]	88 – 419	600	-	240	50 – 830	35 – 70
[87]	298	2 200	600	1 000	800	-
[88]	8 000	-	3 500	2 100	450	200 – 900
[89]	3 000 – 4 000	-	-	1 000	300	-
[90]	1 944	-	-	453.5	0.9 – 47.7	0.5 – 87.5
[91]	22 000	18 000	-	11 000 – 14 000	11 700	70
[92]	-	10 000	-	8 000	2295 .1	70
[93]	-	-	-	-	500	45
[94]	250	250	-	270	1 900	-

As can be observed, some authors focused mainly on techno-economic analyses of hydrogen refuelling stations powered by renewable energy systems comparing different energy supply options and configurations to minimize costs. Others concentrated on optimization frameworks integrating hydrogen infrastructures into broader energy systems and microgrids, aiming to reduce operational costs and emissions while enhancing renewable utilization. A further studies addressed specific operational strategies, such as load and demand management or grid interaction, with the objective of improving flexibility, system stability, and overall profitability. Nevertheless, not all contributions explicitly specify the hydrogen dispensing pressure (distinguishing between 35 MPa and 70 MPa) or the daily or annual hydrogen production. In addition, most works proposing optimization or management strategies of microgrids and hybrid systems use hydrogen production and cost assessment as the main evaluation criteria, without explicitly integrating the operational management of the refuelling station itself. This results in limited applicability of HRS implementation and integration in renewable systems, where factors such as safety standards, refuelling protocols, and end-user requirements are equally crucial.

1.6 SAE J2601-5 protocol overview

The safe and efficient refueling of hydrogen vehicles requires adherence to established protocols that balance refueling speed with thermal and pressure safety constraints. The Society of Automotive Engineers (SAE) has developed the J2601 series of standards to address these requirements across different vehicle categories and pressure levels. While SAE J2601-2 focuses on light-duty vehicles operating at 70 MPa, SAE J2601-5 specifically addresses heavy-duty applications, covering both 35 MPa systems (typically for buses) and 70 MPa systems (for heavy-duty trucks with higher storage requirements). Since this study focused on the refueling of Heavy-Duty Vehicles both at 35 MPa and 70 MPa, an overview of the most important characteristics of the SAE J2601-5 protocol is given in Table 1.5.

The refueling of high-pressure hydrogen tanks is a critical aspect that demands special attention to prevent tank failure, material degradation, or dangerous overheating. This is primarily due to the rapid compression of hydrogen gas and the negative Joule-Thomson effect, both of which cause significant temperature increases during fast refueling. To mitigate these risks, SAE J2601-5 establishes two fundamental safety thresholds that must be respected throughout the entire refueling process, as reported in the table: a maximum hydrogen temperature of 85°C and a maximum pressure equal to 1.25 times the Nominal Working Pressure (NWP). These limits apply to both 35 MPa and 70 MPa protocols and are designed to ensure the structural integrity of the storage tanks and the safety of both the refueling infrastructure and end users.

As reporter in the table, SAE J2601-5 defines multiple refueling protocols tailored to different pressure classes and operational requirements. For 35 MPa applications, the MCF-HF-G protocol is designed for buses and medium-duty vehicles, with a gas pressure limit of 43.75 MPa and a maximum mass flow rate of 120 g/s. This protocol is particularly relevant for urban bus fleets, where refueling times of approximately 3-4 minutes are targeted.

For 70 MPa applications, two protocols are available: Category D HF and MCF-HF-G. These protocols support heavier storage capacities (10 ÷ 201 kg of hydrogen) and are designed for heavy-duty vehicles requiring extended driving ranges. The gas pressure limit is set at 87.5 MPa and maximum flow rates can reach up to 300 g/s in the most advanced configuration (H70HF).

Table 1.5 - Refueling protocols at 35 MPa and 70 MPa [60].

Protocol Name		MCF-HF-G[*]		Category D HF[**]
Pressure Class		H35	H70	H70
Gas p Limit	**[MPa]**	43.75[***]	87.5[***]	
Gas T Limit	**[°C]**	85	85	
CHSS Capacity	**[m^3]**	0.2486 ÷ 7.5	0.2486 ÷ 5	
CHSS Capacity	**[kg]**	5.97 ÷ 180	10÷201	
CHSS Tank Sizes	**[m^3]**	0.05 ÷ 1	0.05÷0.8	
Max. Flow Rate	**[g/s]**	120	60, 90 or 300	60 or 90
Fuel Delivery Temperature Categories	**[°C]**	T40 (-40 ÷ -33)		T40D (-40 ÷ -33)
		T30 (-33 ÷ -26)		T30D (-40 ÷ -26)
		T20 (-26 ÷ -17.5)		T20D (-40÷ -17.5)
		T10 (-17.5 ÷ -10)		-
		T0 (-10 ÷ 0)		-
		TA (0 ÷ 20)	-	-
Coupling Type (Dispenser - Vehicle)[****]	**[g/s]**	H35HF (120)	H70 (60 or 90) H70HF (300)[*****]	-

[*] Mass Change Formula-based refueling protocol which utilizes a dynamic pressure ramp rate continuously calculated throughout the fill (Mass Change Formula - High Flow - General).

[**] High-flow version of the CHSS capacity category D protocol described in SAE J2601.

[***] NWP·1.25. 1.25 is a necessary factor to compensate for the effect of compression and heating of the gas during rapid filling.

[****] Coupling types are defined in SAE J2600 and ISO 17268

[*****] The H70HF (High-Flow) coupling is not yet defined in a standard

The refueling protocols assume that the process begins once the dispenser completes the nozzle connection and performs initial system checks. The entire station infrastructure is responsible for ensuring that the process remains within the defined operational limits throughout the refueling. Several variables critically influence the refueling dynamics, including ambient temperature, fuel delivery temperature, the configuration and properties of the Compressed Hydrogen Storage System (CHSS), such as dimensions, shape, material properties, initial temperature and pressure, and flow dynamics and thermodynamic properties between the dispenser and the vehicle [60].

It is important to note that, as indicated in Table 1.5, the coupling type for the maximum mass flow rate of 300 g/s (H70HF) is not yet fully defined in the current standards. Furthermore, it must be acknowledged that the availability of components, such as nozzles, valves, sensors, and mass flow meters, capable of reliably operating at 300 g/s is currently limited, with most still in the prototype or early development stage. While such flow rates are envisioned for future heavy-duty hydrogen refueling applications, the market maturity of supporting hardware remains relatively low, and the full standardization of H70HF is still ongoing.

1.7 Purpose and impact of the research

The literature review highlights several gaps in the current state of research both on hydrogen refueling infrastructure and its integration with renewable energy systems.

Regarding hydrogen storage systems and refueling stations, while numerous studies have investigated the thermodynamic behaviour during refueling, key limitations persist. Many works do not explicitly verify compliance with SAE J2601-5 safety limits, or they focus primarily on tank modelling without addressing the complete refueling infrastructure. Furthermore, several studies omit critical parameters such as final State of Charge (SOC) or do not calculate refueling times directly, instead relying on fixed values from literature. Most importantly, there is a lack of comprehensive, flexible modelling tools that can be adapted to different vehicle types, tank configurations (Type III to V), and operational scenarios while systematically evaluating the influence of design parameters on refueling performance and safety compliance. Additionally, limited attention has been given to heavy-duty applications with high hydrogen storage capacity (up to 100 kg), which is essential for achieving driving ranges comparable to conventional diesel vehicles.

Concerning HRS integration into renewable microgrids, existing studies predominantly focus on techno-economic optimization and component sizing, often treating hydrogen production as an isolated parameter without explicitly integrating the operational management of the refueling station itself. Many works do not clearly specify key operational details such as hydrogen dispensing pressure (35 MPa vs. 70 MPa) or provide comprehensive annual/daily production data. Moreover, while several studies address energy management strategies and grid interaction, few explicitly evaluate the economic impact of selling surplus renewable energy back to the grid or comprehensively assess the environmental implications through CO_2 emissions analysis. This results in a gap between microgrid optimization frameworks and the practical implementation requirements of HRS, where safety standards, refueling protocols, thermal management, and end-user service quality are equally critical.

In response to these gaps, this study aims to provide an integrated approach that bridges hydrogen refueling infrastructure modelling with renewable microgrid optimization, addressing both technical performance and techno-economic feasibility. The specific objectives of this study are:

- The development of comprehensive dynamic models of Hydrogen Refueling Stations (35 MPa and 70 MPa) to assess and optimize refueling capacity under different operational scenarios, ensuring compliance with SAE J2601-5 safety protocol. This includes both stationary HRS modelling and onboard vehicle storage systems for heavy-duty applications, with validated thermodynamic models capable of simulating realistic operational conditions (e.g., seasonal variations, fleet-based demand) and the maximization of the refueling number after a parametric analysis;
- The integration of HRS into renewable microgrids and optimization of system design through multi-objective function to minimize levelized cost of hydrogen (LCOH) while maximizing self-sufficiency ratio (SSR). This objective addresses the gap in existing literature by explicitly linking HRS

operational requirements with renewable energy system design, proposing and comparing different energy management strategies (renewable-based, mixed, and grid-only operation) while accounting for realistic hydrogen and electricity demand profiles;

- The evaluation of the techno-economic feasibility and environmental sustainability of renewable hydrogen infrastructure by comparing different energy management strategies, assessing the economic impact of grid interaction and surplus energy sales, and quantifying the environmental impact through CO_2 emissions analysis for grid-based hydrogen production. This provides a more complete evaluation framework that integrates economic viability with environmental performance, addressing the limited consideration of grid revenue and emissions assessment in current studies.

The main contributions of this research include: (i) the development of flexible, validated dynamic models for both HRS and onboard HSS that can be adapted to different applications and operational scenarios; (ii) a comprehensive framework for integrating HRS into renewable microgrids with explicit consideration of refueling protocols, safety requirements, and thermal management; (iii) a multi-objective optimization approach that balances cost minimization with energy self-sufficiency while accounting for grid interaction economics; and (iv) a holistic techno-economic and environmental assessment that supports decision-making for sustainable hydrogen infrastructure deployment. These contributions provide practical engineering tools and insights to support the design, optimization, and implementation of safe, efficient, and economically viable hydrogen refueling systems powered by renewable energy.

2. Hydrogen Refuelling Station: Dynamic Modelling, Management and Different Operating Scenarios

This chapter describes the mathematical modelling and thermodynamic analysis of the HRS at 35 MPa. The station is designed to refuel hydrogen buses operating at 35 MPa, and the analysis focuses on assessing refueling capacity under both parametric analysis and realistic simulation while ensuring compliance with SAE J2601-5 safety protocol, particularly with MCF-HF-G with pressure class H35.

The initial system configuration is shown in Figure 2.1. As shown in the figure, the HRS layout consists of several key components: a Low-Pressure Tank (LPT) for initial hydrogen storage, a Hydrogen Compressor (HC) to pressurize the hydrogen, a 3-stage cascade system of High-Pressure Tanks (HPT) for intermediate storage, a hydrogen Pre-Cooling (PC) system to manage thermal effects during refueling, Vehicle Tanks (VT, 6 per bus) and various control valves. The figure also indicates the Nominal Working Pressures (NWP) of each components.

The LPT operates at 3.5 MPa, corresponding to the delivery pressure from the HG. The cascade system comprises 3 HPTs with progressively increasing pressures: 35 MPa (HPT3), 40 MPa (HPT2), and 45 MPa (HPT1). This configuration was specifically designed to enable efficient refueling of buses equipped with 35 MPa vehicle tanks. The cascade strategy allows for sequential tank utilization, optimizing hydrogen transfer and minimizing compression energy. To support this architecture, the HC is capable of compressing hydrogen to pressures up to 45 MPa, depending on which HPT is being refilled. All storage tanks (both the LPT and the HPT cascade system) are assumed to be located outdoors, exposed to ambient temperature variations throughout the year.

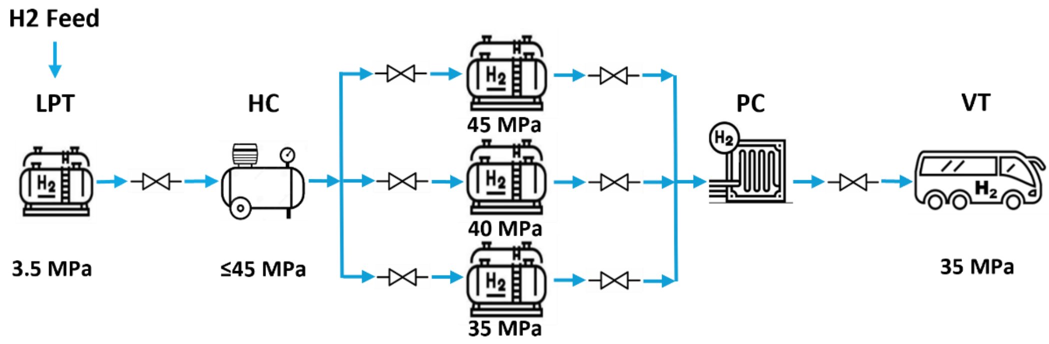

Figure 2.1 - Schematic system of the Hydrogen Refuelling Station considered.

The purpose of the HRS is to supply high-pressure hydrogen (35 MPa) to a certain number of hydrogen buses when requested by the buses themselves. In order to understand how many buses can be refuelled without exceeding the limits set by the SAE J2601-5 protocol (focused on refuelling heavy-duty vehicles) [60] and considering that the HRS will be refuelled with green hydrogen produced from renewable sources, a one-hour HRS working period was studied in Matlab-Simulink. This makes it possible to carry out a dynamic study of the thermodynamic behaviour inside all hydrogen tanks, particularly those on buses, to verify that the pressure and temperature values are always lower than those imposed by the protocol. Furthermore, it is possible to know how many buses can be refuelled in one hour (always in compliance with SAE limits), leaving time at the end of the VT refuelling process to refuel the storage system.

Finally, two simplifications were made during the simulation: the refuelling of the VTs is considered simultaneous, as if each tank were positioned at the same distance from the refuelling nozzle; pressure losses due to infrastructure elements such as valves, pipes, elbows, etc. have been neglected for simplicity. Furthermore, of these latter components, only the delivery valves have been modelled.

The modelling of the main components (storage tanks, hydrogen compressor, pre-cooling and valves) of the HRS will be explained in detail below. Particularly, the VT model was validated by means of the test rig at HyCentA GmbH [95], with data collected previously: this model was then used for all tanks considered in this study, changing some geometrical characteristics. The results of the thermodynamic model, as well as those of the different operational scenarios, will be discussed at the end of the chapter.

2.1 Mathematical modelling and validation of the Vehicle Tank

The VTs were modelled and validated in Matlab-Simulink using the data present in [96], considering a type III tank, directly in the research centre where the study was made. A simplified layout of the piping and instrumentation of the refuelling test rig, set up at the HyCentA laboratory, is reported in Figure 2.2 [96]. In particular, the tank was placed inside a climatized testing chamber and supplied with hydrogen from a high-pressure reservoir (87.5 MPa). The pressure ramp rate of the refuelling process was controlled via a regulator valve. The hydrogen was pre-conditioned either by a heat exchanger (pre-heating in tests 1–3) or by a gas chiller (cold fill in tests 4–12). The tank was connected to the infrastructure at the filling receptacle with coupling. More information about the distances of each component are reported in [96], while pressure, temperature and mass flow rate were measured as indicated in the figure (PT, TT and MF, the latter with a Coriolis sensor characterized by ±0.5% accuracy [96], respectively).

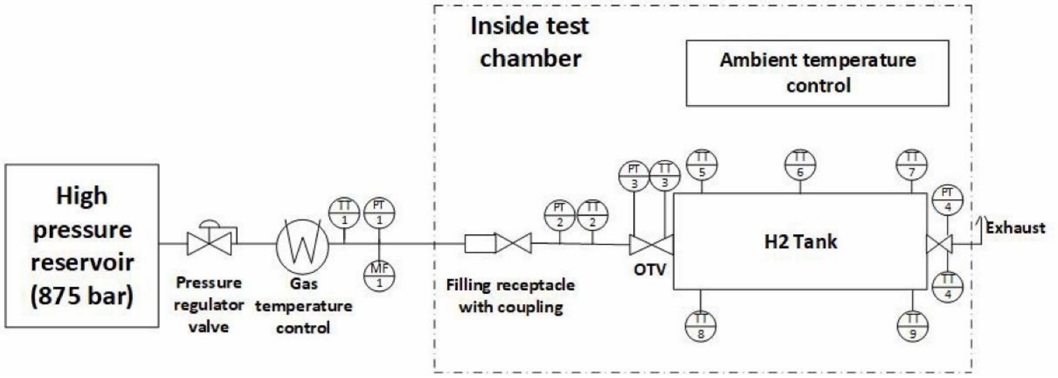

Figure 2.2 - Simplified layout of piping and instrumentation of the test rig.

Starting from the available data (i.e. time, hydrogen pressure before the tank, hydrogen temperature after the cooling unit, mass flow from dispenser, measured tank pressure) obtained from experimental measurement, the cumulative mass of the gas inside the tank, the gas density profile and the average gas temperature were calculated, as indicated in Equation (1).

$$\left[m_{cum,H_2} = m_{in} + \dot{m}\ \cdot \Delta t\right]\ ;\ \left[\rho_{H_2} = \frac{m_{cum,H_2}}{V}\right]\ ;\left[T_{H_2} = f\left(p_{H_2}, \rho_{H_2}\right)\right] \qquad (1)$$

where m_{cum,H_2} is the cumulative mass, m_{in} is the initial mass inside the tank, $\dot{m}$ is the mass flow from dispenser, Δt indicates the time step of the measurement simulation, ρ_{H_2} represent the density profile, V is the tank volume, T_{H_2} is the average temperature of hydrogen inside the tank, calculated with CoolProp [97] starting by gas pressure and density. In particular, only 2 cases were analysed and validated of the 3 reported in the reference study (due to data availability) [96]: Test no. 4 and Test no. 12. The characteristics of these tests, as well the initial simulation data, are reporter in Table 2.1.

Table 2.1 - Initial data for Test no. 4 and Test no. 12 simulations [96].

		Test no. 4	**Test no. 12**
Tank volume	[m^3]	0.32	0.32
Pressure ramp rate	[bar/min]	50	100
Pre-cooling	[°C]	-40	0
Ambient temperature	[°C]	15	15
Starting gas temperature	[°C]	15.06	15.35
Starting gas pressure	[bar]	30.32	29.47
Starting gas mass	[g]	801.56	778.71
Starting gas density	[kg/m^3]	2.505	2.433

The VT was than modelled thermodynamically as reported in [98]. Starting with the conservation of mass and energy, the two balances are written in Equation (2) and Equation (3).

$$\frac{dm}{dt} = \dot{m}_{in} - \dot{m}_{out} \qquad (2)$$

$$m \cdot \frac{du}{dt} + u \cdot \frac{dm}{dt} = \dot{m}_{in} \cdot h_{in} - \dot{m}_{out} \cdot h_{out} - \dot{Q}_{H_2w} \qquad (3)$$

where m and $\dot{m}$ are the mass stored and the mass flowrate of hydrogen, respectively, in and out represent the refuelling and emptying phases, t represent the time, u is the internal energy per unity of mass, h is the enthalpy and $\dot{Q}_{H_2w}$ represent the heat transfer from the gas to the tank wall, obtained with Equation (4).

$$\dot{Q}_{H_2w} = A_{in} \cdot k_{H_2} \cdot \left(T_{H_2} - T_w\right) \qquad (4)$$

where A_{in} is the inner surface area of the tank, k_{H_2} is the heat transfer coefficient and T_{H_2} and T_w indicate the gas and wall temperature, respectively.

The heat transfer coefficient is calculated exploiting the Nusselt number (Equation (5)), expressed depending on the Reynolds number, Re, and the Rayleigh number, Ra (Equation (6)) [55].

$$Nu = \frac{k_{H_2}}{\lambda / D_{int}} = a_1 \cdot Re^{b_1} + a_2 \cdot Ra^{b_2} \tag{5}$$

$$\left[Re = \frac{4 \cdot \dot{m}}{n_{tank} \cdot \pi \cdot \mu \cdot D_{nozzle}} \right] \; ; \; \left[Ra = \frac{g \cdot \tau \cdot \left(T_{H_2} - T_w \right) \cdot c_p \cdot \rho^2 \cdot D_{int}^3}{\mu \cdot \lambda} \right] \tag{6}$$

where λ is the thermal conductivity, D_{int} is the characteristic length or internal diameter of the tank (since all tanks were assumed to be positioned horizontally), a_1, b_1, a_2, b_2 are specific coefficient and exponents for the Re and Ra numbers, n_t is the total number of tanks, μ is the dynamic viscosity, D_{nozzle} is the nozzle diameter, g is the gravity acceleration, τ is the isobaric expansion coefficient, c_p is the specific heat at constant pressure and ρ is the gas density. Regarding the coefficient and exponents for the Re and Ra numbers, a_1 and b_1 were assumed equal to 0.021 and 0.67, respectively, while a_2 and b_2 are equal to 0.004 and 0.352, respectively [96]. These values were kept constant for each tank.

Solving the mass balance equation is possible to calculate the hydrogen mass inside a tank at each time step i, according to Equation (7).

$$\frac{dm}{dt} = \dot{m}_{in} - \dot{m}_{out} \rightarrow m_i = m_{i-1} + \left(\dot{m}_{in,i} - \dot{m}_{out,i} \right) \cdot \Delta t_i \tag{7}$$

Since the hydrogen mass is known, is possible to calculate the SOC of the tanks, SOC_i, and the hydrogen pressure, p_i, as reported in Equation (8).

$$\left[SOC_i = \frac{m_i}{m_{NOM}} \right] \; ; \; \left[p_i = \frac{m_i \cdot Z_i \cdot T_{H_2,i} \cdot R}{MM_{H_2} \cdot V_{tank}} \right] \tag{8}$$

where m_{NOM} is the nominal mass, Z_i is the compressibility factor (considering hydrogen a real gas), R is the gas constant, MM_{H_2} is the hydrogen molecular mass and V_{tank} is the tank volume. In particular, Z_i was calculated for each time step with CoolProp, considering the measured tank pressure and the average temperature of the gas calculated as reported before.

As can be seen, the hydrogen pressure depends on the temperature of the gas inside the tank, $T_{H_2,i}$, which can be found solving the energy balance (Equation (2)) and making some consideration. In fact, since $u_i = c_{v,i} \cdot T_{H_2,i}$, $h_{in,i} = c_{p,i} \cdot T_{in,i}$ and $h_{out,i} = c_{p,i} \cdot T_{out,i}$ (where c_v is the specific heat at constant volume and T_{in} is the temperature of the supplied hydrogen) it is possible to arrive at simplified relations of the variation in time of the hydrogen $\left(\frac{dT_{H_2}}{dt} \right)$ and wall $\left(\frac{dT_w}{dt} \right)$ temperatures, as indicated in Equation (9) [74,99] and Equation (11) [74], respectively. The parameters used to obtain the gas temperature are reported in Equation (10).

$$\left[\frac{dT_{H_2}}{dt} = (1+\alpha_i)\frac{T_i^* - T_{H_2,i}}{t_i^* + t}\right] \tag{9}$$

$$\left[\alpha_i = \frac{A_{in} \cdot k_{H_2,i}}{\dot{m}_\imath \cdot c_{V,i}}\right]; \left[t_i^* = \frac{m_0}{\dot{m}_\imath}\right]; \left[T_i^* = \frac{\alpha_i \cdot T_{w,i} + \gamma_i \cdot T_{in}}{1+\alpha_i}\right]; \left[\gamma_i = \frac{c_{p,i}}{c_{V,i}}\right] \tag{10}$$

$$\left[\frac{dT_w}{dt} = \frac{T_{w,i} - T_{H_2,i}}{t_{w,i}^*}\right]; \left[t_{w,i}^* = \frac{m_w \cdot c_{p,w}}{A_{in} \cdot k_{H_2,i}} = \frac{\rho_w \cdot V_{tank} \cdot c_{p,w}}{A_{in} \cdot k_{H_2,i}}\right] \tag{11}$$

where α, T^*, t^* and t_w^* are coefficients calculated as indicated in Equation (8) and (9), m_0 is the initial hydrogen mass inside the tank, γ is the ratio between the specific heat at constant pressure and volume, m_w is the mass of the tank, calculated multiplying the tank density (ρ_w) and volume (V_{tank}), and $c_{p,w}$ is the specific heat of the wall tank.

Since the type III tank is characterized by two materials, the calculation of the wall temperature has been discretized, considering the increasing of the area (A_j) and volume (V_j) of the tank wall, as indicated in Equation (12) and Equation (13), respectively. In particular, it was assumed to consider 10 shell elements for each layer, each one with the same length dx [96].

$$A_j = 2 \cdot \pi \cdot [(r + (j-1) \cdot dx] \cdot L_{int} + 4 \cdot \pi \cdot [(r + (j-1) \cdot dx]^2 \tag{12}$$

$$\begin{aligned} V_j = \pi \cdot [(r + j \cdot dx)^2 - (r + (j-1) \cdot dx)^2] \cdot L_{int} + \frac{4}{3} \cdot \pi \\ \cdot [(r + j \cdot dx)^3 - (r + (j-1) \cdot dx)^3] \end{aligned} \tag{13}$$

where r is the inner radius of the tank, L_{int} is the total internal length of the tank and j indicates the tank layer. The discretization of the wall temperature, as reported in Equation (14), was implemented with different parameters (from x_1 to x_6). Depending on the layer, indexed in the first column of Table 2.2, it is possible to substitute each parameter in Equation (14) to obtain the formula for each layer considered. The subscript l indicates the liner layer (aluminium), while the C the composite one (carbon fibre reinforced polymer).

$$\frac{dT_{w,j}}{dt} = \frac{A_j \cdot x_1 \cdot \left(x_2 - T_{w_j}\right) - A_{j+1} \cdot x_3 \cdot \left(T_{w_j} - x_4\right)}{x_5 \cdot x_6 \cdot V_j} \tag{14}$$

In particular, the first term in the numerator of Equation (14) considers the heat exchanged due to the hydrogen mass flow. Therefore, during filling operations ($\dot{m} > 0$) it influences the temperature increase, while during unloading operations ($\dot{m} < 0$) it determines a temperature decrease. In stand-by conditions (no mass flow), this contribution has been neglected and the evolution of the wall temperature has been calculated considering only the second term, which represents the heat exchange between the tank wall and the surrounding environment. In these conditions, in fact, the gas temperature remains approximately constant, while the wall temperature tends to approach thermal equilibrium with the ambient temperature.

Table 2.2 - Different parameters used to calculate the tank wall temperature.

	x_1	x_2	x_3	x_4	x_5	x_6
$j = 1$	$k_{H_2,i}$	T_{H_2}	λ_l/dx_l	$T_{w_{j+1}}$	ρ_l	c_{p_l}
$1 < j < 10$	λ_L/dx_l	$T_{w_{j-1}}$	λ_l/dx_l	$T_{w_{j+1}}$	ρ_l	c_{p_l}
$j = 10$	λ_l/dx_l	$T_{w_{j-1}}$	$\frac{\lambda_l + \lambda_C}{dx_l + dx_C}$	$T_{w_{j+1}}$	ρ_l	c_{p_l}
$j = 11$	$\frac{\lambda_l + \lambda_C}{dx_l + dx_C}$	$T_{w_{j-1}}$	λ_C/dx_C	$T_{w_{j+1}}$	ρ_C	c_{p_C}
$11 < j < 20$	λ_C/dx_C	$T_{w_{j-1}}$	λ_C/dx_C	$T_{w_{j+1}}$	ρ_C	c_{p_C}
$j = 20$	λ_C/dx_C	$T_{w_{j-1}}$	$k_{H_2,out}$	T_{amb}	ρ_C	c_{p_C}

All the values dependent on the gas pressure and temperature, as c_p c_v, μ, h, u, λ, τ and ρ were obtained by Coolprop, as a function of pressure and temperature, at each time step. The main parameters of the VT, such the geometry and material properties, are reported in Table 2.3.

Table 2.3 - Properties of the VT tank validated [96].

Parameter		**VT (type III)**
$p_{in} - p_{nom}$	[MPa]	2.99 – 35
$m_{in} - m_{nom}$	[kg]	0.779 – 7.68
V_{tank}	[m^3]	0.32
$D_{int} - D_{ext}$	[m]	0.337 – 0.417
$L_{int} - L_{ext}$	[m]	3.05 – 3.13
Tank Thickness – dx	[m]	0.04 – 0.002
D_{noozle}	[mm]	6
$\lambda_l - \lambda_C$	[W/mK]	202 – 1
$\rho_l - \rho_C$	[kg/m^3]	2 700 – 1 494
$c_{p,l} - c_{p,C}$	[J/kgK]	900 – 938
k_{out}	[W/m^{2}K]	8

The results obtained from the Matlab-Simulink model, compared to the experimental values, are reported in Figure 2.3 for Test no. 4 and in Figure 2.4 for Test no. 12. For both tests are reported the pressure (left) and gas temperature (right) profile. Regarding the pressure profile, the blue line indicates the pressure measured immediately before the tank, while the orange line is the gas pressure measured inside the tank. The yellow line indicates, finally, the value obtained with the Matlab-Simulink model. As for the temperature, the blue line represents the average temperature value calculated with the measurement data, as explained previously. The orange and yellow lines represent, respectively, the gas and wall temperature obtained with the Matlab-Simulink model.

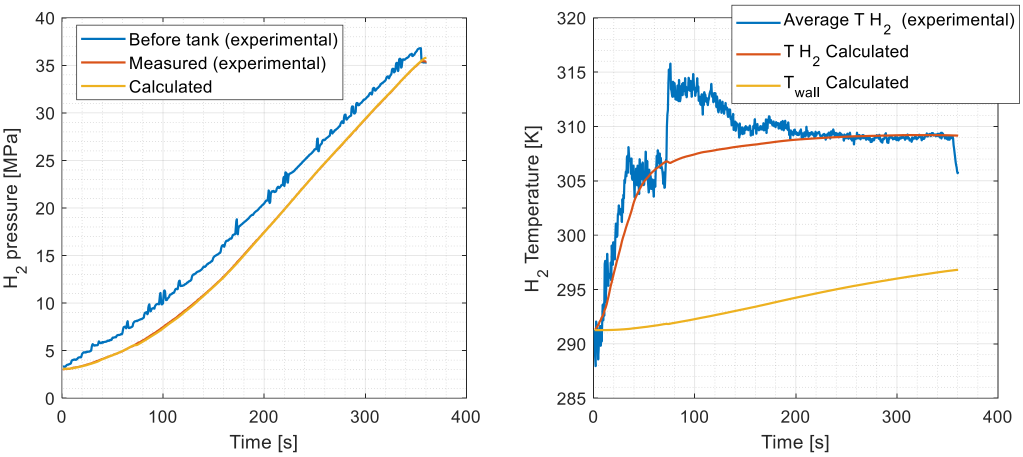

Figure 2.3 - Comparison between experimental and calculated values for Test no. 4.

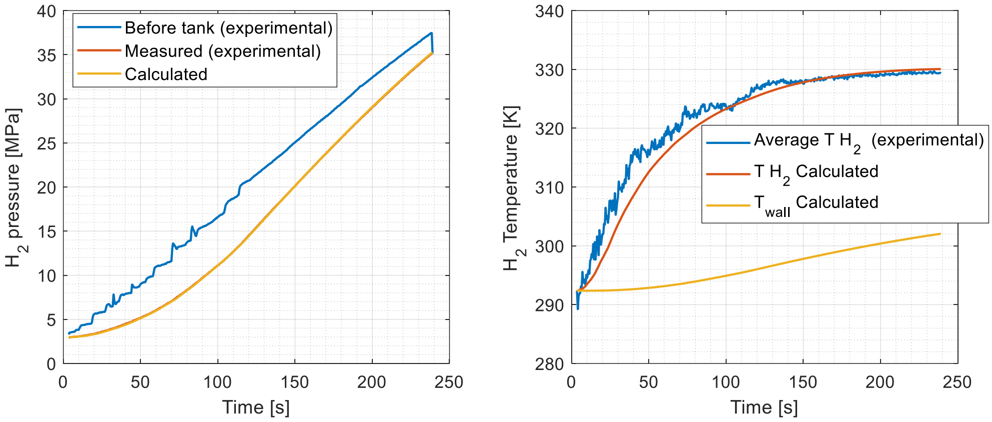

Figure 2.4 - Comparison between experimental and calculated values for Test no. 12.

As can be seen in both figures, the model results of the gas pressure inside the tank for both tests is very similar to the experimental values. Regarding the gas temperature, the results obtained with the model have a more linear trend compared to the experimental data, which show greater variability, especially in Test no. 4. In this case, the simulation data presents some inconsistencies, suggesting potential issues during the measurement process. To evaluate the error between the experimental values and the ones calculated with the Matlab- Simulink model, the Root Mean Square Error ($RMSE$) and its percentage value, compared to the average of the experimental values ($RMSE_{\%}^{MEAN}$), were calculated with Equation (15).

$$\left[RMSE = \sqrt{\frac{1}{n}\sum_{i=1}^{n}\left(y_i - \hat{y}_i\right)^2}\right] \; ; \; \left[RMSE_{\%}^{MEAN} = \frac{RMSE}{\frac{1}{n}\sum_{i=1}^{n} y_i} \cdot 100\right] \qquad (15)$$

where n indicates the number of measurement data, y_i are the experimental values and $\hat{y}_i$ are the results calculated with the model at each time step. The results are summarized in Table 2.4. As can be noted, the percentage error is always lower than 1% for both pressure and temperature. Regarding the absolute error for temperature, this is just a bit lower or greater than 2.5 K, depending on the test, while for pressure the values are very low and included between ~0.05 and ~0.07 MPa.

Table 2.4 - Error results for Test no. 4 and Test no. 12.

	Test no.4		**Test no. 12**	
	$\boldsymbol{RMSE}$	$\boldsymbol{RMSE_{\%}^{MEAN}}$	$\boldsymbol{RMSE}$	$\boldsymbol{RMSE_{\%}^{MEAN}}$
Pressure	0.0731 MPa	0.438 %	0.0514 MPa	0.316 %
Temperature	2.682 K	0.87 %	2.468 K	0.766 %

Given that the error results fall within acceptable limits, the validated model of the VT was adopted as the basis for the modelling of both low- and high-pressure storage tanks.

2.2 Mathematical modelling and characteristics of the LPT, HPTs and VTs of the studied HRS

The LPT and HPT considered are a type I and a type IV tank, respectively, with the first modelled from data from [100], while the VTs are type III tank, as the tank validated before. As reported previously, the VTs are 6, accordingly with the hydrogen bus chosen for this study [101] .

The different types of tanks were modelled with the same principles used for the VT validation (from Equation (2) to Equation (13)). However, unlike the VT validation, no experimental data are available for the case study. For this reason, the increase in VT pressure during the refueling phase was calculated considering a constant APRR, as given in equation (16).

$$p_{VT,i} = p_{VT,(i-1)} + APRR \cdot t_i \tag{16}$$

where $p_{VT,i}$ and $p_{VT,(i-1)}$ are the gas pressure at time t_i and $t_{(i-1)}$, respectively. The hydrogen mass inside the VT was then calculated by multiplying the tank volume and density (obtained with Coolprop as a function of pressure and temperature), while the mass flowrate is a result of Equation (7), since the mass is known.

Since the mass flowrate required by the VTs is known, this value was used to empty the HPT cascade system. In particular, the emptied HPT depends on the pressure inside both tanks (HPT and VT). Logically, the first HPT to be emptied is the one at 35 MPa, while the last one is the 45 MPa tank. Since the mass flow of the HPTs is known, all other parameters can be calculated.

The LPT was modelled similarly to the HPT modelling, considering in this case the compressed hydrogen as mass flow rate to refuel the cascade system. Furthermore, since Type I tanks are characterized by a single material, the discretization of the tank wall temperature in Equation (12) was calculated differently. In particular, only 3 discretization steps of Table 2.2 for the individual layers are considered: the first ($j = 1$), the second (with $1 < j < 20$, where λ, ρ, c_p and dx are the same for each layer), and the last one ($j = 20$). All other parameters were calculated similarly to the other tank types.

The main parameters of the tanks considered in this study are reported in Table 2.5. Regarding geometries, all tank types were scaled starting from data reported in [98].

Table 2.5 - Characteristic of the different tank types considered.

Parameter		**LPT**	**HPT1**	**HPT2**	**HPT3**	**VT**
Type		I	IV	IV	IV	III
p_{nom}	[MPa]	3.5	45	40	35	35
m_{nom}	[kg]	425.32	36.03	39.46	41.39	5.83
V_{tank}	[m^3]	150	1.25	1.5	1.75	0.27
D_{int}	[m]	2.689	0.693	0.737	0.776	0.328
D_{ext}	[m]	2.856	0.757	0.805	0.847	0.406
l_{int}	[m]	24.17	2.849	3.028	3.188	2.97
l_{ext}	[m]	24.5	2.913	3.096	3.259	3.05
AR	[-]	8.58	3.85	3.85	3.85	1.24
s	[mm]	83.5	32	34	35.5	39
dx	[mm]	4.175	1.6	1.7	1.775	1.95
d_{inlet}	[mm]	10.8	5.4	5.4	5.4	6
λ_L	[W/mK]	50	0.3	0.3	0.3	202
ρ_L	[kg/m^3]	7850	1050	1050	1050	2700
$c_{p,L}$	[J/kgK]	490	1700	1700	1700	900
λ_C	[W/mK]	50	0.43	0.43	0.43	1
ρ_C	[kg/m^3]	7850	1560	1560	1560	1494
$c_{p,C}$	[J/kgK]	490	1102	1102	1102	938
$k_{h,outer}$	[W/m^{2}K]	100	100	100	100	8

The nominal pressure of the LPT is equal to the hydrogen production pressure in the HG, while that of the HPT cascade system is able to refuel the VT at 35 MPa. The three-stage cascade configuration (HPT1 at 45 MPa, HPT2 at 40 MPa, and HPT3 at 35 MPa) was selected as the optimal balance between refueling efficiency and system complexity [102]. Studies demonstrate that three to four tanks represent the optimal configuration for cascade systems, as adding more than four tanks yields energy savings of less than 4% per additional tank [102]. A two-tank cascade would result in excessive pressure drops and longer refueling times, particularly in the final phase when the VT approaches 35 MPa, as insufficient pressure differential significantly reduces mass transfer rates [103]. Conversely, a four-tank system would provide only marginal improvements while significantly increasing capital costs, space requirements, and maintenance complexity [102]. The chosen three-stage configuration with approximately 5 MPa pressure steps ensures adequate pressure differentials throughout the refueling process, maintaining sufficient mass flow rates. Research shows that transitioning from a single-tank to a three-tank cascade system reduces total energy consumption by approximately 30-34% [102,104], while the cascading approach optimizes station storage management by minimizing pressure differentials between refueling and refueled tanks throughout the process [103]. This pressure gradient allows approximately 70-80% of the hydrogen stored in each HPT to be effectively transferred to the downstream tank before pressure equalization limits further transfer, thus maximizing the usable capacity of each vessel [105]. Regarding the dimensions, the total volume of the 6 VTs was obtained to contain in total 35 kg of hydrogen, nominal quantity of hydrogen storable in the bus chosen [101].

2.3 Mathematical modelling of the Hydrogen Compressor

The main of the HC is to compress the hydrogen from the pressure coming from the LPT to the nominal pressure of the HPT during its refueling phase. i.e. 35, 40 or 45 MPa. The HC considered in this study is a volumetric compressor (continuously operating with variable load and pressure), which has been modelled to avoid a final temperature after compression above 135 °C [106] with the same principles indicated in [98]. Considering a gas inlet temperature always equal to 15 °C (due to an intercooler before each stage), a minimum pressure of 1.5 MPa (allowing LPT to discharge in a range between 1.5 MPa and 3.5 MPa), and the maximum pressures required by the HPTs, it is necessary to have at least 3 stages. The average compression ratio for a final pressure of 35 MPa, 40 MPa and 45 MPa, $\beta_{(k)}$, are equal to 2.86, 2.99 and 3.11 respectively. It should be noted that, if the inlet pressure is higher than the minimum accepted value, the compression ratios will be lower. Furthermore, with lower compression ratios the final temperature after compression will also be lower, making the system safer.
Each stage of the compressor, including the intercooler at the end of the stage, was modelled the same way. Figure 2.5 shows a simplified scheme of a generic stage k, with all parameters calculated before or after the stage (indicate as HC(k)) and the intercooler (IC(k)).

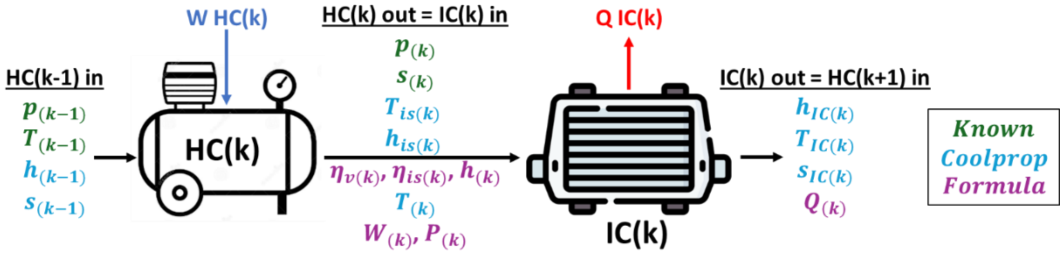

Figure 2.5 - Simplified scheme for a compressor stage

Starting from the initial conditions of pressure and temperature (before the first stage) it is possible to define enthalpy (h) and entropy (s) with Coolprop. The conditions in the middle of the first stage were obtained considering constant entropy and intermediate pressure, through which the isentropic temperature and the isentropic enthalpy ($h_{is(k)}$) were calculated. These last values were then used to find the stage outlet enthalpy ($h_{(k)}$), as a function of the isentropic efficiency (Equation (17), valid for compression ratios between 1.1 and 5 [107]), and the outlet temperature ($T_{(k)}$) with Coolprop.

$$\eta_{is(k)} = 0.1091 \cdot \left(ln\, \beta_{(k)}\right)^3 - 0.5247 \cdot \left(ln\, \beta_{(k)}\right)^2 + 0.8577 \cdot ln\, \beta_{(k)} + 0.3727 \quad (17)$$

As mentioned, an intercooler was modelled at the end of each stage to keep the outlet temperature equal to 15 °C. The same approach was adapted for all stages. At the end of each stage, it is possible to calculate the power needed (Equation (18)), while by adding the power of each stage the total power of the compressor can be obtained.

$$P_{(k)} = \frac{\dot{m}_{H_2} \cdot \left(h_{(k)} - h_{(k-1)}\right)}{\eta_{is(k)} \cdot \eta_{v(k)}} \tag{18}$$

where $P_{(k)}$ is the instantaneous power of a generic stage and $\eta_{v(k)}$ is the stage volumetric efficiency, calculated with Equation (19) [107].

$$\eta_{v(k)} = 1 - \beta_{(k)} - cc \cdot \left(\frac{Z_{in}}{Z_{out}} \cdot \beta_{(k)}^{1/\gamma} - 1\right) \tag{19}$$

where cc is the cylinder clearance (assumed equal to 10%) and Z_{in} and Z_{out} are the compressibility factors at the inlet and outlet conditions considering all stages, respectively.

2.4 Mathematical modelling of Expansion Valves and Hydrogen Pre-Cooling

As shown in Figure 2.1, different valves are located between the components: 1 is located between the LPT and HC, while 3 valves are located before and after the HPT cascade system. The expansion valve located between the HPT cascade system and the VT have the important role of regulating the pressure between the two mentioned components to keep the APRR constant. In fact, during refuelling, the valve is electronically regulated to create a pressure gradient between inlet and outlet equal to the APRR value. This is possible by instantly changing the valve passage section, which determines the variation of the mass flow rate through it. During the expansion process two simplifications were adopted: 1. the heat exchanged with the environment is zero (adiabatic process) and 2. the variation of kinetic energy is zero. This means that the enthalpy remains constant. These considerations help to find the valve outlet temperature, or the inlet temperature of the VTs. In fact, since the HPT and VT pressures are known, as well as the temperature of the HPT, it is possible to find the required temperature with Coolprop. All the other valves were modelled with the same principles, thus considering an adiabatic process and a constant enthalpy.

Regarding hydrogen pre-cooling, this was modelled with the same equation used in HC intercooling to calculate heat removal from hydrogen. Since the mass flow rate at the VT inlet is known, along with the enthalpy and inlet pressure (which vary depending on the HPT tank emptying) and the desired final temperature to which the hydrogen must be cooled, the outlet enthalpy was obtained using CoolProp. The heat to be removed from the gas was then calculated by multiplying the mass flow rate by the enthalpy difference between the initial and final states. Regarding electrical energy consumption, since the hydrogen cooling temperature per SAE J2601-5 ranges from -40°C to 0°C, different Coefficients of Performance (COP) were considered depending on the cooling temperature, as reported in Table 2.6

[108]. The electrical power of the cooler was therefore obtained by dividing the thermal power Q by the COP.

Table 2.6 - Different COP for hydrogen cooling temperature.

Cooling T [°C]	-40	-30	-20	-10	0
COP	1.95	2.2	2.55	3	3.4

2.5 Strategy Management and Control Logic for HRS

The HRS management strategy was designed to determine the maximum number of buses that can be refueled within one hour. A two-minute pause between consecutive refueling events was assumed, while each refueling process was modelled in compliance with the SAE J2601-5 protocol limits for pressure and temperature. Considering a theoretical capacity of the HRS, at the start of each simulation each VT was considered to be refueled from 10% to 100% SOC, whereas the LPT and HPT were assumed to be fully charged (SOC = 100%).

To evaluate how many buses can be refueled within the selected time frame, the VT model was implemented in a loop. Once a refueling is completed, a two-minute pause is simulated during which the main VT parameters (time, pressure, temperature, and hydrogen mass inside the tank) are reset. The methodology used to calculate all the HRS outputs is represented in Figure 2.6, which highlight the most relevant output calculated for each block modelled with Matlab-Simulink.

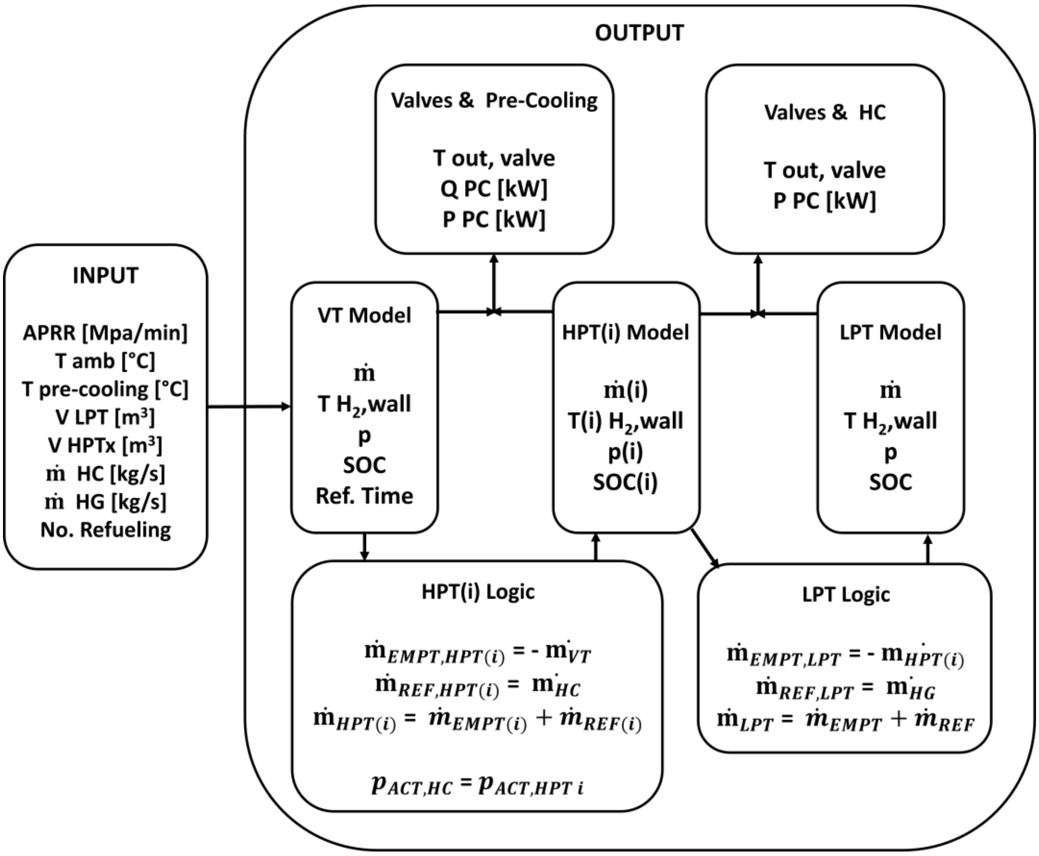

Figure 2.6 - Most relevant HRS output calculation logic.

The key output of each VT simulation is the mass flow rate requested by each of the six VTs, which is identical, and calculated as a function of the APRR. This flow rate is essential to determine the overall outflow from the HPT cascade system, equal to the sum of the mass flow rates requested by all VTs. Specifically, hydrogen is discharged from the HPT whose pressure is higher than that of the VT being refueled. Since at the beginning of the simulation the VTs are nearly empty and all HPTs are fully charged, priority is given to the HPT with the lowest pressure, i.e., HPT3 (35 MPa), followed by HPT2 and HPT1 in order of increasing pressure.
To maximize the number of buses that can be refueled in one hour, a parallel refueling logic for the HPT cascade system was implemented. The HPT logic is represented in Figure 2.7, where *i-1* highlights the priority of HPT3.

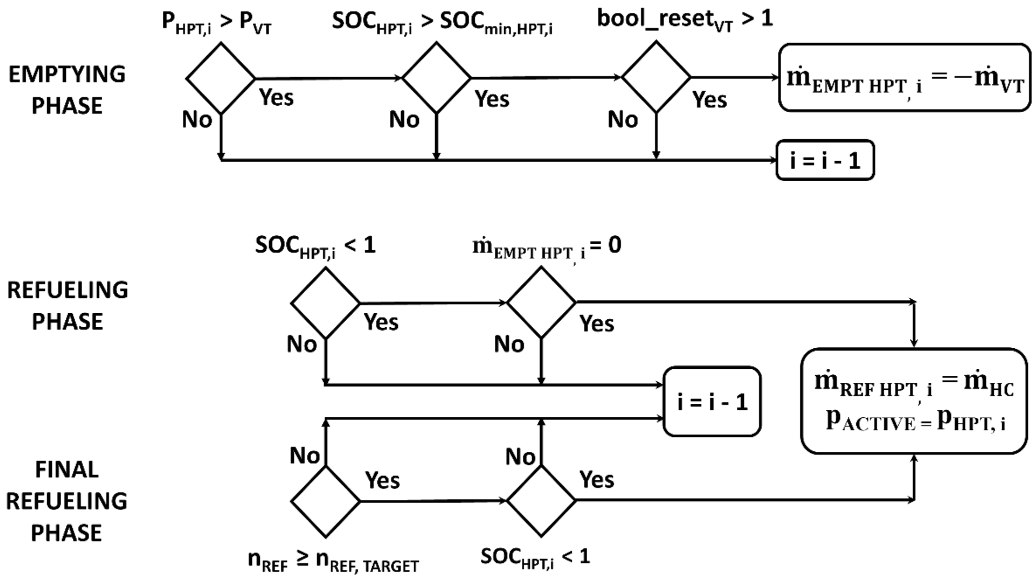

Figure 2.7 - HPT cascade system control logic.

In particular, whenever a tank in the cascade is not discharging, it is refilled if its SOC is below 100%. Again, priority is given to the tank with the lowest pressure, i.e., HPT3. For instance, during the initial phase of VT refueling, HPT3 supplies hydrogen to the VTs until its pressure becomes equal to or lower than that of the VTs. At that point, HPT3 can no longer refuel the VTs, and HPT2, characterized by a higher pressure, takes over from HPT3. Simultaneously, HPT3, which is no longer discharging and has an SOC lower than 100%, can be refueled to its nominal pressure with compressed hydrogen from the LPT. The same logic is applied when HPT1 takes over refueling once HPT2 can no longer provide hydrogen at a sufficient pressure. In this case, if HPT3 has not yet reached 100% SOC or is not required to supply the VTs again, it continues to refuel; otherwise, HPT2 is refueled. HPT1 is refueled during this mixed phase only if HPT3 and/or HPT2 have reached 100% SOC and one of them is discharging to the VTs. Finally, at the end of the one-hour period, a final refueling is carried out so that the cascade system is restored to its initial condition (SOC = 100%). Within this management logic, both the HPT tank selected for discharge and the corresponding mass flow rate (during discharging and refueling phases) and the compression pressure, depending on which HPT tank is being refilled, are determined.

Other key parameters derived from calculations within the VT and hydrogen storage system include pressure, gas and wall temperatures, mass and SOC. Given the pressure and temperature values of the HPT cascade system and the pressure of the VTs, it is possible to compute the outlet temperature at the valves located downstream of the cascade system.

Moreover, depending on which valve is active (based on the hydrogen flow from the HPT currently being discharged) it is possible to determine the amount of heat that must be removed from hydrogen during the cooling phase, as well as the corresponding electrical consumption, as previously described.

Similarly, the mass flow rate of the LPT has been calculated. During the discharging phase, this mass flow rate matches the demand from the HPT cascade system. In particular, the HC compresses the hydrogen to the pressure required by the active HPT. Differently from the cascade system, the LPT is refuelled with hydrogen produced by the HG during all day (if its SOC is lower than 100%), considering hydrogen production at nominal power. Thus, the target number of VTs is refuelled every hour, while the cascade system is refueled during and after the VT refueling. The LPT is refueled hourly at the nominal HG production and emptied when required by the buses.

With all relevant parameters known for the LPT, it is also possible to calculate the outlet temperatures at the valves located upstream of the cascade system and at the valve between the LPT and the HC.

2.6 Results of the HRS thermodynamic model

This session reports the results obtained from the HRS model, achieved using the methodology represented in Figure 2.6. In particular, several simulations were conducted to identify the inputs capable of ensuring the desired SOCs (100% for VT and HPT cascade system) and the temperature and pressure limits imposed by SAE J2601-5 protocol with low energy consumptions. The inputs, indicated as base case, are reported in Table 2.7.

Table 2.7 - Input for HRS model – Base Case

Parameter		Value	Parameter		Value
APRR	[MPa/min]	4.5	N. Ref Target	[-]	5
T Amb	[°C]	20	T Pre-Cooling	[°C]	-10
SOC VT	[%]	10	V VT	[m^3]	0.27
SOC $HTP_{1,2,3}$	[%]	100	V $HPT_{1,2,3}$	[m^3]	1.25/1.5/1.75
SOC LPT	[%]	100	V LPT	[m^3]	150
MF HC	[g/s]	60	MF HG	[g/s]	14.59

As indicated in the table, a target number of 5 hourly refuelings was selected. The tank volumes are those indicated in Table 2.5, which also reports the geometric and material characteristics. As previously reported, the VT starts from an SOC of 10%, while the storage tanks are completely full at the beginning of the simulation. An ambient temperature of 20°C was chosen, while hydrogen is supplied at a temperature of -10°C. The mass flow rate required by the VT is influenced by the required APRR, set at 4.5 MPa/min, while the compression and hydrogen production mass flow rates were initially selected as 60 g/s and 14.59 g/s respectively. In particular, the hydrogen production value of 14.59 g/s was selected based on the bus demand considered in this case study, which will be explained subsequently. This mass flow rate is capable of refuelling the LPT and bringing it back to an SOC of 100% at the end of a working day, always ensuring the hydrogen required by the buses during their respective refuelling hours. With these values, it is possible to reach the desired number of refuelings without exceeding the pressure and temperature limits, while also ensuring the refuelling of the cascade system within one hour. The main results, obtained at the end of the simulation, are visible in Table 2.8.

Table 2.8 - Results obtained from the base case simulation.

Parameter		Value	Parameter		Value
Ref. Time	[min]	7.15	No. Ref.	[-]	5
Max p VT	[MPa]	34.79	Max T H_2 VT	[°C]	51.05
Max p HTP1	[MPa]	47.12	Max T HTP1	[°C]	33.63
Max p HTP2	[MPa]	44.3	Max T HTP2	[°C]	49.93
Max p HTP3	[MPa]	41.69	Max T HTP3	[°C]	73.53
Max p LPT	[MPa]	3.5	Max T LPT	[°C]	20
SOC VT	[%]	100	SOC $HTP_{1,2,3}$	[%]	100
SOC LPT	[%]	72.31	Max MF Disp.	[g/s]	83.26
Max HC Power	[kW]	448.4	HC Consumption	[kWh]	287.24
Max PC Power	[kW]	32.72	PC Consumption	[kWh]	11.55

As just mentioned, the final number of refuelings equals the desired value of 5. With the considered APRR each refuelling takes just over 7 minutes in total, for a total of approximately 45 minutes dedicated to vehicle refuelling (considering a 2-minute pause between consecutive refuelings). This means that the final SOC of each VT is 100%, as well as the HPT cascade system tanks are also completely refuelled by the end of the hour. Regarding the LPT, this tank is refueled up to 100% throughout the day. The maximum flow rate delivered by the dispenser is 83.26 g/s, which is uniformly distributed among the 6 VTs present in one bus.

The pressure limit is respected in every tank, based on the limit imposed by the J2601-5 standard at a value equal to 25% above the nominal working pressure (1.25·NWP). These limits are, specifically, 43.75 MPa for the VT and HPT3, 56.25 MPa for HPT1, 50 MPa for HPT2, and 4.375 MPa for the LPT. From the results, it can be observed that the final pressure value of the VT is slightly lower than the nominal value, while in the other tanks the value is slightly higher or equal, but still within the limits. This difference is due to the different pressure calculation for the VT, set as a function of the APRR, and for the storage tanks, for which the pressure is obtained as a function of the ideal gas equation, depending on the established mass flow rates in the downstream tanks. Furthermore, the nominal value is exceeded due to the mass increase inside the tank, and consequently the temperature increase.

The temperature limit of 85°C is also not exceeded. The tank that comes closest is the HPT3, which is the most stressed during the vehicle refuelling phase and during the refuelling phase through compressed hydrogen, reaching a value of approximately 74°C.

Regarding power of HC and Pre-Cooling, the first reached a maximum power of almost 450 kW, while the second reached only 32.72 kW, which is 7.27% of the compressor. The energy consumption values were obtained integrating the power over the considered hourly interval: the results are 287.24 kWh and 11.55 kWh for the HC and PC, respectively.

In the following, the graphical results of the trends of the most relevant parameters (mass flow rate, SOC, pressure and temperature) for all tanks are reported, as well as the consumption and parameters of the HC and PC.

2.6.1 Vehicle Tanks results

Figure 2.8 presents the VT results obtained from the thermodynamic model of the HRS. The graphs show, from top to bottom, the trends of mass flow rate, SOC, pressure, and gas and wall temperatures.

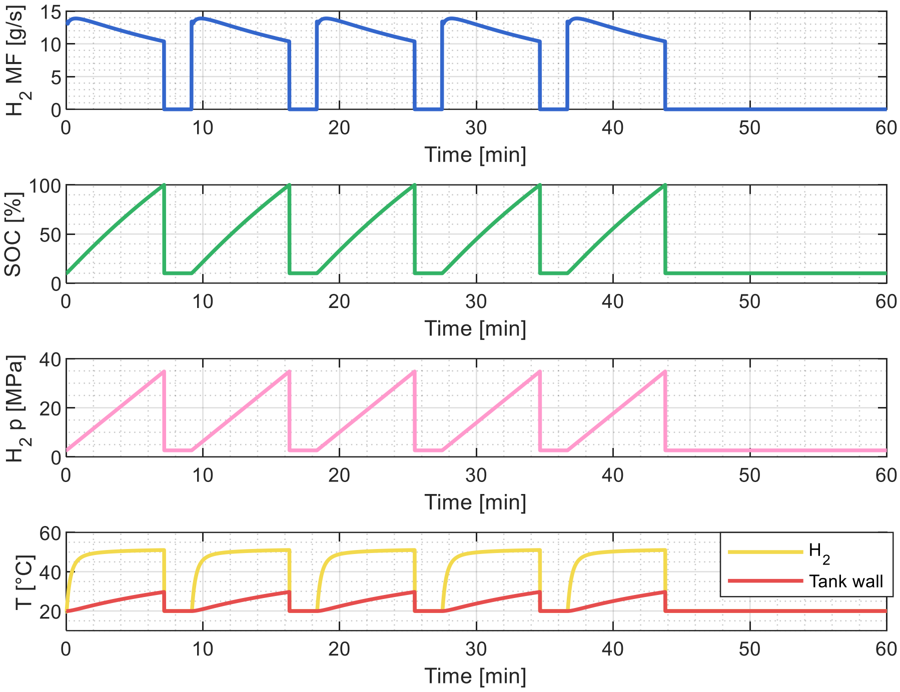

Figure 2.8 - Mass Flow, SOC, pressure and temperature of the VT (base case).

In particular, since each VT is refuelled uniformly, the graph shows the trend of only one VT. This can also be observed in the mass flow rate graph, where the maximum value reached is approximately one-sixth of the maximum flow rate delivered by the dispenser, namely 14.5 g/s. The mass flow rate trend is typical of refuelling with a constant APRR and results from two competing thermodynamic effects. Initially, the mass flow rate increases rapidly due to the greater pressure difference between the HPT cascade system and the VT, which drives hydrogen transfer. However, as refueling progresses, the compression of hydrogen inside the VT causes a significant temperature rise due to the Joule-Thomson heating effect and compression work. This temperature increase reduces the hydrogen density inside the tank, which in turn increases the internal pressure more rapidly than would occur in an isothermal process. Consequently, the pressure differential between the source and the VT decreases faster, leading to a reduction in mass flow rate. The interplay between these two effects, pressure-driven mass transfer (which dominates initially) and temperature-induced pressure rise (which dominates later), determines the characteristic declining mass flow rate profile observed during the refueling process. As the VT pressure approaches that of the active HPT in the cascade, the mass flow rate diminishes until the system switches to the next lower-pressure HPT to continue refueling.

As assumed by the logic, after refuelling a vehicle, a 2-minute pause begins, during which all the most important parameters are reset. At each refuelling, the SOC of each VT starts from 10% to reach a full charge of 100% in approximately 7 minutes, as previously reported. The pressure trend is analogous to that of the SOC, with the maximum value reached close to the nominal conditions. Regarding temperatures, the initial value is equal to that of the ambient temperature (20°C), while the temperature of the hydrogen delivered by the dispenser is close to that set in the PC, equal to -10°C. The highest value reached by the temperature of hydrogen is approximately 51°C. The temperature trend is similar to those of the mass flow rate, characterized by a high increase at the beginning, followed in this case by a more contained increase until the end of the refuelling. This rapid temperature increase at the beginning is due to the low initial pressure and the Joule-Thomson effect. In fact, hydrogen has a negative Joule-Thomson coefficient for the considered temperatures, which means that a free expansion heats it instead of cooling it. The wall temperature assumes lower values instead, with a maximum of approximately 5°C, with an increasing trend.

As mentioned previously, the VT pressure increases thanks to the contribution of all three HPTs, as visible in Figure 2.9, which shows the VT pressure and the active pressure of the cascade system

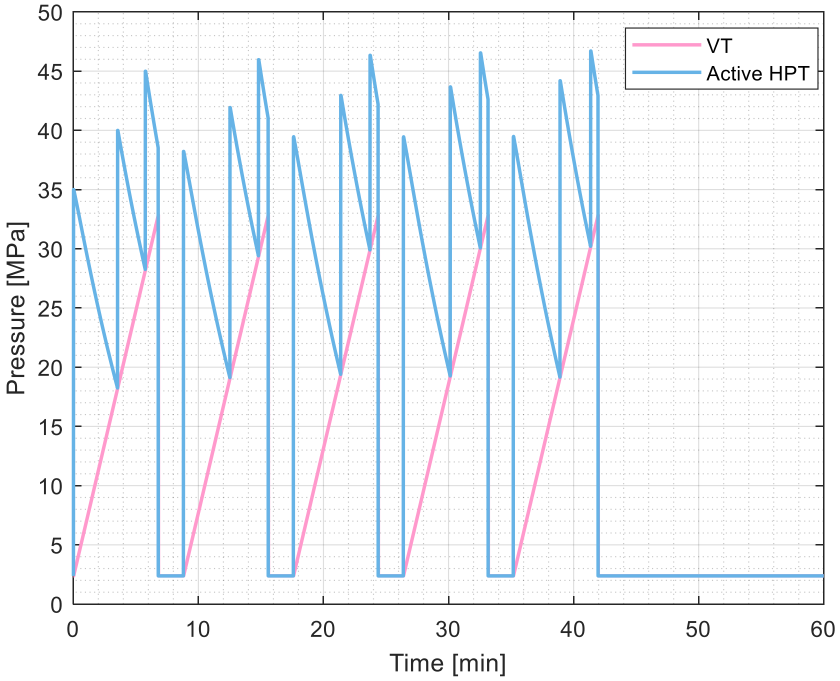

Figure 2.9 - Pressure for VT and Cascade system during refueling.

. As known, in fact, the hydrogen pressure entering the VTs must always be higher than that of the tank. As visible in the figure for all refuelings, the refuelings are ensured by HPT3 up to a pressure close to 18÷19 MPa, by HPT2 from 18÷19 MPa to approximately 28÷30 MPa, and at the end by HPT1 up to the final pressure.

2.6.2 HPT cascade system results

The results of the cascade system control logic are represented in the following figures. Each figure indicates, as already done for the VT, the trends of mass flow rate, SOC, pressure and temperature starting from HPT3, at the top, down to HPT1, at the bottom.

Figure 2.10 shows the mass flow rate trend. As previously reported, the VT is refueled by the cascade system tank characterized by a pressure higher than that of the VT itself. The emptying priority is perfectly visible in the graphs: initially the VT is filled with hydrogen from HPT3 (characterized by an initial negative mass flow rate), after which HPT2 and HPT1 are emptied. This trend is repeated for all refuelings, as visible. Regarding the tank filling logic, HPT3 begins to refuel with compressed hydrogen simultaneously with the emptying of HPT2 (with a mass flow rate equal to that of compression), just as HPT2 begins to refuel as soon as HPT1 starts to empty. Finally, HPT1 refuels during the emptying of HPT3. From the graph, the final filling of each tank can also be observed, which occurs once the desired number of vehicle refuelings is completed (after approximately minute 42). Finally, given the logic set with priority to HPT3 both in the filling and emptying phases, it is possible to observe that this tank is the most used among the three, while for the same reasons HPT1 is the least used.

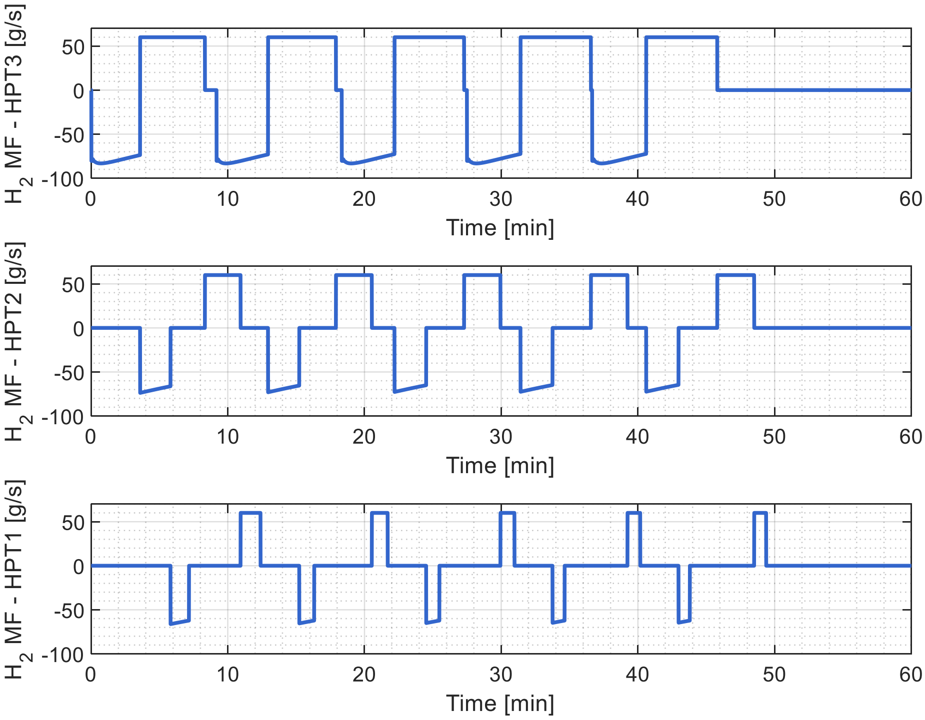

Figure 2.10 - Mass Flow of the HPT3, HPT2 and HPT1 (base case).

Figure 2.11 shows the SOC trend for the cascade system tanks. The SOC was calculated using the Equation (8), considering its variation between the minimum filling value (close to 0%) and 100%, thus the absolute SOC. As just reported, in this case too it is possible to observe how the HPT3 tank is the most used. Its SOC indeed reaches a minimum value close to 50%, while at almost every refuelling it is filled up to 100%. HPT2 instead presents intermediate pause moments between the different refuelings and emptings (also visible in the mass flow rate graph), while the lowest value reached is approximately 75%. Finally, HPT1 presents longer pauses compared to those of HPT2 and reaches a minimum of approximately 85%. The apparently high minimum SOC values for HPT1 (~85%) and HPT2 (~75%) do not indicate oversizing, but are rather a consequence of the adopted logic, which involves cascading emptying until the pressure of the individual HPTs allows it. With smaller volumes, in fact, it is not possible to achieve the required number of refuelings, as the pressures of the storage tanks reach values lower than the vehicle pressure. Each tank reaches a final value of 100%, as previously mentioned, at the moment when the mass flow rate of each tank reaches a zero value at the end of the hour.

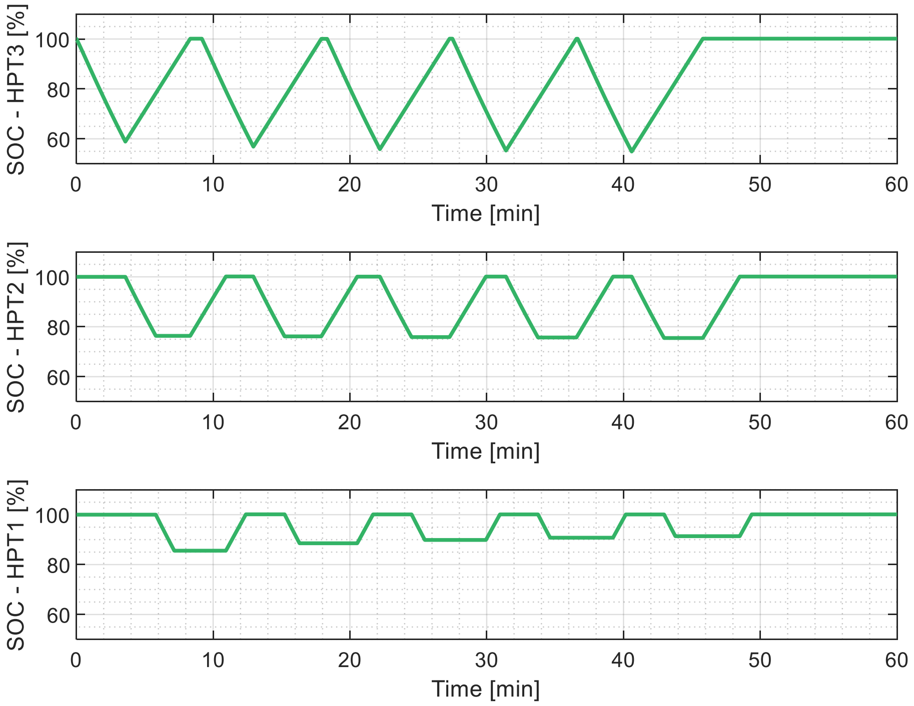

Figure 2.11 - SOC of the HPT3, HPT2 and HPT1 (base case).

Figure 2.12 shows the pressure trends of hydrogen inside each tank. As in the case of the VT, the trend is analogous to that of the SOC. The maximum value of the ordinate scale in the figure reports, in particular, a value close to the limit for each tank. The limits are 43.75 MPa for HPT3, 50 MPa for HPT2, and 56.25 MPa for HPT1 (NWP multiplied by 1.25). As already mentioned, all tanks respect the limit imposed by the SAE J2601-5 standard.

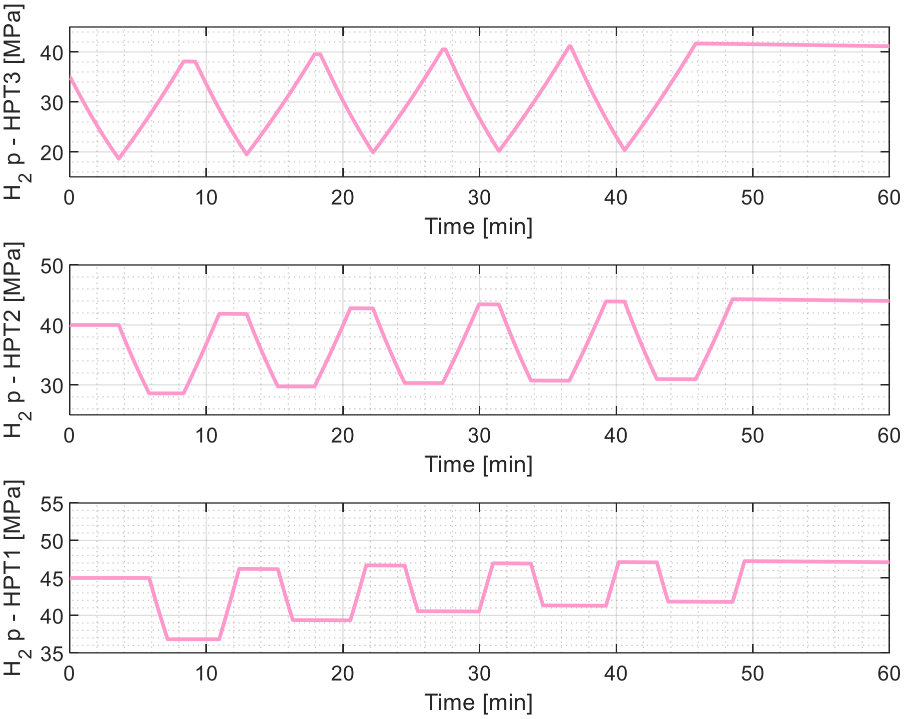

Figure 2.12 - Pressure of the HPT3, HPT2 and HPT1 (base case).

Figure 2.13 finally shows the gas and wall temperature trends for each HPT. Looking at the temperature trends for HPT3, at the beginning both temperatures are characterized by a slight decrease, due to the first emptying phase of the tank. This is followed by an increase in both temperatures, with the gas temperature reaching a slightly higher value. These two phases are followed by a brief pause, also visible in the mass flow rate graph: in this phase, the gas temperature decreases in a very contained and almost imperceptible way, while the wall temperature decreases more evidently, although slightly, trying to reach equilibrium with the ambient temperature.

This temperature decrease leads to the subsequent emptying phase, during which the gas temperature decreases, causing an increase in the wall temperature. The observed phenomenon can be explained considering the thermal inertia and energy exchange between gas and tank walls. When the subsequent emptying phase begins, the pressure decrease causes the gas to cool due to expansion, while the walls are now heated by the gas flow which, although colder, creates turbulence and favours heat exchange from the environment toward the walls. In the subsequent phases, characterized by continuous filling and emptying, both temperatures follow the same trend: they increase during refueling and decrease during emptying. In the final phase, with no flow rate and therefore at rest, both temperatures decrease, with the walls releasing more heat to the outside compared to the temperature released by the gas.

The same trend occurs in HPT2. This tank presents an initial pause phase, followed by emptying, with consequent decrease of both temperatures in a very contained manner. At this point there is another pause, during which the difference in both temperatures is almost imperceptible (before minute 10). This is followed by the first filling, which instead causes a more evident temperature increase, with the gas reaching higher temperatures. Subsequently, another pause occurs, during which the gas slightly decreases its temperature, against a greater decrease in wall temperature. At the next emptying, as already observed, the gas temperature decreases, while that of the walls increases.

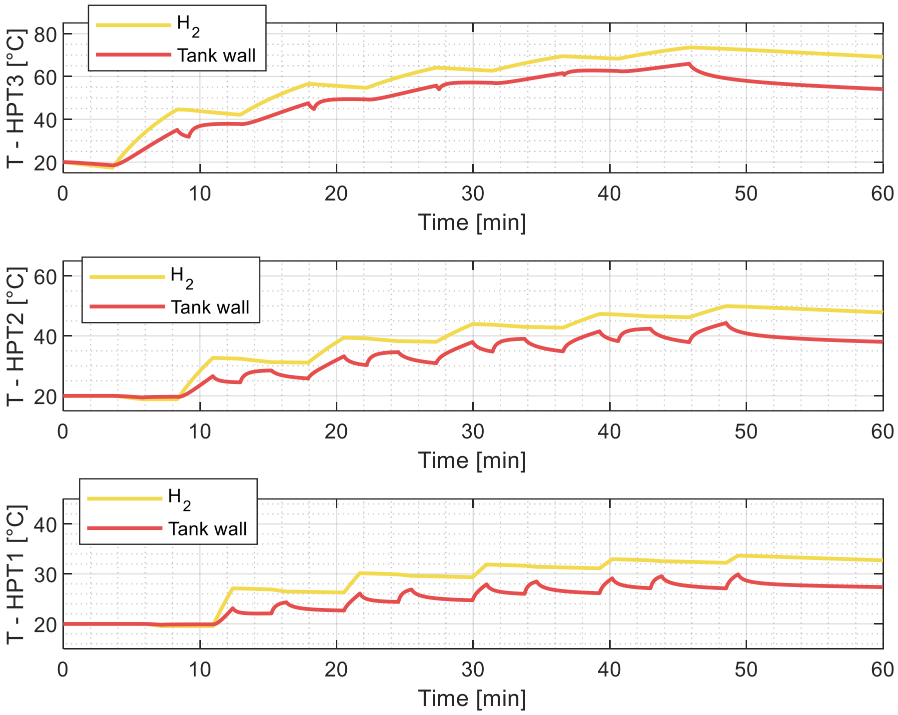

Figure 2.13 - Temperature of the HPT3, HPT2 and HPT1 (base case).

HPT1 is also characterized by a similar trend. In summary, it can be said that in the initial phase, when a tank has not yet undergone a filling phase, the differences in both temperatures are hardly visible. The filling phases can instead be identified by the 5 upward peaks of the gas temperature, followed by an increase in wall temperature. The post-filling pause phases are visible from the downward elbows of the wall temperature, more or less evident depending on the duration of the pause. Finally, the emptying phases are characterized by opposite temperature behaviour: that of the gas decreases, while that of the walls increases.

2.6.3 Low Pressure Tanks results

Figure 2.14 shows, from top to bottom, the graphs of mass flow rate, SOC, pressure and temperatures relative to the LPT.

As previously explained, the LPT refuels, whenever its SOC is less than 100%, with a mass flow rate equal to that of HG production (13.89 g/s). Simultaneously, it empties when required by the HPT cascade system (-60 g/s). This can also be observed by viewing together the mass flow rate and SOC graphs: when the latter equals 100%, the LPT is not filled, but only emptied when required. Instead, in the case where the SOC is below 100% and there is a request from the HPTs, the LPT empties by the difference between the compressed flow rate and that produced by the HG (close to -46 g/s). Finally, in moments when there is no hydrogen demand downstream, the LPT fills, as visible from the positive peaks. In the final phase, the LPT fills, as both the VTs and HPTs have already reached an SOC of 100%.

The pressure presents a trend analogous to that of the SOC, as previously seen by the other tanks. The initial value starts from the nominal pressure value, 3.5 MPa, equal to the hydrogen production pressure by the HG.

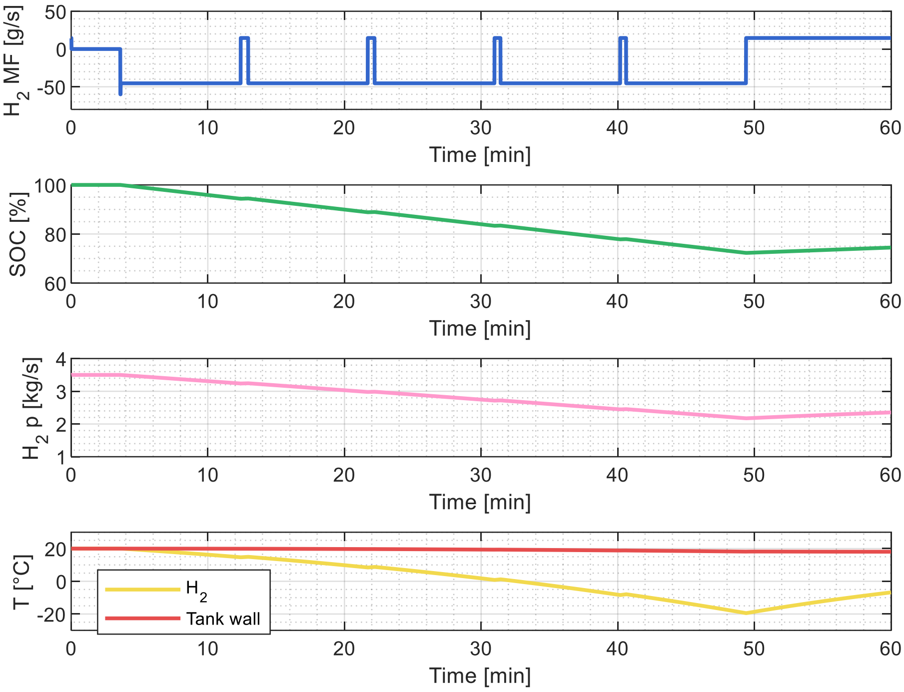

Figure 2.14 - Mass Flow, SOC, pressure and temperature of the LPT (base case).

Regarding temperatures, since the LPT is mainly characterized by emptying phases, the gas temperature decreases from ambient temperature down to a minimum of -19.43°C, then increases in the final filling phase with hydrogen arriving from the HG at 55°C. The wall temperature instead remains almost constant, with a slight decrease visible at the end. This phenomenon is primarily due to the significant larger volume of the LPT tank (150 m^3) compared to the HPTs (1.25-1.75 m^3) and VT (0.27 m^3), which provides substantial thermal mass and inertia. Additionally, the Type I steel construction (thermal conductivity of 50 W/mK) facilitates continuous heat exchange with the ambient environment, maintaining wall temperature close to ambient conditions despite gas temperature fluctuations.

2.6.4 Compressor and Pre-Cooling results

The compressor, as reported in Section 2.3, is characterized by 3 stages. Figure 2.15 shows the compression ratio for all stages.

As visible, this parameter has the same trend and value in all stages. In detail, the compression ratio is unitary during the pause phases, in which a compression pressure equal to that of the LPT and an indicative flow rate of 0.1 g/s have been set. Subsequently, during the compression phases, the compression pressure is that of the HPT being refuelled: in this phase, instead, the compression ratio increases slightly with time due to the decrease in LPT pressure of the inlet flow. The first compression phase begins, in particular, when HPT3 can no longer fill the VT: HPT2 therefore begins to empty, while HPT3 starts its first filling phase with compressed hydrogen at 35 MPa. The 5 compression phases reported are therefore related to the hydrogen demand by the cascade system, according to the established priority logic among the 3 HPTs. As visible, in fact, the compression ratio also increases slightly in each phase, depending on the pressure required by the cascade system. The compression ratio values are between 2.2 and 2.8, values lower than the average ones reported in Section 2.3, due to an inlet pressure higher than the minimum.

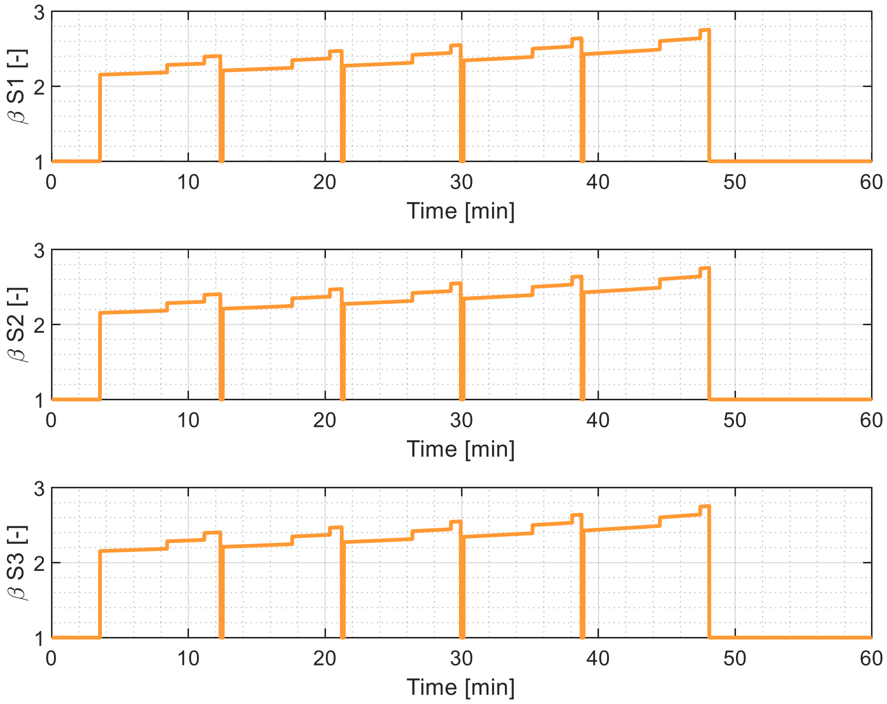

Figure 2.15 - Compression Ratio for each stage of the compressor.

Figure 2.16 shows the pressure trend in each stage. The initial value in each stage is 3.5 MPa, the starting value of the LPT, 100% full. In the first stage, it can be observed how the pressure decreases with time, as it is influenced by the LPT inlet pressure, which is also decreasing during all emptying phases. The slight final increase is instead due to the LPT pressure increase, under the filling phase, calculated with the minimum compression flow rate. The pressure values during the compression phases in this stage are between 7.9 MPa and 6 MPa.

Also, in the second stage the pressure shows a decrease with time, but much more contained than the previous one, with values between 19.5 MPa and 16 MPa. The last stage instead sees compression up to the pressures required by the cascade system, equal to 35 MPa, 40 MPa and 45 MPa.

As previously seen for the compression ratio, the pressure in each stage and in each of the compression phases also increases, depending on the pressure of the HPT in the filling phase.

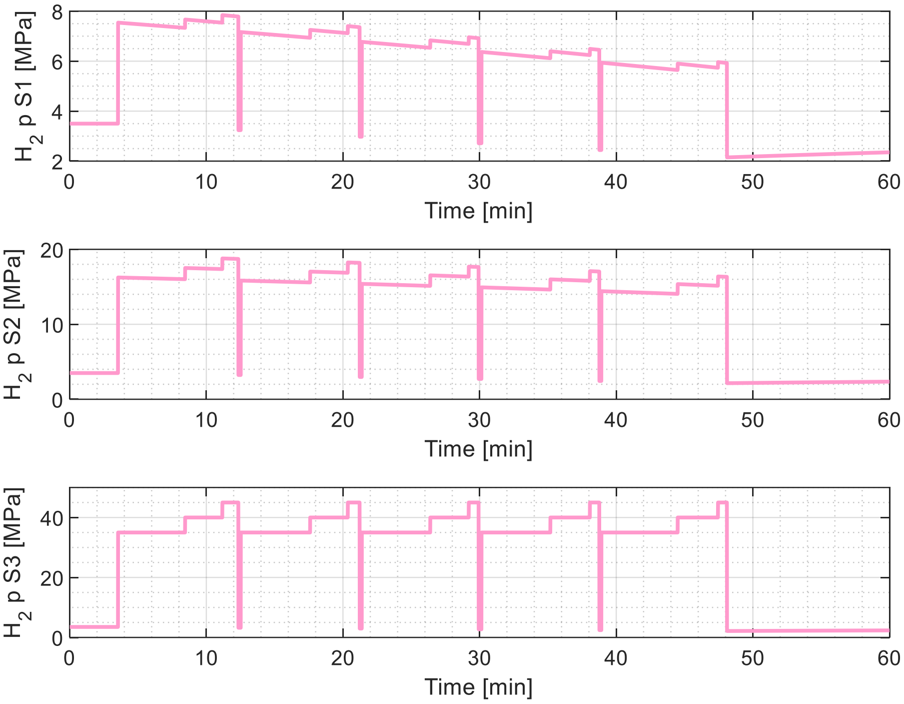

Figure 2.16 - Pressure for each stage of the compressor.

Regarding the two efficiencies, volumetric and isentropic, these are reported in Figures 2.17 and 2.18, respectively. Both efficiencies present equal values over time among the different stages.

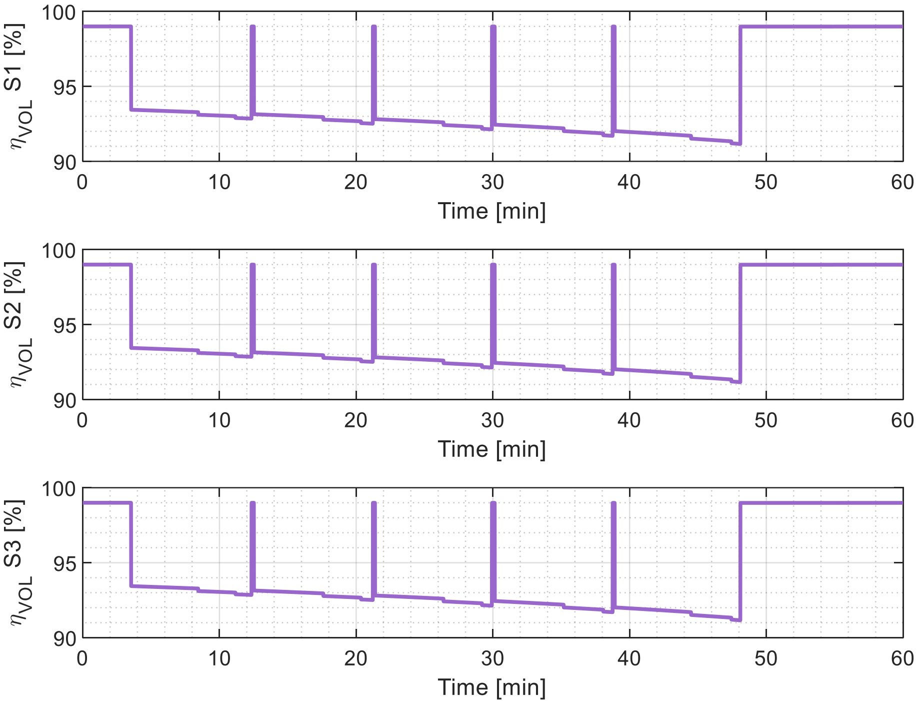

Figure 2.17 - Volumetric efficiency for each stage of the compressor.

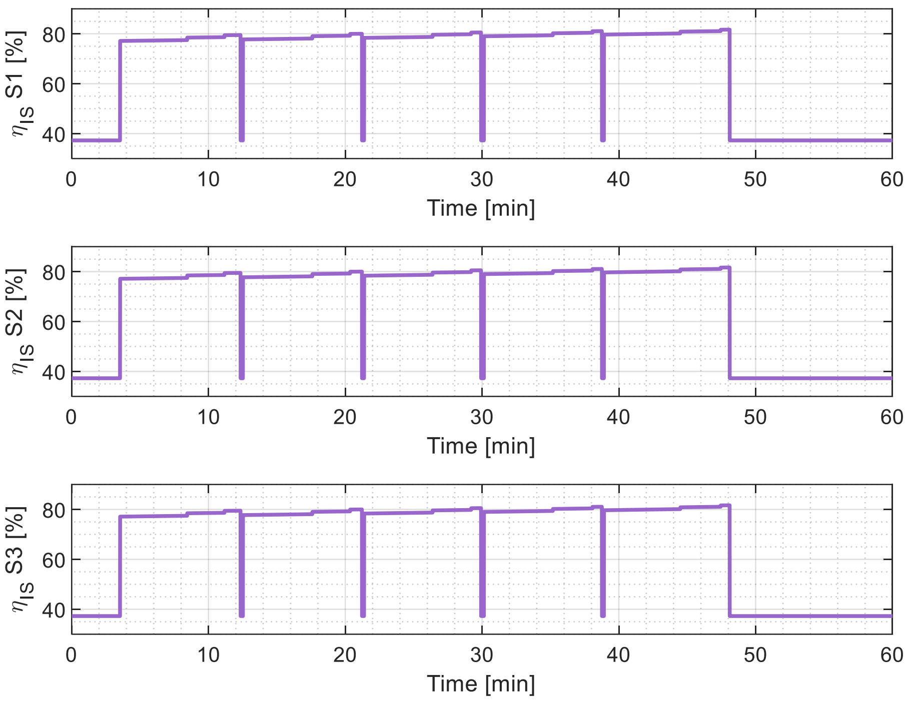

Figure 2.18 - Isentropic Efficiency for each stage of the compressor.

The volumetric efficiency is between approximately 91% and 93.5%, while the isentropic efficiency is lower and between 75.5% and 82%.. The two efficiencies, as visible in the figures, have opposite trends: while the volumetric efficiency decreases over time, the isentropic efficiency increases. This behaviour is easily understandable from the formulas of the two efficiencies, reported in Section 2.3. In fact, the isentropic efficiency is a function of the compression ratio alone (which increases over time), and the 2 positive terms out of 3 prevail over the single negative term. The volumetric efficiency is instead a function of both the compression ratio and other parameters, but all terms, beyond the initial unit constant, are negative.

Finally, Figure 2.19 shows the overall power of the HC (top) and PC (bottom). As previously reported, the maximum power of the HC is 450 kW. During pause phases the power is zero, as expected, since the compression pressure has been set equal to the inlet pressure. The power trend follows that already analysed previously for the other characteristic parameters of the HC: there are 5 compression phases, during which the power increases depending on the HPT being filled, while the power increases overall over time due to the decrease in inlet pressure (with the compressed mass flow rate being constant).

Regarding the PC, instead, this is mainly influenced by the hydrogen mass flow rate cooled and sent to the VTs, and by the inlet flow temperatures (while the outlet temperature is constant and fixed at -10°C). Also in this case, during pause phases the power is zero. During refuelings, instead, the cooling power decreases, as the inlet flow temperature decreases from HPT3 to HPT1. Between one refuelling and another, instead, the power increases as the initial temperature of the processed gas is higher compared to the initial temperature of the previous VT refuelling, since in the meantime each tank of the cascade system has been refuelled.

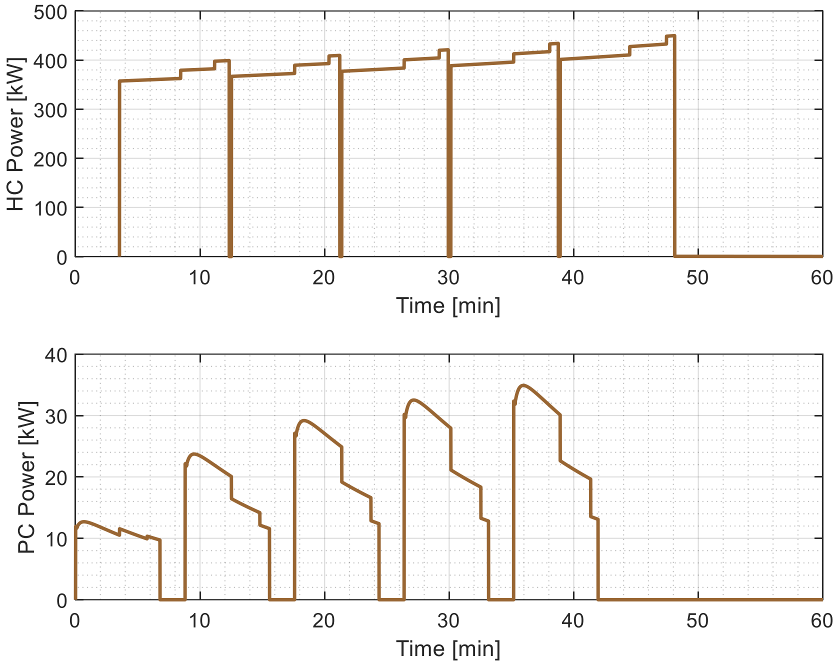

Figure 2.19 - Power for Compressor and Pre-Cooling.

2.7 Parametric analysis results

This section reports the results of a parametric analysis, varying one or more parameters, with the objective of identifying the maximum number of full refuelings that the HRS considered in this study is theoretically capable of guaranteeing. Some of the input parameter values presented in Table 2.7 were varied (less the initial SOCs) to find a number of refuelings greater than 5, initially hypothesized.

The first parameters to be varied were the APRR (between 4.5 MPa/min and 9.5 MPa/min) and the compressed hydrogen mass flow rate (between 60 g/s and 120 g/s). The selection of these two parameters is partly dictated by the system logic. To increase the number of refuelings, the APRR is adjusted, which increases the hydrogen flow rate required from the storage system. However, to ensure that the cascade system maintains a sufficient SOC during each refueling, it is also necessary to increase the compression flow rate upstream of the cascade system itself. Through a parametric analysis varying the two aforementioned parameters, the minimum compression flow rate was determined to guarantee the required number of refuelings, initially set at 5, for each APRR considered. Subsequently, with the objective of increasing the number of refuelings, an analogous parametric analysis was performed for target values of 6, 7, and 8 refuelings. The results are presented in Figure 2.20. The points shown satisfy all imposed conditions: temperatures and pressures below the upper limit or above the lower limit (particularly for LPT pressure), target number of refuelings, and cascade system SOC equal to 100% at the end of the hour.

As can be observed, with increasing number of refuelings, the curves shift toward higher compressed hydrogen flow rates (rightward), while the number of points on the curves decreases. Indeed, in the case of 7 refuelings, an APRR of 4.5 MPa/min never satisfies the target number of refuelings within the hour, whereas a value of 9.5 MPa/min consistently exceeds the temperature limit in HPT3. For 8 refuelings, both an APRR of 4.5 MPa/min and 5.5 MPa/min fail to satisfy the number of refuelings, while again at 9.5 MPa/min the temperature limit in HPT3 is exceeded and the LPT pressure drops below the minimum allowable value (1.5 MPa). The figure also indicates the unsatisfied constraint for lower flow rates, depending on the number of refuelings. For the case of 5 refuelings, the only unsatisfied constraint at lower flow rates is the target number of refuelings, while for the cases with 6, 7, and 8 refuelings, the HPT3 temperature constraint is also violated. Furthermore, for 8 refuelings, the minimum LPT pressure is not satisfied either.

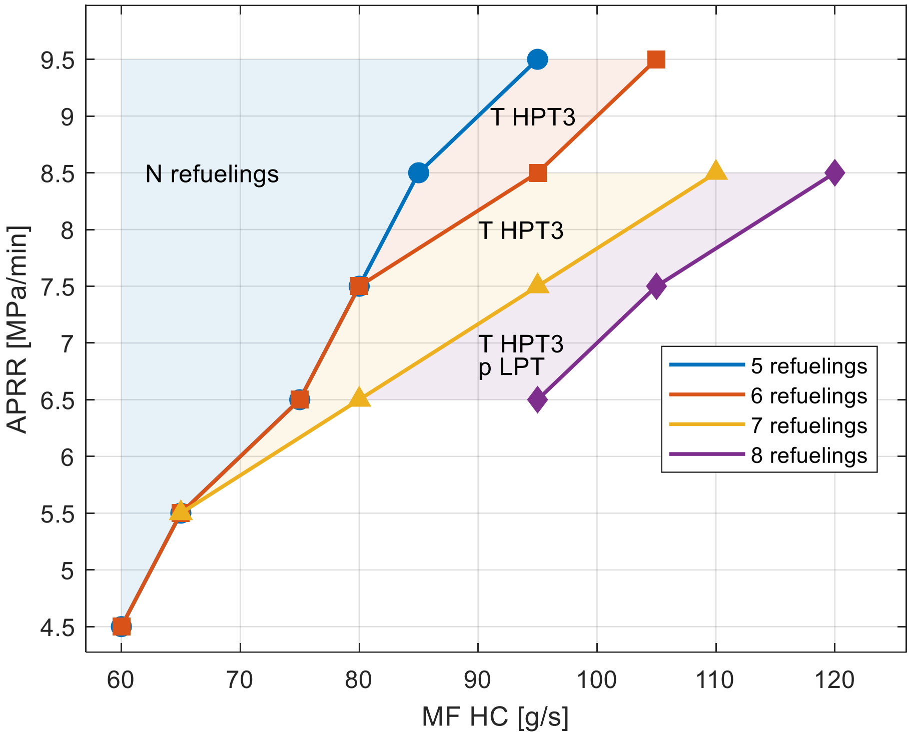

Figure 2.20 - Parametric analysis by varying APRR, mass flow HC and number of refuelings.

To address the temperature issue, the same parametric analysis was performed with a cascade system volume increased by 30% compared to the initial value. The results are presented in Figure 2.21. As can be observed, compared to the previous case, some of the obtained values are now shifted leftward. This is due to the fact that by increasing the cascade system volume, which is characterized by an initial SOC of 100%, a lower compression flow rate is required thanks to the greater initial hydrogen quantity. The points corresponding to unsatisfied refueling requirements are the same for the cases of 7 and 8 refuelings (4.5 MPa/min and 5.5 MPa/min), and are therefore not present. Conversely, the points characterized by an APRR of 9.5 MPa/min, which were absent in the previous case, now satisfy the temperature and pressure constraints. For lower flow rates, the most frequently unsatisfied constraint is the number of refuelings, particularly for 5, 6, and 7 refuelings. Furthermore, for 7 and 8 refuelings, the HPT3 temperature constraint is not satisfied at high APRR values. Finally, in the case of 8 refuelings and lower flow rates, the minimum LPT pressure is never satisfied.

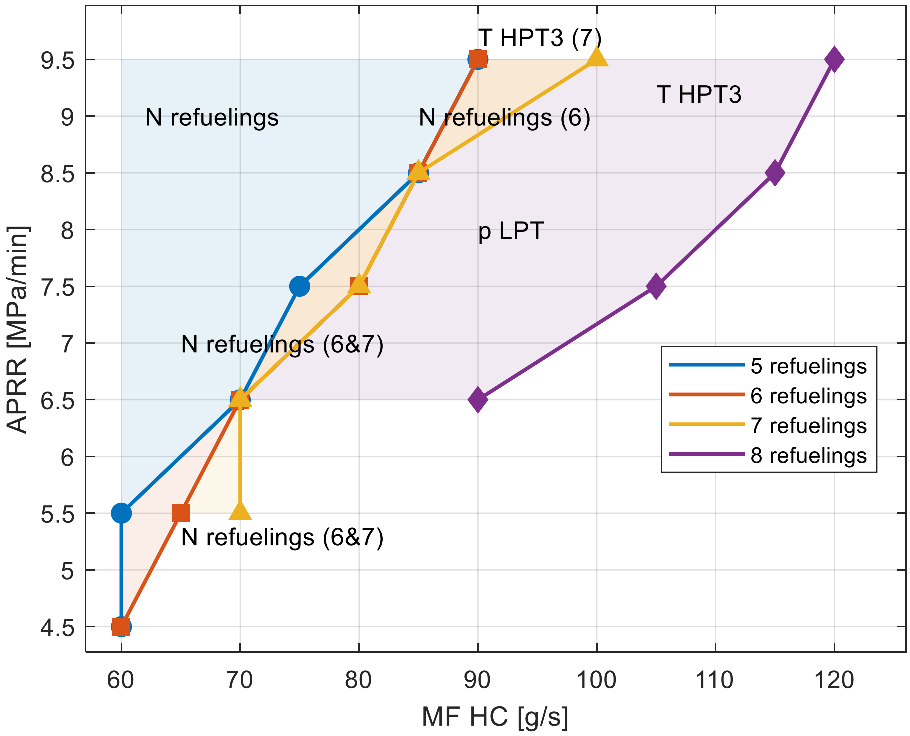

Figure 2.21 - Parametric analysis by varying APRR, mass flow HC, number of refuelings and cascade system volume by 30%.

To ensure compliance with the temperature constraint even at high APRR values, a final parametric analysis was performed, this time considering a 45% increase in the cascade system volume compared to the initial value. The results are presented in Figure 2.22. As previously observed, the minimum compressed flow rate values obtained are partially shifted leftward. Considering lower flow rates, the least satisfied parameter remains the target number of refuelings, while the temperature values are now always satisfied. Another parameter that is not satisfied at lower flow rates is the LPT pressure in the case of 8 refuelings. In this regard, the LPT volume could be increased; however, since the hydrogen production flow rate and consequently the hydrogen stored in the LPT will be optimized subsequently, it was decided to maintain a constant tank volume at this stage. A final consideration concerns the minimum flow rates obtained for an APRR of 4.5 MPa/min (6 refuelings) and 5.5 MPa/min (7 refuelings). These points exhibit a minimum flow rate higher than that obtained for the immediately subsequent APRR: for 6 refuelings, a flow rate of 65 g/s is required at 4.5 MPa/min compared to 60 g/s at 5.5 MPa/min, while for 7 refuelings, a flow rate of 75 g/s was found at 5.5 MPa/min versus 70 g/s at 6.5 MPa/min. This aspect is primarily related to the final refilling of the cascade system (rather than to the refueling of the VTs), which must be completed within the hour: to ensure this is possible, it was necessary to increase the compression flow rate.

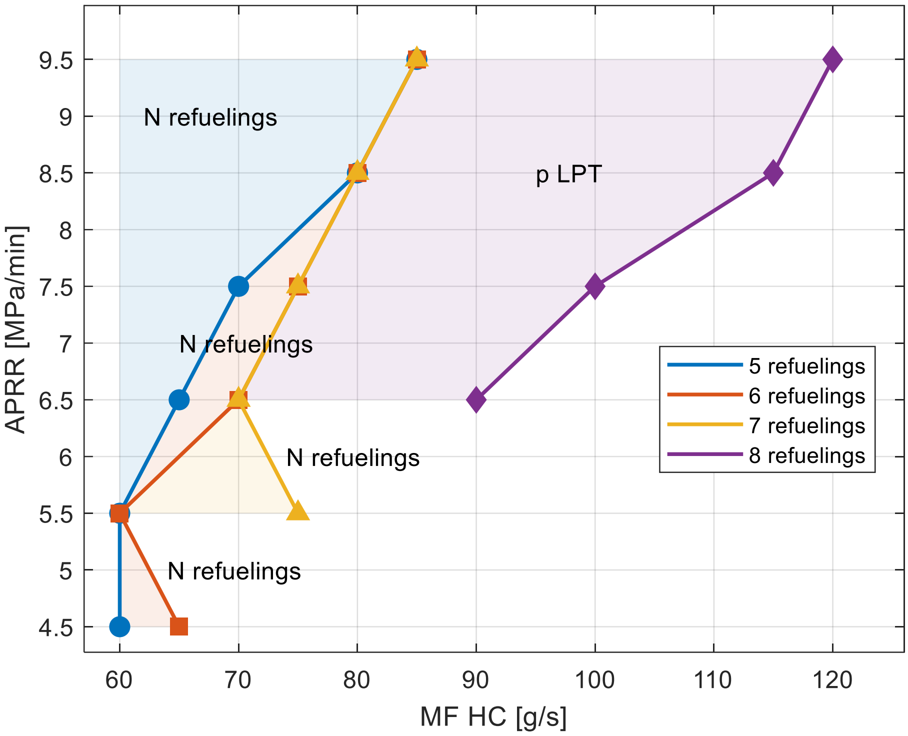

Figure 2.22 - Parametric analysis by varying APRR, mass flow HC, number of refuelings and cascade system volume by 45%.

In summary, the parametric analysis varying one or more parameters showed satisfactory results, regarding the number of refuelings guaranteed, for either 6, 7 or 8 refuelings in one hour. Regarding the HRS components, major problems occurred with HPT3: these were remedied by increasing the volume of the cascade system, in cases where HPT3 temperature exceeded the limit of 85°C. The LPT also contributed to the failure of some simulations, but only for those characterized by a high number of refuelings and a high compressed flow rate.

Of the initial inputs, it was decided not to vary all parameters. As said before, the LPT volume was kept constant in all simulations during this phase, as it does not affect the achievement of the target number of refuelings. The hydrogen production mass flow rate was also kept constant: in fact, it was calculated to satisfy the required refuelings and to refuel the LPT throughout the day. Furthermore, the solution with a production of approximately 15 g/s of hydrogen is already energy-intensive, and not suitable in the case where vehicles are to be refueled with green hydrogen, as the electrolyzer would run most of the day to refuel the LPT. This aspect will therefore be improved subsequently. Also, the precooling temperature was left constant and equal to -10°C: this temperature, in fact, influences only the gas temperature inside the VTs, already under control with the selected ambient temperature. Like the PC temperature, the ambient temperature was left constant, considering this temperature as average throughout the year. This choice can be acceptable for the theoretical functioning of HRS operation and will be further investigated subsequently. Finally, additional tests were not performed, as the results obtained for the satisfactory tests were close to the temperature or pressure limits or would almost certainly have increased consumption.

Regarding the results of the satisfactory tests just analysed, these are represented in the subsequent figures by means of heatmaps. The results, particularly the refueling characteristics, pressures, temperatures, SOC and energy consumption, are grouped in different figures, while each test from the previous parametric analysis is highlighted on the x-axis and by vertical lines of a different colour from those of the results.

Figure 2.23 presents the results of the number of refuelings achieved, the time per refueling, and the maximum hydrogen flow rate delivered by the dispenser.

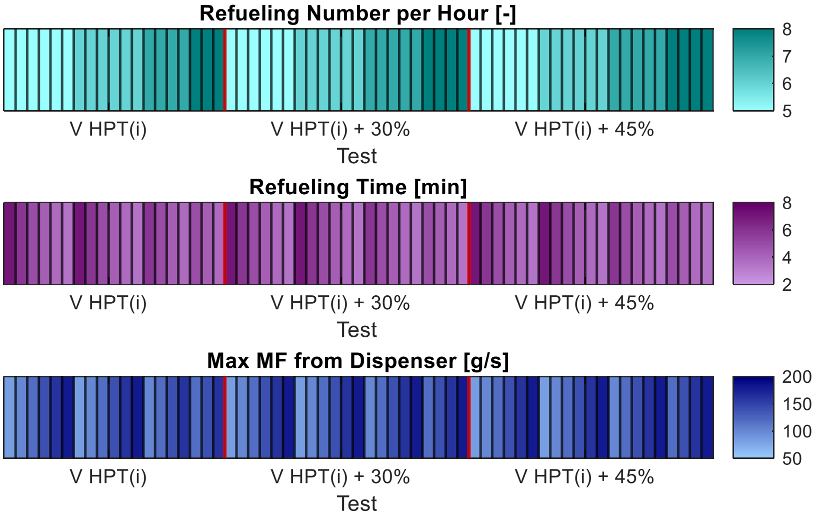

Figure 2.23 - Satisfactory results of parametric analysis – Refuelings.

The number of refuelings is the same as the target. Regarding the refueling time, this is strictly related to the maximum hydrogen flow rate delivered by the dispenser: indeed, it can be observed in the figure that the shorter the refueling time, the higher the hydrogen flow rate, which is influenced by the APRR value. The shortest times were obtained, for obvious reasons, with higher APRR values and range overall between 3.45 min (APRR=9.5 MPa/min) and 7.15 min (APRR=4.5 MPa/min). These values correspond to the highest delivered flow rate, approximately 180.62 g/s, and the lowest, 83.26 g/s.

Figure 2.24 instead reports the maximum pressure value for the VT and cascade system, while for the LPT the minimum pressure is reported. Indeed, since the latter tank is mainly characterized by emptying, its maximum pressure is always equal to the nominal value. Furthermore, since the minimum compressor pressure is 1.5 MPa, the minimum pressure of the LPT was also set to the same value, in order to evaluate the net quantity of hydrogen that can be utilized. In the figure, the upper limit of each legend indicates the maximum pressure for each tank, according to the SAE J2601-5 limit.

As can be observed, the tank characterized by a pressure close to the limit value is HPT3, followed by HPT2, VT and HPT1. As previously highlighted, HPT3 is indeed the most stressed tank during refueling, according to the established priority logic.

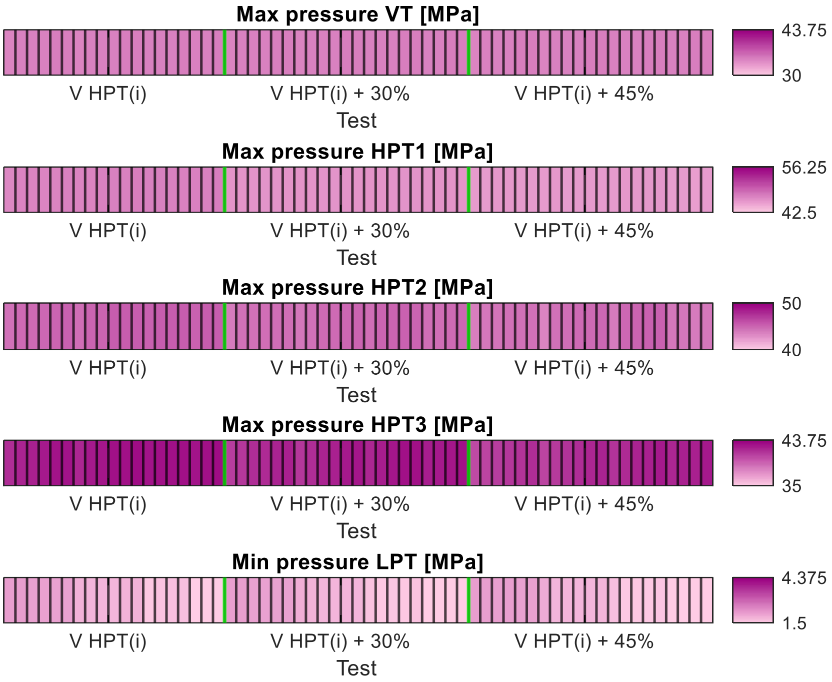

Figure 2.24 - Satisfactory results of parametric analysis – Pressures.

For the LPT, conversely, the values found tend more toward the lower limit. Among the different tests, however, there is no evident change between the results found. This aspect can also be observed in the range between the maximum and minimum values in each tank:

- In the VT, the values found range from a minimum of 34.79 MPa (test with APRR equal to 4.5 MPa/min) to a maximum of 35.35 MPa (test with APRR of 9.5 MPa);
- In HPT1, the values range between 45.70 MPa and 47.68 MPa;
- HPT2 is characterized by a minimum of 43.51 MPa and a maximum of 45.39 MPa;
- HPT3 has a minimum equal to 40.48 MPa and a maximum of 43.13 MPa;
- Finally, the LPT ranges from a minimum of 1.50 MPa to a maximum of 2.21 MPa.

Figure 2.25 shows the temperature results, which exhibit a similar trend to those of pressure. The tank characterized by values close to the limit of 85°C is HPT3, now followed by HPT2 and the VT. Lower temperatures are found in HPT1, which is last in the cascade system management logic, and the LPT, which predominantly undergoes emptying phases that do not increase temperature. As before, the results do not vary visibly from one test to another, except for the LPT, which shows a more or less marked decrease in results. Specifically, the temperature values range between:

- A minimum of 51.05°C and a maximum of 55.56°C for the VT;
- A value of 23.67°C and a maximum of 36.42°C for HPT1;
- A minimum of 44.58°C and a maximum of 57.53°C for HPT2;
- A value of 63.99°C and a maximum of 84.97°C for HPT3;
- A minimum of -51.53°C and a maximum of 20°C for the LPT.

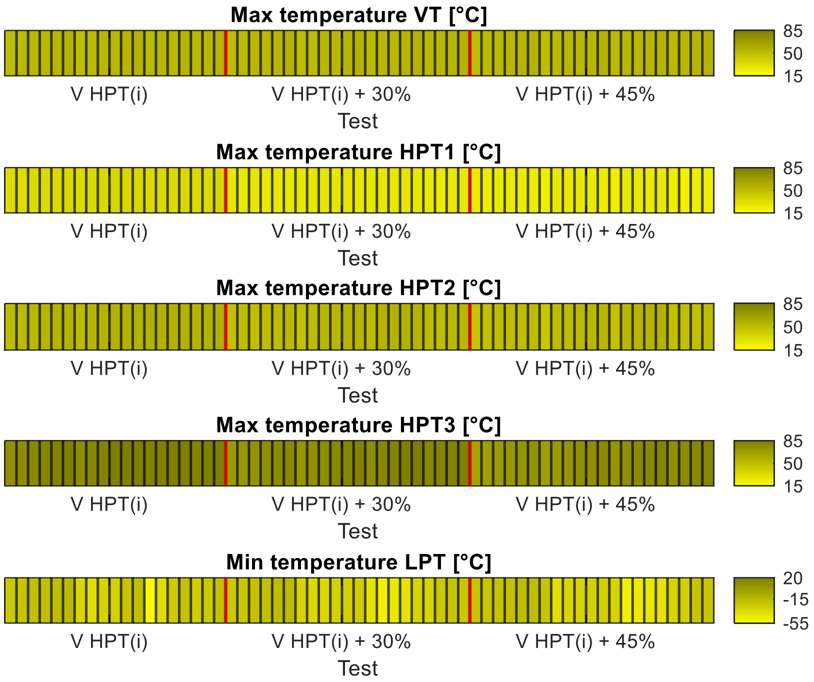

Figure 2.25 - Satisfactory results of parametric analysis – Temperatures.

Regarding the SOC values, the minimum values are reported in this case, as the maximum values at 100% are already guaranteed by the simulations considered positive during the parametric analysis, with the exception of the LPT, for which refueling over multiple hours is envisaged. As can be observed in Figure 2.26, the tank that is emptied the most is HPT3, as established by the logic.

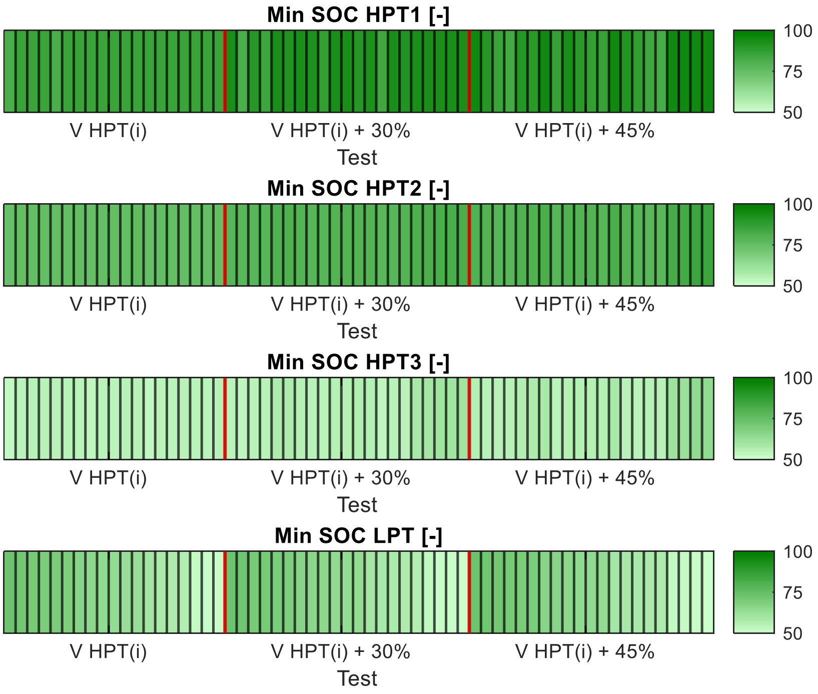

Figure 2.26 - Satisfactory results of parametric analysis – SOC.

Consequently, HPT2 is less depleted, while HPT1 has values close to 100%. The test values do not differ for the cascade system, whereas for the LPT the values vary slightly between the different tests. The minimum SOC values range:

- Between 81.45% and 95.79% for HPT1;
- Between 74.54% and 84.63% for HPT2;
- Between 52.95% and 64.72% for HPT3;
- Between 50.55% and 72.79% for the LPT.

Figure 2.27 finally reports the results of the maximum power of the HC and PC, their energy consumption, and the respective sums. The highest power for the compressor was found for higher compressed flow rates (120 g/s), while the highest value of PC power is due to the higher APRR value considered (9.5 MPa/min). The overall values vary more significantly both for power and consumption from one test to another, unlike the previous cases. However, higher power does not correspond to higher consumption. Specifically, the values range between:

- 412.16 kW (consumption of 286.75 kWh) and 995.6 kW (consumption of 470.06 kWh) for HC power;
- 281.59 kWh (power of 639.15 kW) and 477.39 kWh (power of 783.01 kW) for HC consumption;
- 27.8 kW (consumption of 10.2 kWh) and 82.18 kW (consumption of 21.92 kWh) for PC power;
- 10.2 kWh (power of 27.8 kW) and 21.97 kWh (power of 73.49 kW) for PC consumption.

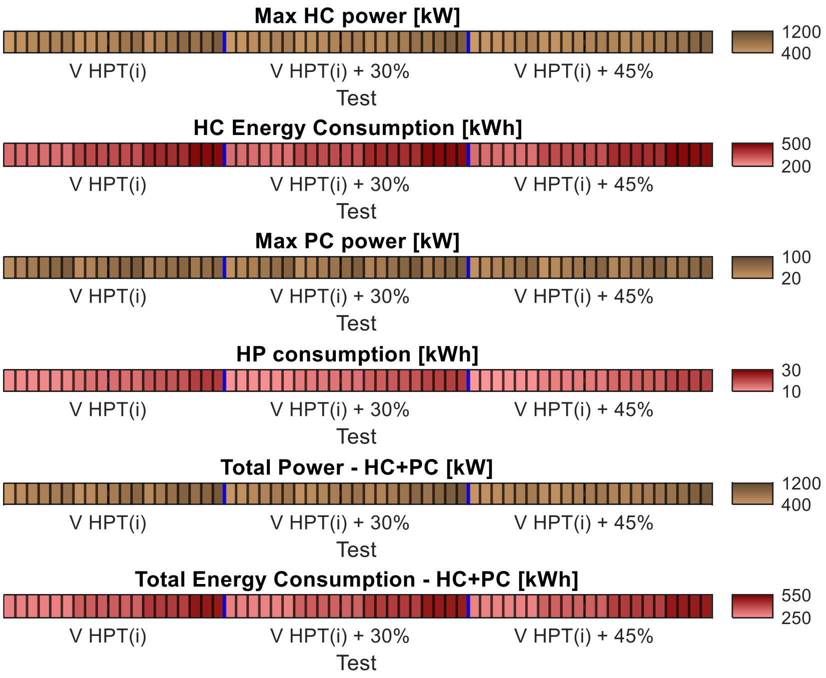

Figure 2.27 - Satisfactory results of parametric analysis – Consumptions.

As can be observed from the results, the only case in which power and consumption belong to the same simulation is the case of the minimum pre-cooling values.

Furthermore, the PC power is between 6.74%÷8.25% of the HC power, while at the consumption level the percentage decreases 3.62%÷4.6%.

The best and worst results, defined according to final energy consumption, are reported in Table 2.9 for 6, 7, and 8 refuelings. As previously highlighted, moreover, the case with 8 refuelings is also the one characterized by higher energy consumption, for a total of approximately 500 kWh consumed by the HC and PC. As the number of refuelings decreases, as shown in the table, energy consumption decreases to approximately 430 kWh in the case with 7 refuelings and 360 kWh with 6 refuelings. Since the consumption values are quite similar between the best and worst cases, these are identified based on the lower and higher power, respectively. Specifically, in the case with 6 refuelings, the power varies from a total of 463.6 kW to 814.2 kW, while with 7 refuelings the results range between 529.6 kW and 878.6 kW, a similar range than the previous one.

Table 2.9 - Best and worst results for 6, 7, and 8 refuelings.

Parameter		**6 REFUELS**		**7 REFUELS**		**8 REFUELS**	
		Best	**Worst**	**Best**	**Worst**	**Best**	**Worst**
APRR	[MPa/min]	4.5	9.5	5.5	8.5	6.5	9.5
MF HC	[g/s]	60	105	65	110	90	120
V HPT$_{1,2,3}$	[m^3]	+30%	+0%	+0%	+0%	+45%	+30%
Ref. Time	[min]	7.15	3.45	5.88	3.85	5	3.45
Max MF Disp.	[g/s]	83.26	180.6	101	160.3	119.5	180.6
Max p VT	[MPa]	34.79	35.35	34.96	35.3	35.1	35.35
Max p HTP1	[MPa]	46.21	47.68	47.46	47.61	45.71	46.25
Max p HTP2	[MPa]	44.08	45.39	45.31	45.34	44.17	44.90
Max p HTP3	[MPa]	41.42	43.11	42.88	43.06	42.00	42.98
Min p LPT	[MPa]	1.92	1.90	1.57	1.71	1.51	1.50
Max T VT	[°C]	51.05	55.56	52.28	54.91	53.30	55.56
Max T HTP1	[°C]	27.40	36.42	35.65	36.06	23.88	27.10
Max T HTP2	[°C]	48.51	57.53	56.98	57.19	49.03	54.07
Max T HTP3	[°C]	71.52	84.97	83.25	84.35	76.22	84.20
Min T LPT	[°C]	-30.59	-18.09	-51.53	-19.34	-30.04	-22.60
Min SOC HPT1	[%]	92.98	85.92	85.58	85.72	95.64	93.13
Min SOC HPT2	[%]	78.97	75.81	74.54	75.62	82.69	81.55
Min SOC HPT3	[%]	55.85	55.01	52.95	54.77	61.00	60.65
Min SOC LPT	[%]	66.96	62.97	59.83	57.01	52.49	50.55
Max HC Po.	[kW]	463.6	814.2	529.6	878.6	744.1	995.6
HC Cons.	[kWh]	348.7	344.2	416.6	409.1	474.6	470.1
Max PC Po.	[kW]	31.79	81.79	45.20	72.74	49.45	82.18
PC Cons.	[kWh]	13.75	15.78	18.54	18.80	20.29	21.92

Both worst cases obtained for 6 and 8 refuelings are characterized by the same initial inputs, namely 9.5 MPa, a compressed flow rate of 180.6 g/s, and cascade system volumes increased by 30% for 8 refuelings. The worst case for 7 refuelings is instead characterized by an APRR equal to 8.5 MPa/min and cascade system volumes equal to the initial values. Regarding the pressures, both maximum and minimum, these are similar for all tanks and cases. The temperatures remain relatively consistent across scenarios, with the notable exception of HPT3. For the best-case scenario with 6 refuelings, HPT3 reaches a minimum temperature of 71°C, whereas the worst-case scenarios and the best case with 7 refuelings exhibit significantly higher temperatures, approaching the operational limit of 85°C.

In conclusion, the HRS is capable of satisfying a maximum of 8 refuelings, respecting all pressure and temperature limits depending on the APRR, mass flow compressed and cascade system configuration, but with high consumption. If instead one wishes to increase the number of refuelings compared to the base case, characterized by 5 refuelings, an APRR of 4.5 MPa, a compressed flow rate of 60 g/s and HPTs minimum volumes, to perform at least one additional refueling it is necessary to increase consumption from approximately 299 kWh to 360 kWh, while the power should increase from approximately 481 kW to 495.4 kW. Finally, the cascade system volume should increase by 30%.

2.8 HRS realistic simulation

As highlighted in the previous paragraph, there are some aspects identified from the results that, in order to study the real operation of the HRS, can be improved. Among these are:

- The initial SOC of the VTs: in reality, it is preferable to refuel a vehicle at the end of its working day, and not when it has an almost empty tank. Much also depends on the vehicle's range and its tank capacity, but in both cases ongoing developments are leading to higher achievable values [109]. This means that, in reality, the VT's SOC will not be equal to the initially assumed 10%, but higher;
- The ambient temperature: this can realistically vary between -10°C and 40°C, creating different seasonal conditions. This temperature must therefore be set according to the Pre-Cooling temperature, to avoid high temperatures in the VTs and HPTs;
- The final temperature and pressure of HPT3: as seen from the results, being the most used tank in the HRS, its pressure and temperature values are often close to the SAE protocol limits. This is not desirable, especially in the case of refuelings during consecutive hours;
- The HG mass flow rate produced: so far, a flow rate capable of refuelling the LPT throughout the entire day has been considered. However, considering the production and use of green hydrogen produced through renewables, continuous operation over time is not realistic, unless there is a large quantity of electrical energy stored.

In the following, the points reported above will be addressed in detail, with the aim of outlining more realistic characteristics of the operation of the HRS studied so far.

2.8.1 H_2 bus fleet demand and definition of the new SOC for VTs

To determine the SOC at which the VTs (Vehicle Tanks) arrive for refueling, an urban bus line currently operated with diesel vehicles in Cagliari (Sardinia) was considered, with the aim of assessing its potential conversion to FCEVs powered by green hydrogen. Table 2.10 reports the main characteristics of the bus line and the selected hydrogen-powered bus, while Table 2.11 presents the hydrogen consumption and daily demand of the bus fleet.

As shown in Table 2.10, the selected bus has a driving range of 500 km, equipped with 6 tanks capable of storing a total of 35 kg of hydrogen at 35 MPa. Based on the data of the route considered, characterized by a round trip of 24.3 km covered at an average speed of 13.3 km/h, the hydrogen consumption of the bus is 1.7 kg per complete round trip and 0.931 kg per operating hour (since a round trip takes approximately 1 hour and 50 minutes). Regarding the CO_2 emissions of the local bus company, these amount to 1.072 kg CO_2/km [110]: consequently, considering the total distance of the line over the year, the emissions avoided by replacing the 21 diesel buses with hydrogen vehicles correspond to 36.84 kt CO_2/year.

Table 2.10 - Bus line and hydrogen bus characteristics [101].

Parameter		Value	Parameter		Value
Line roundtrip (RT)	[km]	24.3	Bus autonomy	[km]	500
Commercial velocity	[km/h]	13.3	Bus tank pressure	[MPa]	35
Daily line distance	[km]	3 828	Bus total capacity	[kg]	35
R time	[s]	109.6	Bus N° of tanks		6
Max buses in service		21	H2 consumption	[kg/RT]	1.7
			H2 consumption	[kg/h]	0.931

Table 2.11 reports hydrogen consumption and demand on an hourly basis. The second column shows the maximum number of buses in operation, which increases during peak hours. The table also includes the hourly hydrogen consumption throughout the day (calculated by multiplying the number of operating buses by the hourly consumption reported in Table 2.10) and the total distance travelled by the fleet (obtained by multiplying the average speed by the number of operating buses). The resulting values amount to approximately 275 kg/day of hydrogen consumption for the fleet, corresponding to just over 100 tons per year, and 3 923.5 km/day of total distance travelled. The latter slightly differs from the value initially provided for the bus line, likely because, in real operating conditions, buses do not run continuously throughout every hour of the day (especially toward the end of service), as instead assumed in this study. Finally, the last column shows the hydrogen demand of the different buses, expressed as the total demand per hour. As expected, the cumulative daily demand equals the total daily consumption.

In particular, the hydrogen demand is distributed over 6 different hours, depending on the end of the work shift times of the buses:

- 14:00: 3 buses require 8.38 kg of H_2;
- 15:00: 6 buses require 7.45 kg of H_2;
- 21:00 and 22:00: 2 buses require 13.96 kg of H_2, while another 2 require 14.9 kg;
- 23:00: 3 buses require 13.96 kg of H_2;
- 00:00**:** 1 bus requires 14.9 kg, while the remaining 5 require 6.52 kg of H_2.

As can be observed, refueling is required for 26 buses in total, rather than 21. This is because 5 buses refuel twice during the day, allowing the refueling operations to be better distributed and preventing an excessive demand peak at the end of the day. Moreover, as shown in the previous results, after only one hour of refueling the pressure and temperature inside HPT3 already reach values close to their respective limits. For this reason, the refueling operations initially scheduled at 23 and midnight (highlighted in red in Table 2.11, as they were removed) were rescheduled to 5 and 6 in the morning, respectively.

Table 2.11 - Bus fleet hydrogen consumption and demand.

	Buses in service [-]	**Daily H_2 consumption [kg H_2/h]**	**Daily buses distance [km/h]**	**Daily H_2 refueling [kg H_2/h]**
5 – 6	6	5.586	79.8	41.88
6 – 7	9	8.379	119.7	47.5
7 – 8	21	19.55	279.3	
8 – 9	21	19.55	279.3	
9 – 10	21	19.55	279.3	
10 – 11	21	19.55	279.3	
11 – 12	21	19.55	279.3	
12 – 13	21	19.55	279.3	
13 – 14	21	19.55	279.3	
14 – 15	18	16.76	239.4	25.14
15 – 16	12	11.17	159.6	44.69
16 – 17	12	11.17	159.6	
17 – 18	17	15.83	226.1	
18 – 19	17	15.83	226.1	
19 – 20	17	15.83	226.1	
20 – 21	16	14.90	212.8	
21 – 22	13	12.10	172.9	57.72
22 – 23	6	5.586	79.8	57.72
23 – 00	5	4.655	66.5	41.88
00 – 01				47.5
Per day →		274.65	3 923.5	274.65

For the subsequent calculations, the most critical refueling block during the day was identified. This corresponds to the two consecutive refueling operations at 21 and 22, characterized by the highest total hydrogen demand and therefore by the most intense thermal activity inside the tanks, which could potentially cause the system to exceed its pressure and temperature limits. During these hours, as previously reported, 2 buses require approximately 14 kg of hydrogen each, while another 2 require around 15 kg. Consequently, the initial SOC of the VTs was set at 57%, corresponding to the lowest tank level reached by the vehicles throughout the day. If the resulting maximum pressure and temperature values are satisfactory for this worst-case scenario, it can reasonably be expected that the other refueling operations will also comply with the safety requirements.

2.8.2 Definition of seasonal Pre-Cooling temperature and analysis of cascade system temperature trends throughout the day

With regard to the analysis of gas temperature during the subsequent refueling hours, the rescheduling of the 2 refueling to the early morning may not be sufficient to prevent the HPT3 from reaching its operational limits. In fact, this tank already exhibits near-limit temperature values after the first hour of refueling, as shown previously. To address this issue, a hydrogen Pre-Cooling system was introduced upstream of the cascade storage system, in order to prevent excessive gas heating after two consecutive hours of refueling.

It should also be noted that the attainment of high temperatures inside the storage tanks depends on the ambient temperature. To evaluate the temperature evolution within the tanks, four different ambient temperature conditions, representing the seasonal maximums, were considered: 10 °C for winter, 20 °C for autumn, 30 °C for spring, and 40 °C for summer. For each of these seasonal cases, the behaviour of the gas temperature was studied as a function of the hydrogen PC temperature, varied from –40 °C to 0 °C in 10 °C increments. This parametric analysis was performed with the aim of identifying, for each season, the optimal PC temperature capable of keeping the gas temperature within the SAE protocol limits and to ensure that the gas temperature returns to ambient conditions during the break between refueling blocks.

Dynamic simulations of the gas thermal evolution in the cascade system were performed for the refueling block occurring at hours 21-22, followed by a 6-hour idle period. This operational scenario was identified as the most critical case, featuring the highest hydrogen mass flow demand. By analysing this limiting condition, compliance with thermofluids dynamic constraints, including gas pressure and temperature limits and thermal recovery to ambient temperature during idle periods, can be assessed under worst-case conditions. Given that subsequent refueling cycles involve lower hydrogen consumption rates, it is postulated that thermal loads will be proportionally reduced, thereby ensuring compliance with operational limits.

The gas temperature evolution results were obtained, as mentioned, from dynamic simulations performed at varying system temperatures (ambient and pre-cooling) during the first refueling block (21, 22). The inputs for the first hour simulation are summarized in Table 2.12.

Table 2.12 - Input for HRS model: real Simulation at first hour of refueling.

Parameter		Value	Parameter		Value
APRR	[MPa/min]	4.5	N. Ref Target	[-]	4
T Amb	[°C]	10:10:40	T Pre-Cooling	[°C]	-40:10:0
SOC VT	[%]	57	V VT	[m^3]	0.27
SOC HTP$_{1,2,3}$	[%]	100	V HPT$_{1,2,3}$	[m^3]	1.6/1.95/2.25
SOC LPT	[%]	100	V LPT	[m^3]	150
MF HC	[g/s]	60	MF HG	[g/s]	14.59

These parameters correspond to the optimal configuration identified in the previous study, with reference to the HRS capacity for 6 refuelings (Table 2.9). Since the most critical refueling hours in the real investigation involve 4 refuelings, the number of target refueling was adjusted accordingly. The initial SOC of the VT was increased to 57%, while the hydrogen production rate will be optimized in subsequent analyses, which include the integration of the HRS studied within a renewable microgrid system. The inputs for the second hour of refueling are the same as reported in Table 2.9, except for the initial temperatures of the cascade system (equal to the final temperatures obtained at the end of the first hour for each tank), the temperature and the SOC of the LPT.

The results of the final temperature related to the first refueling block are reported, for each season, in the following figures for the HPT2 and HPT3 tanks only. The choice to show only the final temperature obtained after the dynamic simulation as the precooling temperature varies is due to the complexity of representing each dynamic temperature curve per each precooling temperature, since the trend is similar to the one shown in Figure 2.13. The HPT1 tank is discharged only occasionally during summer; however, its minimum SOC remains close to the nominal value (98.84%). For this reason, its internal temperature remains essentially constant regardless of the external ambient conditions. Nevertheless, HPT1 was not excluded from the system, as it could become useful in scenarios involving a higher number of refueling events than initially assumed, or refueling operations with greater hydrogen demand.

Figure 2.28 illustrates the first gas temperatures after the first hour (22) and the second hour (23) of refueling for HPT2 (left) and HPT3 (right), as the precooling temperature varies, during the winter season. For both tanks, the initial temperature in the dynamic simulation (at 21) was set to 10 °C, which was kept constant throughout the entire day. As expected, based on previous results, the temperature in HPT3 is higher than in HPT2. After the first hour of refueling (at 22), the gas temperature in HPT2 ranges between 14 °C and 20.5 °C, while after the second hour of refueling (at 23) it reaches values between 16.74 °C and 26.56 °C. The highest values were obtained for the highest precooling temperature, 0 °C.

In HPT3, the gas temperature ranges from 18.94 °C to 31.67 °C at the end of the first refueling hour, and from 24.15 °C to 44.69 °C at the end of the second, again showing a direct correlation with the PC temperature.

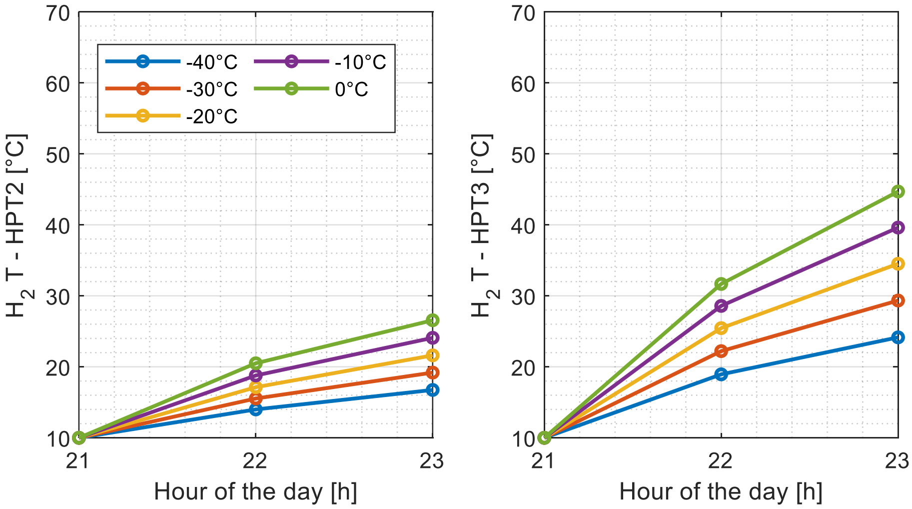

Figure 2.28 - Daily trend of hydrogen temperature: winter.

Figure 2.29 presents the final gas temperature results after the first 2 hours of refueling for the autumn case, characterized by a maximum ambient temperature of 20 °C. In this case as well, the trend is repeated: the gas temperature increases more in HPT3, with curves that appear shifted upward compared to the winter case. For

HPT2, the temperature rises from 23.05 °C to 30.27 °C during the first refueling hour, and from 25.12 °C to 36.2 °C during the second, with the lowest values corresponding to a PC temperature of –40 °C. In HPT3, the temperature increases from 25.91 °C to 38.29 °C during the first refueling hour and reaches values between 29.44 °C and 49.55 °C during the second, always considering the increase in PC temperature.

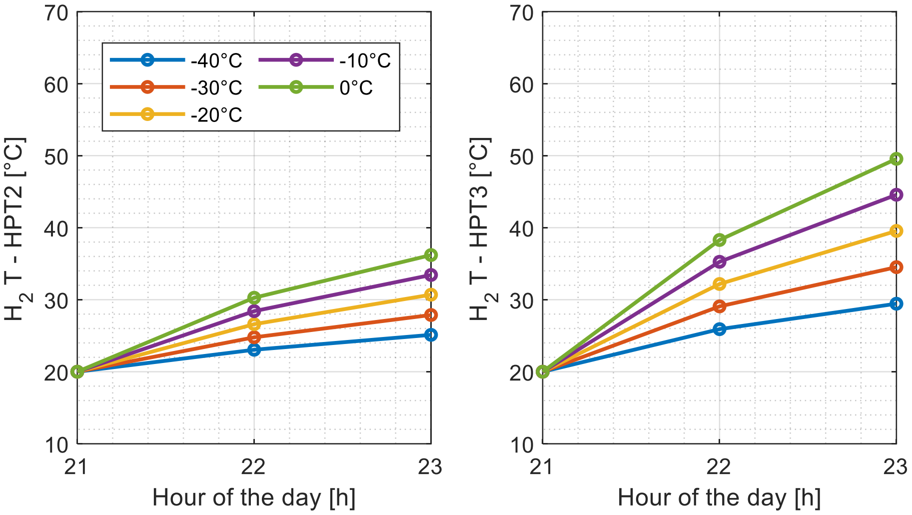

Figure 2.29 - Daily trend of hydrogen temperature: autumn.

Figure 2.30 presents the results for the spring season, characterized by an ambient temperature of 30 °C. Once again, the refueling exhibit similar trend to the previous one, with gas temperatures increasing as the PC temperature increases. At the end of the first hour of refueling, temperatures ranged between 31.79 °C and 39.4 °C for HPT2 and between 33.03 °C and 45.08 °C for HPT3. During the second refueling hour, the temperature rises from 33.03 °C to 45.2 °C in HPT2 and from 34.86 °C to 54.43 °C in HPT3.

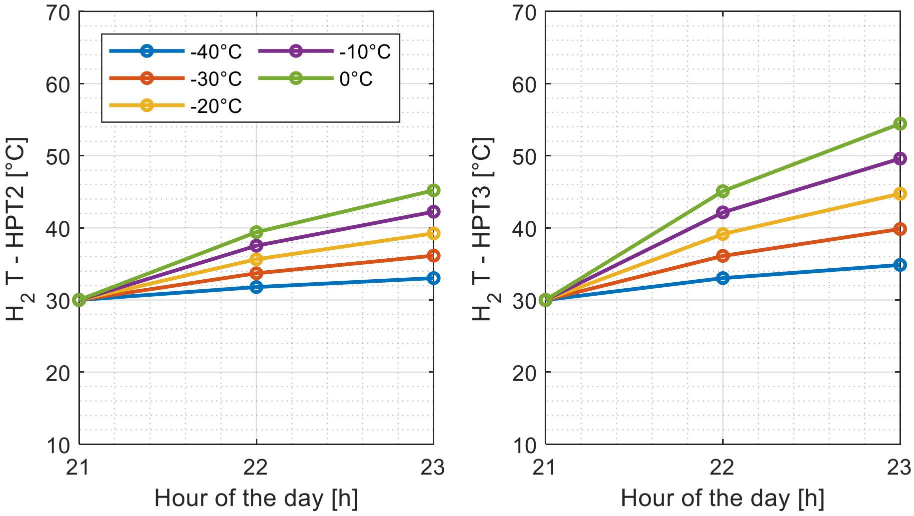

Figure 2.30 - Daily trend of hydrogen temperature: spring.

Figure 2.31 reports the results for the summer case, characterized by a maximum ambient temperature of 40 °C. As expected, this condition also shows similar results for the first and second refueling hours, with the curves appearing shifted upward compared to the previous case, but more compressed than the winter case. For HPT2, the temperature increases to values between 40.1 °C and 47.84 °C during the first refueling hour, and up to 40.17 °C (for a pre-cooling temperature of –40 °C) and 53.2 °C (for 0 °C) during the second. For HPT3, the gas temperature rises from 40.1 °C to 52.05 °C during the first refueling and from 40.16 °C to 59.57 °C during the second.

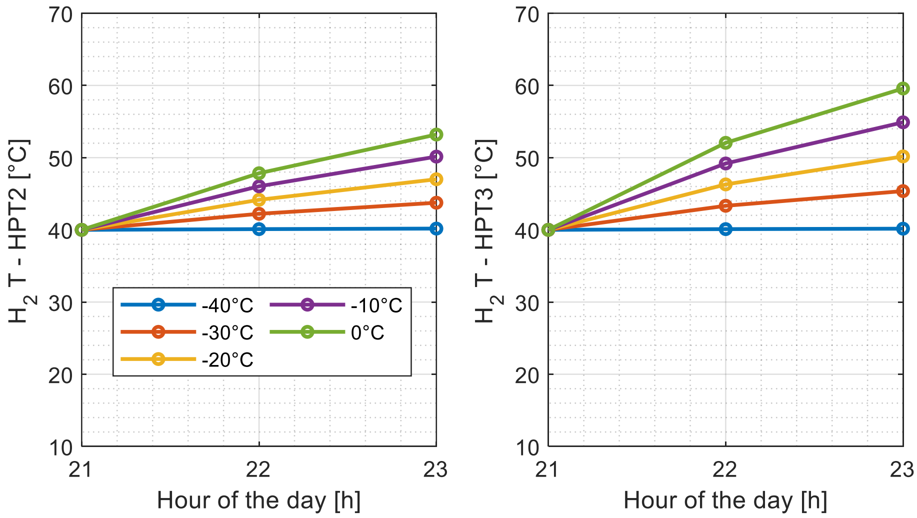

Figure 2.31 - Daily trend of hydrogen temperature: summer.

Overall, the analysis of gas temperatures at the end of the first refueling block in tanks HPT2 and HPT3 reveals a cyclical similarity. However, a comparison between seasons highlights a clear difference in final gas temperatures between the first and second hour of refueling, more pronounced in winter conditions and with a "flattening" effect observed in the summer case.

In winter (ambient T = 10 °C), for the same PC temperature, the temperature difference between the first and second refueling operations is greater than in summer (ambient T = 40 °C). This behaviour can be attributed to the differing thermal balance between the system and its surroundings. During winter, the lower ambient temperature reduces the effectiveness of heat exchange with the environment, leading to residual heat accumulation in the tanks after the first refueling. Consequently, the second refueling starts from a less favourable thermal condition, resulting in a more pronounced increase in gas temperature. In contrast, during summer, the higher ambient temperature promotes faster heat dissipation, allowing the system to reach quasi-steady thermal conditions between consecutive refueling events. This results in a more uniform temperature trend and a smaller temperature difference between successive cycles.

Moreover, increasing the PC temperature gradually diminishes the initial cooling effect. This implies that a deeper PC is particularly effective in summer, due to the larger thermal gradient between the precooled gas and the environment. Conversely, under winter conditions, the system's lower ability to dissipate the accumulated heat means that, even with aggressive pre-cooling, the final hydrogen temperatures remain relatively higher.

Regarding the maximum gas temperature values reached during the seasons, the results indicate that the maximum values inside the tanks reach 53.2 °C for HPT2 and 59.57 °C for HPT3, with both values relating to the summer case and at a PC temperature of 0 °C after the second hour of refuelings (23). Both values are well below the SAE protocol limit, which specifies a maximum gas temperature of 85 °C. Furthermore, since cascade storage tanks experience greater thermal stress during daytime operations compared to vehicle tanks, these results ensure an adequate thermal safety margin, both to comply with regulations and to preserve the integrity of the materials and prevent deterioration.

To evaluate the decrease in gas temperature during the first idle period (from 23 to 5), dynamic simulations were performed for each seasonal scenario with varying precooling temperatures. The initial gas temperature at the start of the pause was set equal to the final temperature reached at the end of the second refueling hour for both the cascade system and the LPT.

The gas temperature results after the six-hour pause showed values close to ambient temperature for both tanks during the summer season, considering a precooling temperature of -40°C. Specifically, HPT2 exhibited a gas temperature of 40.08°C, while HPT3 reached 40.09°C. The temperature difference between the gas at the beginning of the pause and the ambient temperature was less than one degree for both tanks, which facilitated rapid thermal equilibration between the gas and the environment.

During spring, still considering a precooling temperature of -40°C, the results showed final gas temperatures of 30.8°C for HPT2 and 31.21°C for HPT3. For higher precooling temperatures, elevated final gas temperatures were observed at the end of the pause, reaching up to +5°C above ambient in the worst case (PC = 0°C). The temperature difference between the gas at the beginning of the pause and ambient temperature was 4.86°C for HPT3 and 3.03°C for HPT2, greater than in summer.

Regarding the autumn results, final gas temperatures of 21.24°C for HPT2 and 22.11°C for HPT3 were obtained, again considering a pre-cooling temperature of -40°C. The temperature difference between the gas at the start of the pause and the ambient temperature was 9.44°C for HPT3 and 5.12°C for HPT2. In the worst case, the gas temperature exceeded the ambient temperature by approximately 6°C.

Finally, in the winter case, the results showed temperatures slightly higher than ambient, again considering a precooling temperature of -40°C (12.62°C for HPT3 and 11.36°C for HPT2). For all other precooling temperatures during winter, the final gas temperature was at least 3.5–7.5°C higher than ambient temperature; therefore, these results are not considered satisfactory. The temperature difference between the start of the first pause and ambient temperature was 13.58°C for HPT3 and 6.74°C for HPT2.

The winter case therefore represents the most critical seasonal scenario. The temperature evolution for this season is illustrated in Figure 2.32 (HPT2) and Figure 2.33 (HPT3), covering both the first two refueling hours and the subsequent idle period. The temperature trends (gas and walls) follow the same behaviour described in Figure 2.13, exhibiting characteristic phases of emptying, filling, and thermal recovery during the pause. As previously established, the initial temperature during the first hour is set to ambient temperature, while the starting conditions for the subsequent hours (22 and 23) correspond to the final temperature of the previous hour for both gas and walls. As mentioned, final temperatures after the pause of 11.36°C for HPT2 and 12.62°C for HPT3 were reached. The dynamic evolution between the first and second hours is nearly identical for gas temperature and shows slight differences for wall temperature in the initial phase. Similar trends were observed in the other seasons, with the primary distinction being the different ambient temperature and minor variations in final gas temperature, resulting in vertically shifted temperature profiles.

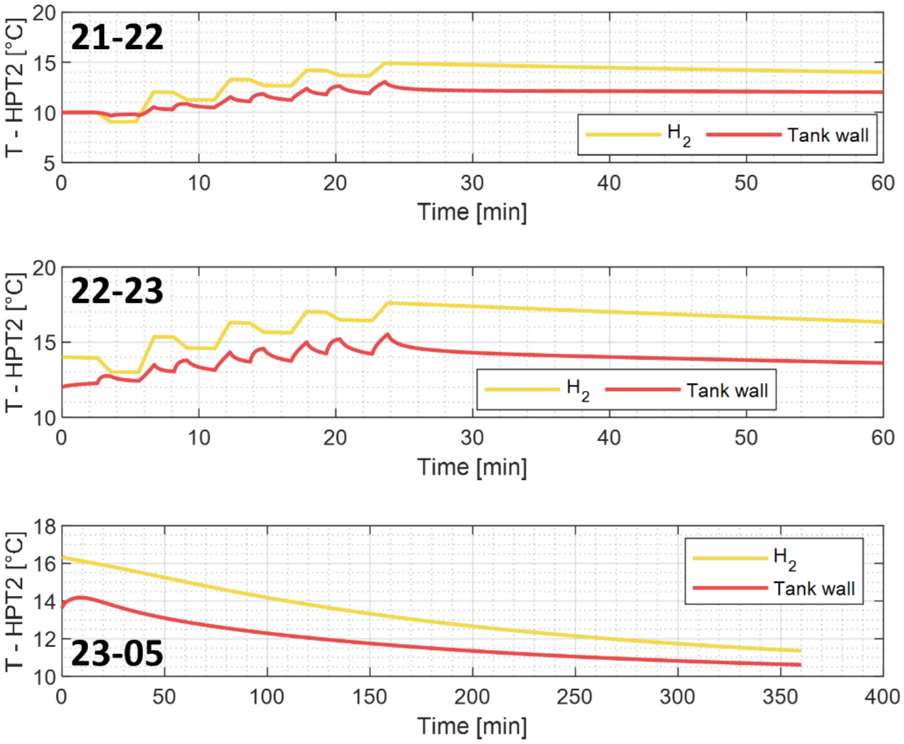

Figure 2.32 - Dynamic temperature trend (winter season) in HPT2 during the first refueling block and first pause.

The analysis of gas temperature evolution during the 6-hour idle period reveals that winter conditions represent the most critical scenario for thermal recovery, confirming the trends already observed in the previous seasonal analysis of refueling operations. Despite aggressive precooling (-40°C), the system struggles to dissipate accumulated heat due to the limited thermal gradient between the gas and the cold ambient environment (10°C). Conversely, summer conditions prove to be the most favorable case: the large temperature difference between the precooled inlet gas (-40°C) and the high ambient temperature (40°C) promotes efficient heat exchange, enabling the gas to reach near-ambient conditions (40.08-40.09°C) by the end of the idle period, consistent with the enhanced heat dissipation capacity previously identified for high-temperature scenarios.

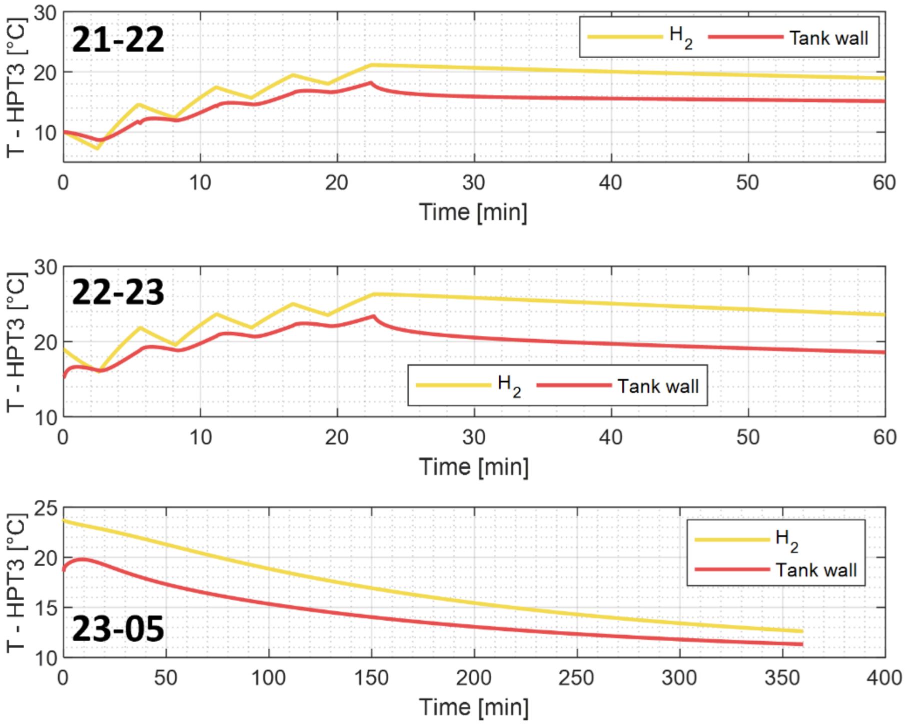

Figure 2.33 - Dynamic temperature trend (winter season) in HPT3 during the first refueling block and first pause.

Interestingly, HPT2 and HPT3 exhibit similar thermal behavior despite different initial temperature gradients relative to ambient conditions. This can be attributed to their differing volumes (1.95 m^3 vs 2.25 m^3): the larger thermal mass of HPT3 compensates for its higher initial temperature difference, resulting in comparable final temperatures. Both tanks share identical construction (Type IV, same materials and insulation characteristics), which explains their convergent thermal response.

It is important to note that the analysis focused on the most demanding refueling scenario (between hours 21-23), characterized by the highest hydrogen demand. In subsequent refueling cycles with lower hydrogen consumption, the reduced thermal stress on both tanks should facilitate more effective thermal recovery during idle periods, potentially mitigating or eliminating the issue of incomplete return to ambient temperature. This conservative approach ensures that if thermal equilibrium is achieved in the worst scenario, it will certainly be satisfied under less demanding operational conditions. However, while the observed temperature differences of 1-3°C above ambient in winter may appear acceptable for short-term operation, they pose a potential concern for long-term performance. If the system operates daily without achieving full thermal equilibrium, cumulative heat accumulation could occur, particularly during cold seasons. Over extended periods, this progressive thermal drift may lead to gradually increasing baseline temperatures, reducing the effectiveness of precooling and potentially approaching safety limits during peak demand periods. This phenomenon is exacerbated in winter when natural heat dissipation is minimized, creating a thermal "debt" that cannot be recovered between refueling cycles.

To mitigate these challenges and ensure consistent return to ambient conditions, several operational strategies should be considered:

- extended idle periods during winter months to allow sufficient time for thermal equilibration;
- buffer tank implementation to decouple high frequency refueling from cascade storage, reducing thermal stress on HPT2 and HPT3 or higher volumes for both tanks;
- strategic use of HPT1 when hydrogen inventory permits, allowing HPT2 and HPT3 to recover thermally while maintaining refueling capability;
- active cooling systems for the cascade system during extended idle periods in winter, though this would increase energy consumption;
- bypass strategies during low-demand periods, redirecting flow to allow individual tanks to undergo thermal recovery.

The selection of appropriate mitigation strategies should balance operational complexity, energy consumption, and long-term system reliability, with particular attention to seasonal variations in thermal behavior.

The overall seasonal results, referring to the second refueling hour (considered more critical than the first especially for energy consumption) are reported in Table 2.13. The input parameters used in the dynamic model are those listed in Table 2.12. As shown in the results, with increasing ambient temperature and keeping all other initial parameters constant, the refueling time slightly increases, while the maximum hydrogen flow rate delivered by the dispenser remains constant.

Regarding the maximum pressure values, the VT experiences a slight increase with rising ambient temperature, while the cascade system tanks (with the exception of HPT1, which maintains an SOC close to its nominal value) exhibit a slight decrease. This outcome is consistent with the results obtained from the parametric analysis carried out with varying ambient and PC temperatures: at a fixed PC temperature, lower ambient temperatures make heat dissipation more difficult, leading to slightly higher final values. Furthermore, in the LPT, the pressure results remain well above the lower operating limit.

The maximum gas temperature results show an increasing trend with rising ambient temperature. In the VT, the maximum temperature increases from approximately 24 °C in winter to 45 °C in summer, remaining well below the 85 °C limit. The maximum temperatures of the cascade system are reported for both the first refueling hour (21) and the second (22). The HPT1 displays nearly constant values, since it does not undergo emptying phases. HPT2 reaches maximum temperatures equal to the final values at the end of each refueling hour (as reported earlier), whereas the HPT3 exhibits slightly higher peak temperatures compared to its final ones. This behaviour is related to the system logic implemented in the model: since HPT3 has priority during the filling sequence, once it reaches 100% SOC, it enters a standby phase during which its temperature slightly decreases. The model is also configured to stop once all refueling operations are completed and the overall SOC of the cascade system reaches 100%, meaning that HPT2 does not have sufficient time to experience a similar temperature drop.

Table 2.13 - Seasonal results for the HRS studied – Real case.

Parameters		Winter	Autumn	Spring	Summer
Ambient temperature	[°C]	10	20	30	40
Pre-Cooling temperature	[°C]	-40	-40	-40	-40
Refueling Time	[min]	3.56	3.6	3.64	3.68
Max MF Dispenser	[g/s]	80.4	80.4	80.4	80.4
Max p VT (<43.75)	[MPa]	31.82	32.58	33.64	34.11
Max p HTP1 (<56.25)	[MPa]	44.99	44.99	44.99	45.15
Max p HTP2 (<50)	[MPa]	41.17	40.89	40.52	40.07
Max p HTP3 (<43.75)	[MPa]	37.15	36.4	35.72	35.07
Min p LPT (>1.5 MPa)	[MPa]	3.07	3.04	3.02	2.99
Max T VT	[°C]	24.07	31.04	38.02	45
Max T HTP1 (Ref. 21-22)	[°C]	10	20	30	40.03
Max T HTP1 (Ref. 22-23)	[°C]	10	20	30	40.03
End T HPT1 (Idle 23-05)	[°C]	**10**	**20**	**30**	**40**
Max T HTP2 (Ref. 21-22)	[°C]	14.91	23.72	32.16	40.14
Max T HTP2 (Ref. 22-23)	[°C]	17.6	25.99	33.51	40.22
End T HPT2 (Idle 23-05)	[°C]	**11.36**	**21.24**	**30.8**	**40.08**
Max T HTP3 (Ref. 21-22)	[°C]	21.13	27.31	33.72	40.17
Max T HTP3 (Ref. 22-23)	[°C]	26.32	31.12	35.68	40.23
End T HPT3 (Idle 23-05)	[°C]	**12.62**	**22.11**	**31.21**	**40.09**
Min T LPT	[°C]	7.98	16.55	25.12	33.56
Min SOC HPT1	[%]	100	100	100	99.93
Min SOC HPT2	[%]	92.3	90.81	89.36	87.93
Min SOC HPT3	[%]	78.09	79.87	80.74	81.57
Min SOC LPT	[%]	90.43	88.2	87.81	87.39
Max HC Power	[kW]	392	390.05	389.34	390.92
HC Cons.	[kWh]	104.67	103.64	103.27	103.1
Max PC1 Power	[kW]	26.68	26.66	26.64	27.7
PC1 Consumption	[kWh]	3.09	3.23	3.31	3.4
Max PC2 Power	[kW]	39.8	43.1	46.07	49.03
PC2 Consumption	[kWh]	7.63	8.49	9.32	10.13
Total Power	[kW]	458.52	459.81	462.05	467.65
Total Consumption	[kWh]	115.39	115.36	115.89	116.64

Finally, regarding component power consumption, the HC shows a slight decrease in energy demand with increasing ambient temperature, with values ranging between 103 kWh and almost 105 kWh. Conversely, the energy consumption of both pre-cooling systems increases as ambient temperature rises. This trend is due to the fact that, at higher ambient temperatures, cooling the gas becomes more energy intensive. Moreover, the PC1 unit exhibits lower energy consumption than PC2, since the hydrogen flow cooled by PC1 enters at a lower temperature (15 °C, at the outlet of the HC) compared to that of PC2, which handles the gas after compression-induced heating. The total energy consumption amounts to approximately 116 kWh.

2.9 Results summary and conclusions

This chapter presented the development of a mathematical and thermodynamic model of a 35 MPa HRS designed to supply hydrogen buses operating on urban routes. The model, implemented in Matlab-Simulink, integrates all main station components (LPT, HC, HPT cascade system, PC, and VT). In particular, the VT was validated against experimental data, achieving errors below 1% for pressure and temperature predictions.

A comprehensive thermodynamic analysis of critical parameters (hydrogen mass flow rate, pressure, temperature) was conducted for each system component. To evaluate station performance under different conditions, a two-level approach was followed: a parametric analysis to determine the maximum station capacity and a realistic analysis based on actual bus fleet demand.

Regarding the parametric analysis, the main objective was to identify optimal initial conditions to maximize the number of consecutive refuelings, starting from initially empty vehicles (VT SOC = 10%). Favourable configurations were identified for 5, 6, 7, and 8 consecutive refuelings. Results demonstrated that pressure and temperature remain consistently below the limits imposed by the SAE J2601-5 protocol, with minimum energy consumption for 6 refuelings and refueling times ranging from 3.45 to 7.15 minutes.

In the realistic simulation, the daily hydrogen demand from a bus fleet was considered, which allowed for defining a more realistic initial VT SOC value (57%). An additional pre-cooling system was integrated upstream of the cascade system to limit temperature rise in the HPTs, which is particularly critical during the second hour of refuelings. A seasonal parametric analysis was conducted to determine the optimal pre-cooler temperature as a function of ambient conditions. By adapting the optimal parameters from the parametric analysis case to the actual number of daily refuelings (4-6), results showed that pressure and temperature remain below SAE J2601-5 limits for all system components throughout the entire year, ensuring continuous station operability. Refueling times are approximately 3-4 minutes, consistent with current operational standards for hydrogen buses.

Overall, the results demonstrate that the proposed control logic for the cascade system, combined with aggressive precooling (-40°C), enables safe and efficient HRS operation under variable demand conditions. However, winter operation requires additional thermal management strategies, such as extended idle periods or strategic tank rotation, to prevent long-term heat accumulation and ensure sustained compliance with temperature limits. The validated model provides a flexible tool for adapting station design and control strategies to different seasonal and operational scenarios.

The next chapter extends this analysis by investigating the integration of the HRS into a renewable microgrid to assess the techno-economic feasibility of green hydrogen production.

3. Hydrogen Refueling Station Integration in a Renewable Microgrid

This chapter presents the integration of the previously analysed HRS into a renewable energy-based microgrid. A mathematical model is developed in Matlab to evaluate the microgrid performance under different Energy Management Strategies (EMS), each characterized by an increasing share of green hydrogen production.

The microgrid model was then optimized to determine the optimal component sizing for two objective functions: maximizing the Self-Sufficiency Ratio (SSR) and minimizing the Levelized Cost of Hydrogen (LCOH). The LCOH analysis enables evaluation of the additional costs associated with integrating energy storage systems for continuous green hydrogen production, compared to the costs of operating the electrolyzer exclusively with grid electricity.

Additionally, a comprehensive cost analysis considers both the revenue from surplus electricity sales and the expected decrease in Hydrogen Generator (HG) costs in the coming years. Finally, the avoided CO_2 emissions are quantified for each EMS, including both emissions from Fuel Cell Electric Vehicle (FCEV) operation and those related to the renewable electricity powering the electrolyzer and HRS components.

3.1 Renewable microgrid with HRS system configuration

The renewable-based microgrid considered is characterized by a PV system coupled with a BS and a hydrogen production, storage and utilization system, composed of a Hydrogen Generator (HG), a LPT, a Hydrogen Compressor (HC), a Pre-Cooling Unit, a cascade system of HPTs, a second Pre-Cooling Unit and the VTs. Therefore, starting from the HRS system shown in Figure 2.1 and after adding the second PC before the cascade system, in this case 3 new components (PV, BS and HG) were considered. As shown in Figure 3.1, the renewable microgrid is also connected to the Public Grid (PG), in order to study two different EMSs, characterized by an increasing share of renewable energy used for green hydrogen production, compared finally to the hydrogen production costs obtainable by powering the HG only with the public grid. The figure also shows how all the components that require electrical energy (HG, HC, and PCs) are supplied. Specifically, electrical power is provided by the PV system, the BS, or, when necessary, by the PG.

As explained in the previous paragraph, the purpose of the HRS integration in a renewable microgrid concerns the supply of green hydrogen to the bus fleet considered in Section 2.8. Starting from the daily hydrogen demand, the annual hydrogen demand of the HRS was determined, assuming that the buses operate every day of the year. Furthermore, based on the seasonal energy consumption results of the HRS components (obtained in section 2.8.2), the corresponding hourly electrical energy demand for the entire year was generated, accounting for the appropriate consumption levels in each season. The annual hydrogen demand of the HRS amounts to 100.25 t/y (equivalent to 3 948.2 MWh eq./y H_2), while the total annual energy consumption of the HRS (HC and two PCs) is 178.67 MWh/y.

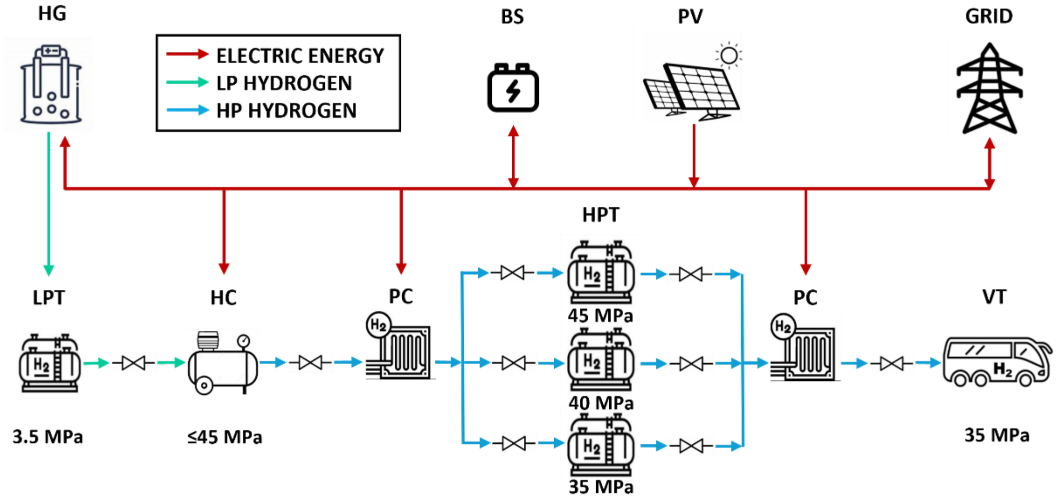

Figure 3.1 - Schematic system of the HRS integrated with the renewable-based microgrid.

The performance of the microgrid over a typical year was evaluated using a mathematical model developed in Matlab**,** which includes the new components (PG, PV, BS, and HG), the LPT, and the hydrogen and electrical demand of the HRS (the latter already optimized through dynamic modelling). The following sections describe the mathematical models implemented for the new components, in order to assess the expected performance of each component within the system.

3.2 PV system and battery storage mathematical modelling

The PV generation profile was simulated starting from a typical meteorological year dataset of the location considered obtained by Meteonorm Software [112]. In particular, the PV system is composed of modules characterized by a peak power of 355 Wp [113], while the overall size is considered a design parameter to be optimized. Regarding the PV plant orientation, an azimuth angle of -30° and a tilt angle equal to 30° were considered. The output power P_{PV} of the PV subarray was calculated by Equation (21):

$$P_{PV}(t) = P_{PV,nom}\,\frac{GI(t)}{GI_{NOCT}}\,\left[1+\gamma\left(T_C(t)-T_{C,STC}\right)\right]\eta_{INV}\,f_{PV} \qquad (21)$$

where the incident radiation (GI_{NOCT}) was set equal to 800 W/m^2, the Cell Temperature under Standard Test Conditions ($T_{C,STC}$) is equal to 25°C, the PV temperature coefficient (γ) is -0.0027 1/°C, while the inverter efficiency (η_{INV}) is given by the manufacturer as a function of the PV power output. Secondary losses, like wiring losses, shading, soiling of the modules and aging are accounted in a derating factor f_{PV} equal to 0.9. The Global Irradiance (GI) and the operating Cell Temperature (T_C) were calculated using the method proposed by Duffie and Beckman [114].

Regarding the energy stored in the BS, this was evaluated by determining its SOC as reported in Equation (22), which indicates the ratio between the amount of stored energy and the nominal storage capacity:

$$SOC_{BS}(t) = SOC_{BS}(t-1) + \frac{\left[P_{BC}(t)\eta_{BC} - \frac{P_{BD}(t)}{\eta_{BD}}\right] \Delta t}{E_{BS}} \tag{22}$$

where P_{BC} is the power input during Battery Charging (BC) phase and P_{BD} is the power output during Battery Discharging (BD) phase. The batteries efficiency during BC and BD phases (η_{BC} and η_{BD}) were set equal to 98% and 97% respectively, since the considered batteries are lithium type, while the applied time step (Δt) and the battery Depth-of-Discharge (DOD) were assumed equal to 1 h and 80% respectively [110]. The battery capacity (E_B), as for the PV system, is a design parameter to be optimized.

3.3 Hydrogen section mathematical modelling

The hydrogen section includes a HG and an LPT, in which hydrogen is stored up to the HG delivery pressure (while the minimum pressure is set equal to 1.5 MPa, equal to the minimum working pressure of the HC as previously explained). The size of the HG and the capacity of the LPT were considered design parameters to be optimized during the performance analysis.

Concerning the HG, a commercial electrolyzer based on the Proton Exchange Membrane (PEM) technology, with a hydrogen production of 1 Nm^3/h at 35 barg, was considered. According to the manufacturer specification [115], it was assumed that the HG can operate in a range between 20% and 100% of its rated power. The HG often operates in off-design mode with variable efficiency, as the PV power supplying the hydrogen section and the user needs are time dependent. Therefore, the hydrogen mass flow rate $\dot{m}_{HG}$ produced by a given HG power supply P_{HG} depends on the electrolyzer efficiency η_{HG} [115], given by Equation (23):

$$\eta_{HG}(t) = \frac{\dot{m}_{HG}(t)\, HHV_{H_2}}{P_{HG}(t)} \tag{23}$$

where HHV_{H_2} is the Higher Heating Value of the hydrogen.

Finally, the energy stored inside the LPT at a given time was evaluated based on the SOC, determined by Equation (24):

$$SOC_{LPT}(t) = SOC_{LPT}(t-1) + \frac{[\dot{m}_{HG}(t) - \dot{m}_{HC}(t)]\, HHV_{H_2} \cdot \Delta t}{E_{LPT}} \tag{24}$$

where $\dot{m}_{HG}$ and $\dot{m}_{HC}$ are the hydrogen mass flow rate produced by the HG and compressed by the HC respectively, while E_{LPT} is the hydrogen storage capacity expressed in energy terms of the LPT. Equation (24), in detail, allows to evaluate the energy converted by the hydrogen generator and stored in the LPT.

3.4 Energy management strategies proposed

To evaluate the performance of the renewable microgrid under increasing shares of green hydrogen production, different Energy Management Strategies (EMSs) were developed. The EMSs were implemented in Matlab and then optimized to determine the optimal sizing of the microgrid components, particularly the PV system, BS, HG, and LPT, capable to obtain the lowest LCOH at the highest SSR. Specifically, 3 different EMSs were investigated.

The first EMS refers to the green hydrogen production EMS, illustrated in Figure 3.2. The black section represents the logical framework governing hydrogen production from the PV and/or BS systems, while the green section describes how the HRS demand is supplied by the LPT. Each logic node and its corresponding control action are identified by matching colours.

Specifically, the yellow node determines the amount of energy available for hydrogen production, calculated as the PV generation minus the power consumption of the HRS components. If the available energy exceeds the minimum required by the HG, a check on the LPT (orange node) is performed to decide whether hydrogen should be produced under nominal or partial load conditions (pink node). When hydrogen production is possible but the LPT lacks sufficient free capacity, the surplus PV energy, after covering HRS consumption, is directed to the BS or, if the batteries are fully charged, exported to the grid (light blue node). Conversely, if the available energy is insufficient to run the HG at its minimum power, a check on the BS is carried out to enable operation using both PV and BS energy sources (blue node). When enough storage capacity is available in the LPT, hydrogen is produced at either intermediate or nominal power (brown node). Otherwise, the PV production is sent to the grid.

With regard to hydrogen demand from the HRS (pink node, green section), if the LPT cannot fully satisfy the total requirement it provides a partial supply, depleting its storage down to the minimum level (grey node).

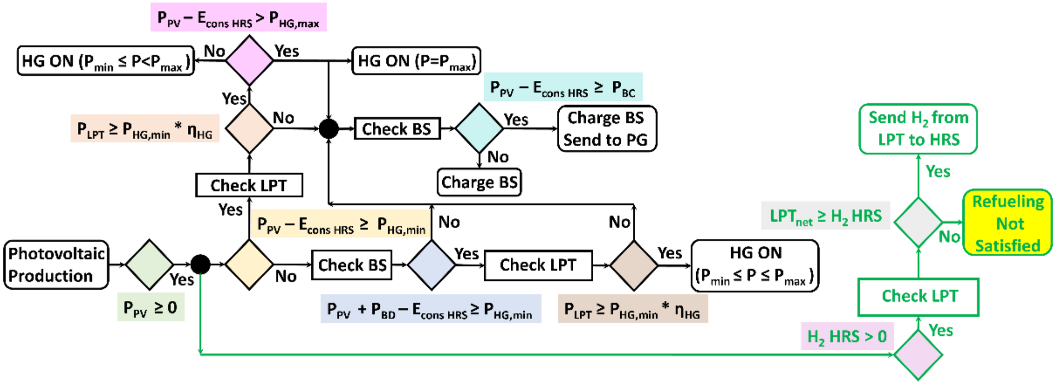

Figure 3.2 - Energy management strategy scheme of the green hydrogen production case.

The EMS corresponding to the mixed hydrogen production strategy is illustrated in Figure 3.3. As shown, the black section (hydrogen production from PV + BS) and the green section (hydrogen supplied to the HRS) are identical to those of the green hydrogen production EMS. The main difference lies in the red section, which concerns hydrogen production using electricity from the grid, activated when there is a deficit relative to the HRS demand. Specifically, when a hydrogen demand from the HRS occurs (dark grey node), a check on the LPT is performed five hours before the scheduled refueling time (dark green node). If the amount of hydrogen available, considering both the current storage level and the quantity expected to be produced in the next five hours from PV + BS energy, is lower than the HRS demand (violet node), the deficit is compensated by producing hydrogen using electricity from the grid (light yellow node).

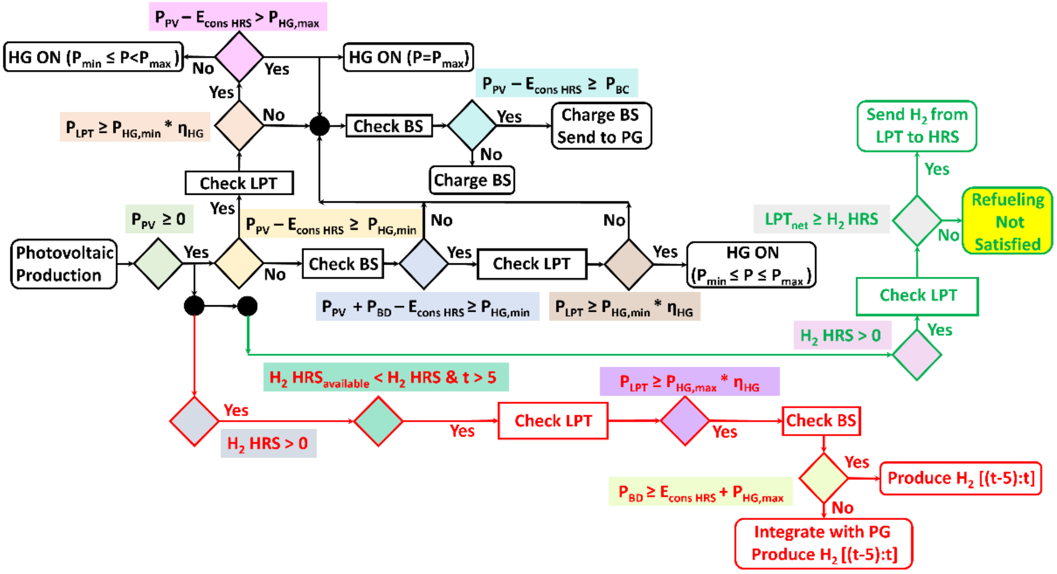

Figure 3.3 - Energy management strategy scheme of the mixed hydrogen production case.

The two proposed EMSs were then compared with an EMS characterized by hydrogen production exclusively with energy from the grid. In this case the EMS is similar to the Mixed EMS one, with the black part excluded (PV and BS are not present). Furthermore, in the red part, the hydrogen production with energy from grid covers the whole day.

3.5 Microgrid optimization settings

A multi-objective optimization is formulated and solved with the goal of finding the best optimal design of the renewable-based microgrid by considering two conflicting objective functions: the maximization of the self-sufficiency rate (SSR) and the minimization of the Levelized Cost of Hydrogen (LCOH). The first function indicates the microgrid ability to satisfy the HRS demand (ratio between the amount of green hydrogen produced by the HG, $\dot{m}_{HG,green}$, and the total quantity required, $\dot{m}_{HRS}$, as reported in Equation (25)), while the second indicates the ratio between the total expenditure and the hydrogen delivered (m_{HRS}) to the HRS (Equation (26)).

These two objectives are inherently conflicting: increasing the SSR typically requires oversizing renewable and storage components, which raises investment and operational costs, thus leading to a higher LCOH. Conversely, minimizing the LCOH often results in a smaller renewable share and higher grid dependence, thereby lowering the SSR. Therefore, the optimization problem cannot yield a single global optimum but rather a set of non-dominated solutions that represent the trade-off between autonomy and cost. The resulting Pareto front illustrates this compromise, providing the designer with a spectrum of feasible configurations from cost-effective to highly self-sufficient systems. The final design can then be selected based on technical or economic preferences (e.g., lowest LCOH, highest SSR, or balanced configuration).

$$SSR = \frac{\sum_t \dot{m}_{HG,green}(t)}{\sum_t \dot{m}_{HRS}(t)} \tag{25}$$

$$LCOH = \frac{TCI + (E_{FG} \cdot c_{E,FG} + OM \cdot TCI) \cdot \sum(1 + IR)^{-y}}{m_{HRS} \cdot \sum(1 + IR)^{-y}} \tag{26}$$

where the term TCI was calculated by Equation (27), starting from the Purchase Equipment Costs (PEC) as a function of the relative size of the hydrogen section components and their specific costs c (listed in Table 3.1), $c_{E,FG}$ indicates the specific cost for the energy purchased from the grid multiplied by the total quantity of energy purchased (E_{FG}), OM represents the Operating and Maintenance costs, IR is the Interest Rate and y the total lifetime. The terms E_{FG}, OM and m_{HRS} were considered constant throughout the useful life.

Regarding Equation (26) it can be observed that, while the cost of purchasing electricity from the grid has been included throughout the term E_{FG}, the revenue from selling surplus renewable energy has instead been excluded. This choice is due to the optimisation logic, which aims to minimise costs: including the revenue from energy sales would have led the optimisation process to oversize the PV system excessively, in order to sell more electricity and thereby reduce the LCOH. Since this outcome would go beyond the actual objectives of the overall system (the production and supply of green hydrogen to the HRS when required), this aspect was therefore deliberately omitted.

$$\begin{aligned} TCI = \Bigg(& c_{PV} \cdot P_{PV} + c_{BS} \cdot \frac{E_{BS}}{DOD_{BS}} + c_{HG} \cdot {P_{HG}}^{0.885} + c_{LPT} \cdot m_{LPT} \\ & + \sum_{i=1}^{3} c_{HPT,i} \cdot m_{HPT,i} + c_{HC} \cdot {P_{HC}}^{0.6038} + c_{PC1} \cdot P_{PC1} \\ & + c_{HRS} \Bigg) (1 + c_{BOP})(1 + c_{EC}) \end{aligned} \tag{27}$$

Table 3.1 - Main parameters assumed for the economic analysis [115–117].

Parameter		Value	Parameter		Value
y	[year]	20	c_{HC}	[€/kW]	37 232.55
OM	[%]	5% TCI	$c_{HT\ HP}$	[€/kg]	1 390.35
IR	[%]	5	c_{PC1}	[€/kW]	500.77
c_{BOP}	[%]	10% PEC	c_{HRS}	[€]	158 100
c_{EC}	[%]	10	m_{HPT1}	[kg]	59
c_E	[€/kWh]	0.114	m_{HPT2}	[kg]	63.5
c_{PV}	[€/kW]	1 058.34	m_{HPT3}	[kg]	64
c_{BS}	[€/kWh]	697.5	P_{HC}	[kW]	400
c_{HG}	[€/kW]	3 165.72	P_{PC1}	[kW]	5
$c_{HT\ LP}$	[€/kg]	930.93			

In Equation (27), c_{BOP} are the costs for the balance of plant (expressed as a percentage of the PEC), c_{EC} are the Engineering Costs (expressed as a percentage of the PEC+BOP costs) and all powers or energy values are the nominal ones for each components.

In Table 3.1 are also reported the nominal quantity of hydrogen stored in the cascade system and the nominal power of HC and PC1 (before cascade system), while the PC2 costs are included in the cost related to the HRS.

The optimization problem is implemented in Matlab and solved using the *gamultiobj* function, which is based on the Non-Dominated Sorting Genetic Algorithm II (NSGA-II) [118]. A population of 2000 individuals was defined to ensure a wide exploration of the design space. The optimization stopped when the default convergence criteria of gamultiobj were met, either reaching the maximum number of generations (by default, 100 × number of variables) or achieving negligible improvement of the Pareto front over consecutive generations (default function tolerance = $1 \cdot 10^{-4}$). All the other genetic operators were kept at MATLAB default values:

- Selection method: tournament selection (default selection pressure = 0.75);
- Crossover operator: scattered crossover (default crossover fraction = 0.8);
- Mutation function: adaptive feasible mutation;
- Pareto ranking and elitism: controlled elitist strategy inherent to NSGA-II.

This configuration allowed balancing between exploration of the design space and convergence toward the non-dominated optimal solutions. The design variables to be optimized and the corresponding lower and upper bounds are:

- PV plant nominal power: 2 000 kW ÷ 10 000 kW;
- BS nominal capacity: 100 kWh ÷ 5 000 kWh;
- HG nominal power: 1 000 kW ÷ 3 000 kW;
- LPT geometrical volume: 50 m^3 ÷ 500 m^3.

In the next sections, the annual performance of the renewable microgrid based on different EMSs are shown and discussed. The results, represented by the Pareto front obtained from the multi objective optimization, are also compared with the hydrogen production costs resulting by powering the HG only with the public grid, highlighting the additional costs deriving from the requirement of storage systems to guarantee the production and use of green hydrogen.

3.6 Optimization results - Green Hydrogen Production EMS

This section reports the results regarding the Green Hydrogen Production EMS described before. The Pareto front and the variation in the sizing of the microgrid components for all points along the Pareto front, corresponding to increasing values of the SSR, are shown in Figure 3.4 and Figure 3.5, respectively. The shape of the Pareto front curve shows the conflict between the two outcomes: lower costs (17.81 €/kg) result in low self-sufficiency values (80.44%), while higher costs (25.11€/kg) must be accepted to achieve a 100% SSR.

Concerning the components sizes showed in Figure 3.5, all parameter values lie between the lowest and highest values of the two objective functions. As can be seen, achieving a 100% SSR (associated with an increase in LCOH till 25.11 €/kg) requires larger component sizes: both the PV system and the HG exhibit a nearly linear increase in their nominal power. A general increase in the LPT volume is also observed, although this trend appears somewhat discontinuous, while the BS capacity remains almost unchanged.

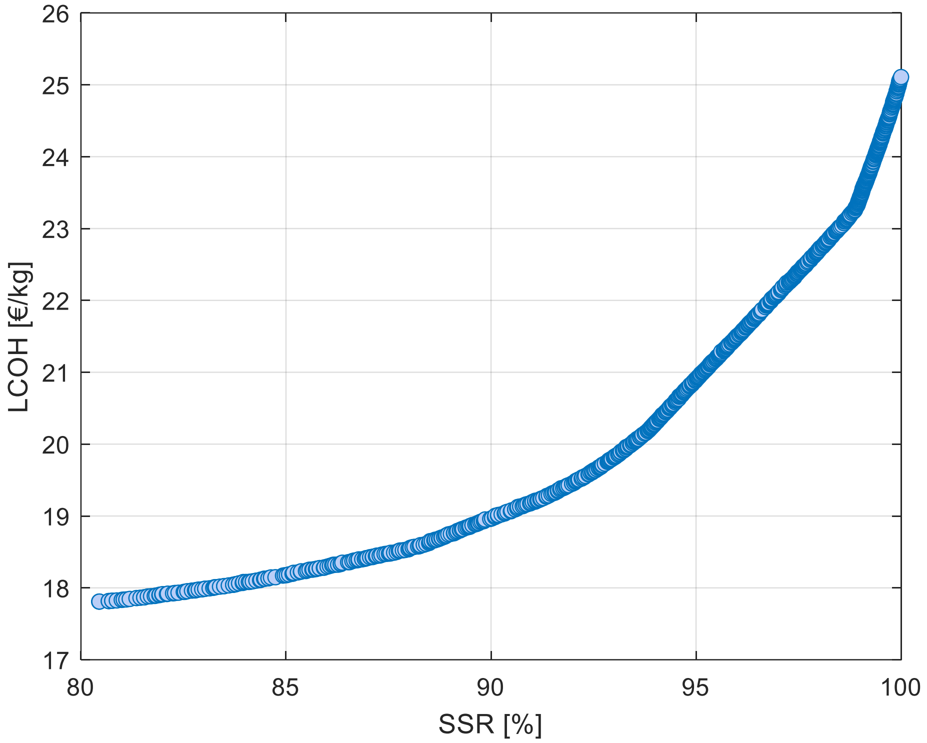

Figure 3.4 - Pareto Front resulting from the Green Hydrogen Production EMS.

As showed before, the lowest LCOH, equal to 17.81 €/kg, is obtained for the configuration with the minimum SSR of 80.44%, whereas achieving a 100% SSR results in an increase of the LCOH to 25.11 €/kg. This rise in hydrogen production cost can be explained by comparing the design variables associated with these two extreme configurations:

- Lowest LCOH: PV=3 977.7 kW; BS=197.95 kWh; HG=1 916.7 kW; LPT=128.07 m^3;
- Highest SSR: PV=8 397.6 kW; BS=384 kWh; HG=2 908.8 kW; LPT=462.21 m^3.

As can be observed, all components increase in size, especially PV, BS and LPT, which increase by more than double, while only HG increases to a lesser extent. In particular, the increase in SSR is mainly achieved through the significant expansion of the PV capacity, which roughly doubles when comparing the two extreme cases (lowest LCOH vs. highest SSR). The larger PV field enables a higher amount of renewable energy generation, thus improving system autonomy but also leading to a greater surplus of electricity exported to the grid. In all configurations, the battery storage capacity remains relatively small compared to the PV size, indicating a marginal role in the overall system operation, mainly serving to smooth short-term fluctuations rather than providing large-scale energy shifting. An interesting trend can also be observed in the ratio between the HG and PV nominal powers, which decreases from approximately 0.5 in the lowest-LCOH case to around one-third in the highest-SSR configuration. This suggests that the improvement in SSR is primarily due to the increased renewable capacity and consequent longer operating hours of the electrolyzer, rather than a direct enlargement of the HG itself. However, this also implies a higher amount of surplus PV production that is sold to the grid, a point that connects with the following discussion on system energy balance and economic implications.

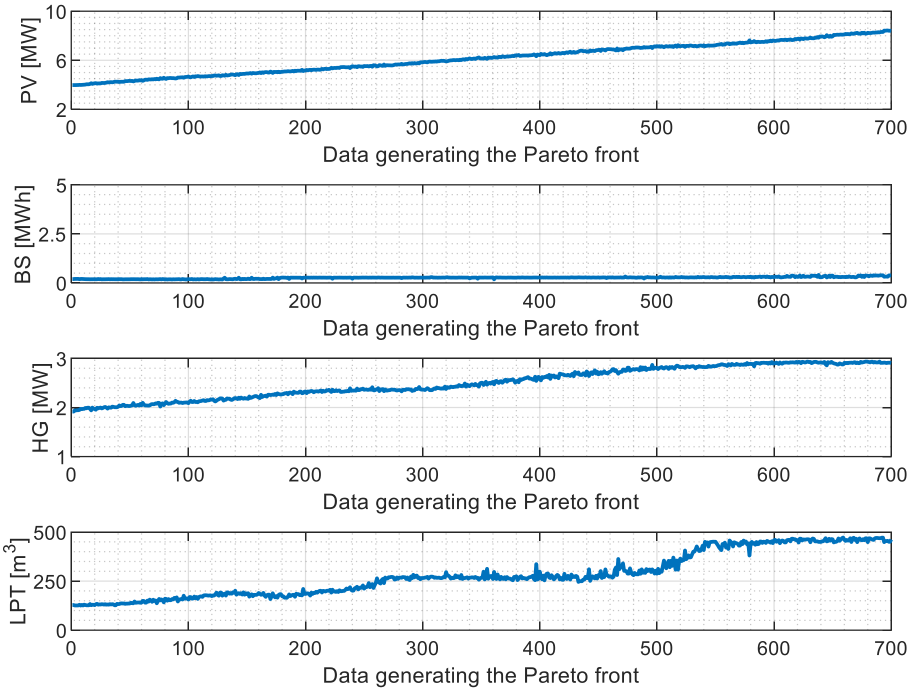

Figure 3.5 - Sizing of renewable-based microgrid components (Green EMS).

Since the possible revenue from electricity sold to the grid was excluded during the optimization process, the resulting LCOH value was subsequently corrected, as indicated in Equation (28).

$$LCOH^I = LCOH - \frac{E_{TG} \cdot c_{E,TG}}{H_2\ HRS_d} \tag{28}$$

where $LCOH^I$ represents the hydrogen production cost adjusted by subtracting the revenue from electricity sales, calculated as the product of the total amount of energy sent to the grid (E_{TG}) and the electricity selling price ($c_{E,TG}$). In particular, starting from the results obtained from the sizes of the microgrid components, the total quantity of energy transferred to the grid and of hydrogen actually supplied by dispensers was calculated. For the electricity selling price, three different electricity selling prices were considered:

- The Guaranteed Minimum Price (PMG), which for renewable energy plants in Italy in 2025 amounts to 0.0468 €/kWh for up to 1.5 GWh/y of electricity sold [119];

- The regional price for Sardinia, obtained as the weighted average of electricity prices during the first eight months of 2025, considering 60% of sales in Band 1, 30% in Band 2, and 10% in Band 3, resulting in a value of 0.0941 €/kWh [120];
- The national average price during the first quarter of 2025 for a renewable energy system, equal to 0.137 €/kWh [119].

The corrected LCOH results, obtained by applying the three electricity price values reported above to Equation (28) through the term $c_{E,TG}$, are shown in Figure 3.6.

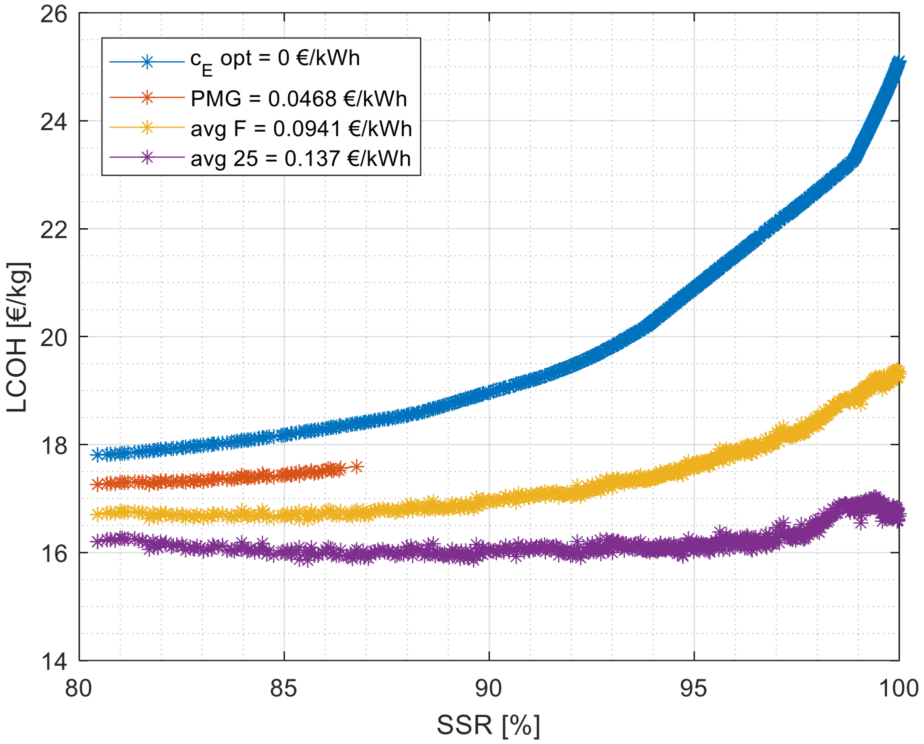

Figure 3.6 - Pareto Fronts resulting after LCOH correction (Green EMS).

Specifically, the curve corresponding to the LCOH calculated excluding any potential revenue from selling surplus renewable energy to the grid microgrid component sizes (illustrated in Figure 3.4) is represented by the blue line.

For the curve corresponding to the Guaranteed Minimum Price, only the points from the original Pareto front characterized by an annual energy export of ≤ 1 500 000 kWh were considered. However, the highest SSR obtained for this case is close to 87%. As expected from Equation (28), selling the surplus renewable electricity results in a decrease in the overall hydrogen production cost. Moreover, the purple curve, associated with the highest electricity selling price, exhibits a less uniform progression of LCOH values along the SSR range. This trend is due to the relationship present in equation (28): as the sales cost increases, in fact, this ratio increases, thus lowering the costs. Graphically, this result is shown with points further apart from each other in the curves, as the profit increases.

The minimum cost obtained (corresponding to an SSR of 80.44% for all cases) are range between 16.2 €/kg and 17.81 €/kg. The maximum values reach 19.35 €/kg for the Sardinian weighted average electricity price (avg F = 0.0941 €/kWh) and 16.72 €/kg for the national average price for the first quarter of 2025 (avg 25 = 0.137 €/kWh). Regarding the energy sent to the grid, the annual value varies from 945 841 kWh/y (lowest points) to 6 138 025 kWh/y (highest points).

3.7 Optimization results - Mixed Hydrogen Production EMS

Figure 3.7 shows the increase in component sizes obtained from the optimization of the Mixed EMS, corresponding to the points along the Pareto front shown in Figure 3.8. It should be noted that the SSR result considered in this case refers only to green hydrogen production: total SSR is always equal to 100%, since hydrogen production from grid electricity is allowed when hydrogen is unavailable. As previously observed, the PV and HG sizes exhibit a steady increase, while the LPT volume also grows but in a more discontinuous manner. The BS capacity, on the other hand, remains close to its lower limit, consistent with earlier findings.

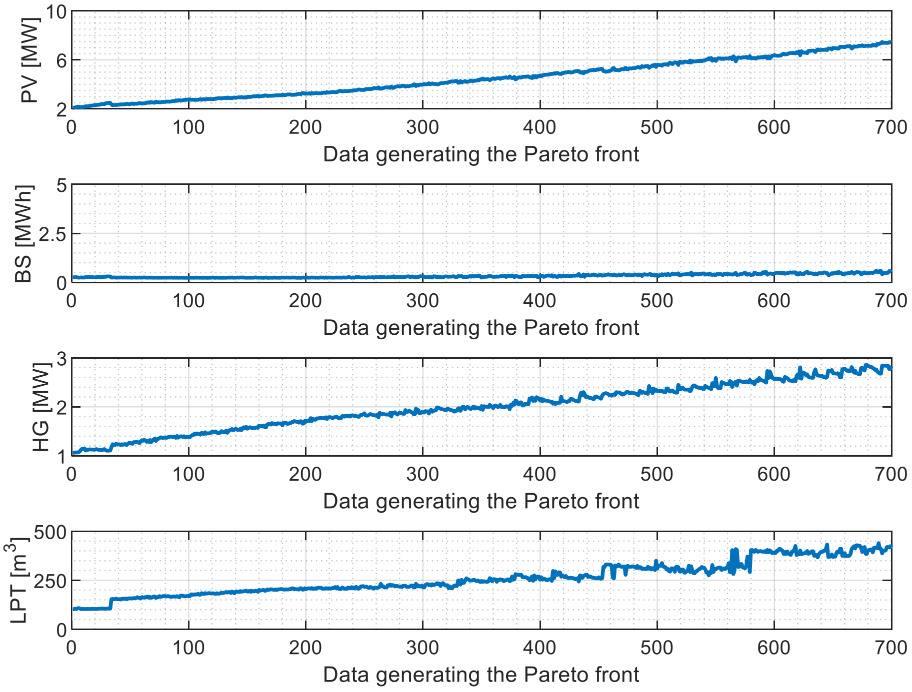

Figure 3.7 - Sizing of renewable-based microgrid components (Mixed EMS).

In this case, the SSR values are characterized by a wider range compared to the fully renewable configuration. In particular, the microgrid configurations achieving the lowest LCOH (13.1 €/kg, without selling the surplus energy) are characterized by a low SSR (47.34%): this means that the share of hydrogen produced by renewable is less than half. On the other hand, the 100% SSR results in a LCOH of 23.49 €/kg, slightly lower than that obtained in the previous case (25.11 €/kg). The sizes of the components for these two extreme cases are:

- Lowest LCOH: PV=2 088.3 kW; BS=258.41 kWh; HG=1 063.9 kW; LPT= 102.71 m^3;
- Highest SSR: PV=7 407.9 kW; BS=529.87 kWh; HG=2 834.5 kW; LPT=430.7 m^3.

The difference in size is evident for all components, with PV and LPT more than tripling, while BS and HG approximately double. This behaviour can be explained by the system's operating logic: achieving higher SSR values primarily requires increasing renewable generation capacity and hydrogen storage to reduce grid dependence and allow continuous hydrogen production. Conversely, battery capacity plays a secondary role, being used mainly for short-term power balancing rather than large-scale energy shifting, while the HG power grows moderately since the electrolyzer is increasingly operated for longer hours rather than being significantly upsized.

When compared to the Green EMS, the Mixed configuration exhibits overall smaller component sizes for both the lowest-LCOH and highest-SSR solutions. This is due to the additional flexibility provided by the grid connection, which compensates for renewable intermittency without requiring as large a PV or storage capacity. However, the relative trends remain consistent: PV and LPT still dominate the capacity increase as the SSR rises, confirming that renewable overgeneration and hydrogen storage expansion are the main drivers for improving system self-sufficiency, albeit at the expense of higher production cost.

As in the previous case, the LCOH results were corrected using Equation (28), and the corresponding outcomes are shown in Figure 3.8.

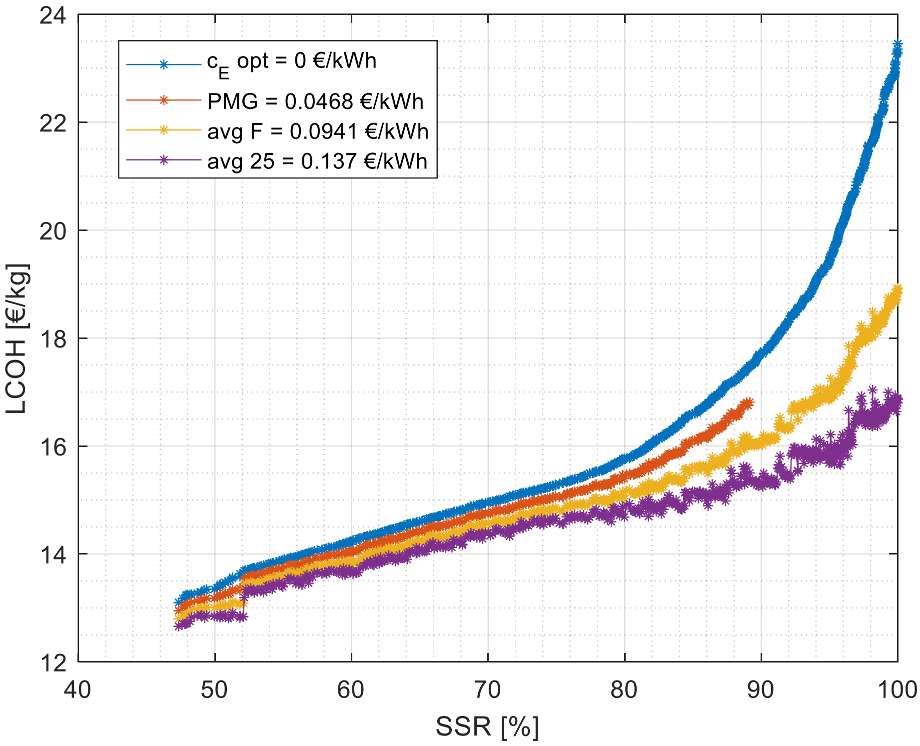

Figure 3.8 - Pareto Chart resulting from the Mixed Hydrogen Production EMS.

Unlike the Green EMS, the curves representing the corrected LCOH values are now less compressed downward. This behaviour may be explained by the fact that, except for a few initial points, the amount of hydrogen available for the HRS is almost always equal to the total required. Consequently, the denominator of the equation remains constant, unlike in the previous case where it increased with the

SSR. Furthermore, the curve corresponding to the minimum guaranteed price includes a greater number of cases in which the amount of energy sold to the grid is less than or equal to 1 500 000 kWh/y.

The minimum cost obtained (corresponding now to an SSR of 47.34% for all cases) are range between 12.66 €/kWh and 13.1 €/kg. The maximum values reach 19.02 €/kg for the Sardinian weighted average electricity price (avg F = 0.0941 €/kWh) and 16.98 €/kg for the national average price for the first quarter of 2025 (avg 25 = 0.137 €/kWh). Regarding the energy sent to the grid, the annual value varies from 322 545 kWh/y (lowest points) to 4 759 973 kWh/y (highest points).

In summary, the results obtained after the LCOH correction, thus considering the sale of surplus energy produced to the grid, are reported in Table 3.2. The values refer to an SOC of 100% (therefore to the highest cost obtained), except in the case of the PMG cost (0.0468 €/kWh), whose highest SSR value is indicated in parentheses. Considering the values obtained for an SSR of 100%, it can be observed that considering a selling price equal to 0.0941 €/kWh results in a cost reduction of 5.76 €/kg (Green EMS) and 4.47 €/kg (Mixed EMS). Considering instead the higher selling price (0.137 €/kWh), a reduction of 8.39 €/kg in the Green EMS and 6.51 €/kg in the Mixed EMS is achieved. Finally, it can be noted that the Green EMS case is characterized by both the highest cost (25.11 €/kg, without energy sale) and the lowest cost (16.72 €/kg): this may be due to the greater production and sale of electricity to the grid, and therefore to the larger PV size of the Green EMS at 8 398 kW, compared to that of the Mixed EMS at 7 408 kW.

Table 3.2 - Results summary for LCOH and LCOH' for Green EMS and Mixed EMS.

	$c_{E,TG}$ [€/kWh]				
	0	0.0468	0.0941	0.137	
	LCOH [€/kg]	LCOH' [€/kg]			SSR [%]
Green EMS	25.11	17.59 (86.77%)	19.35	16.72	100
Mixed EMS	23.49	16.81 (89.16%)	19.02	16.98	100

While Table 3.2 shows significant cost reductions through energy sales, the absolute LCOH values remain considerably high. To identify the main cost drivers and understand how the system configuration changes between different optimization objectives, Figure 3.9 and Figure 3.10 present the breakdown of the Total Capital Investment (TCI) for both Green and Mixed EMS configurations, considering the lowest LCOH and the highest SSR, respectively.

Figure 3.9 illustrates the TCI composition for the minimum LCOH solutions. In this scenario, the Green EMS requires a total investment of 10.95 M€, while the Mixed EMS achieves a lower investment of 7.26 M€ (33.7% reduction). The PV system represents the dominant cost component, accounting for 46.5% (Green EMS) and 36.8% (Mixed EMS) of the total investment. The HG contributes significantly with 28.1% and 25.2% respectively, while BS remains limited at 1.8% and 3.8%. The lower total cost of the Mixed EMS is primarily attributed to the smaller PV installation required (while PV represents similar percentages in both cases, the absolute investment is significantly lower due to the reduced system capacity) and the possibility of relying on grid electricity, eliminating the need for oversized renewable generation.

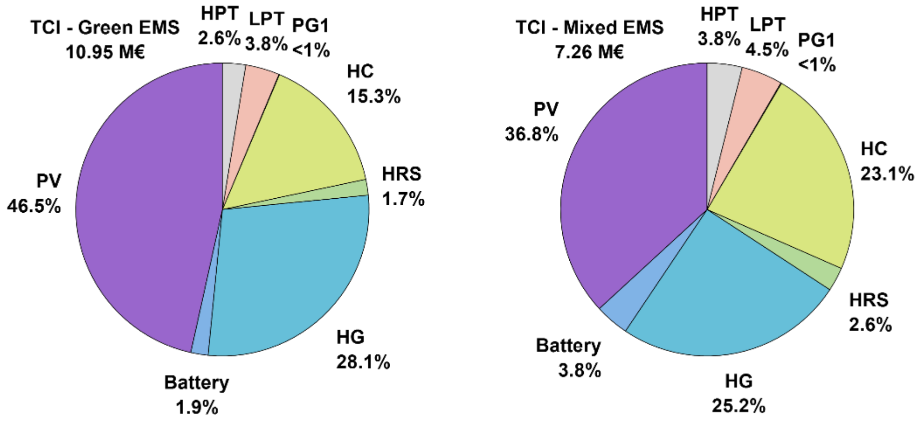

Figure 3.9 - Breakdown of the Total Capital Investment for the lowest LCOH.

Figure 3.10 shows the TCI breakdown for the 100% SSR configurations. In this case, the investment requirements increase substantially: the Green EMS reaches 19.25 M€ (75.8% increase from minimum LCOH) and the Mixed EMS 17.93 M€ (147% increase from minimum LCOH). The most notable change is the increased dominance of the PV system, which now represents 55.9% and 52.9% of the TCI, respectively. This shift reflects the need for significantly oversized photovoltaic capacity to ensure energy autonomy even during periods of low solar irradiation. BS also increases slightly to 2.1% and 3.1%, while the HG contribution decreases in relative terms (23.1% and 24.3%) despite maintaining similar absolute values. The larger percentage increase in the Mixed EMS investment (147% vs 75.8%) indicates that achieving self-sufficiency is particularly challenging and costly when starting from a grid-dependent optimum, as the system requires a more substantial redesign of its energy sources.

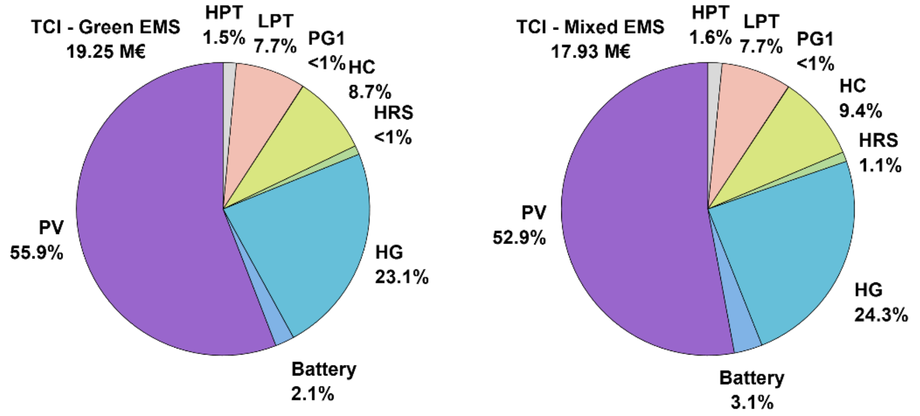

Figure 3.10 - Breakdown of the Total Capital Investment for the highest SSR.

3.8 Parametric analysis by varying the HG specific cost – Green EMS

A further cost analysis was conducted by varying the specific cost of the HG, whose cost is expected to decrease in the coming years [121,122]. As reported in Table 3.1, the specific cost of the HG considered so far is 3 165.72 €/kW, while to obtain the cost in € the power is raised to 0.885. Three other specific costs were therefore considered, while the calculation equation was kept the same: 1 191.48 €/kW, the cost forecast for 2030 according to [121], 545.69 €/kW, the cost forecast for 2050 with a total installed capacity of 1 TW [122], and 353.54 €/kW, the cost also forecast for 2050 but with a total installed power of 5 TW [122]

A multi-objective optimization was therefore performed by varying the specific cost of the HG for the Green EMS only, with the same characteristics as the previous optimization. The results are visible in Figure 3.11. The blue curve refers to the first optimization and to the initial cost considered (also shown in Figure 3.4), while the other curves relate to the new costs considered. As expected, as the specific cost of the HG decreases, there is a reduction in LCOH.

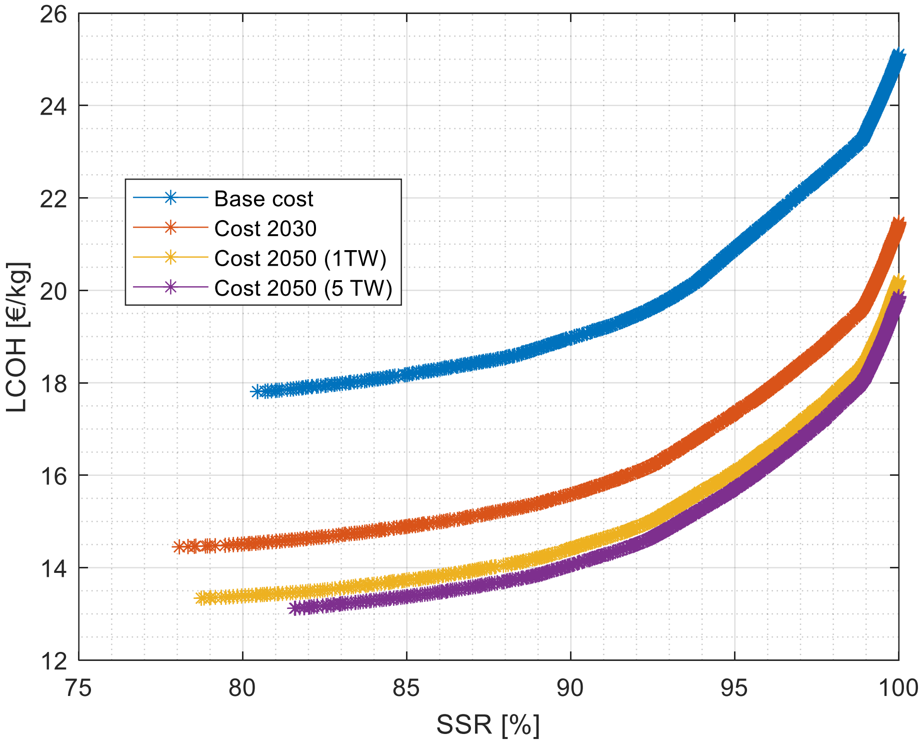

Figure 3.11 - Optimization results by varying the HG specific cost.

Table 3.3 instead reports the main results, including component sizes, for each HG specific cost considered. Considering an SSR of 100% (in bold), the cost decreases from 25.22 €/kg to a minimum of 19.87 €/kg. In general terms, the values found for the component sizes are similar to each other: the PV has a size ranging between 8 353 kW and 8 421 kW, the BS between 312.4 kWh and 403.1 kWh, the HG between 2 909 kW and 2 981 kW, and the LPT between 435.9 kW and 462.2 kW. In the case of SSR-only optimization (bold values), it is expected that the variation in electrolyzer specific cost has no impact, as this parameter does not influence the objective function. However, analysing the opposite extreme (LCOH minimization scenarios in non-bold values), a clear trend emerges as the HG specific cost decreases from 3165.72 €/kW to 353.54 €/kW: the electrolyzer size increases from 1 917 kW to 2 429 kW (+26.7%), while the PV installation decreases from 3 978 kW to 3 568 kW (minimum value). This indicates that when LCOH is the objective, lower electrolyzer costs make it economically favourable to shift the system design toward larger hydrogen generation capacity and reduced photovoltaic oversizing, as the optimizer balances capital costs between the two main components.

Also in this case, the reduction of the LCOH was analysed by considering the sale of surplus electricity produced, limited to the cases of a selling price of 0.0941 €/kWh (regional weighted average, avg F) and 0.137 €/kWh (national average, avg 25). Considering the higher selling price (national average, mean 25), the results show a reduction of €8.45/kg by 2030 and approximately €8.3/kg by 2050 in both scenarios.

Table 3.3 - Optimization results and component sizes by varying the HG specific cost.

c_{HG}	SSR	LCOH	LCOH' avg F	LCOH' avg 25	PV	BS	HG	LPT
[€/kW]	[%]	[€/kg]	[€/kg]	[€/kg]	[kW]	[kWh]	[kW]	[m^3]
3 165.72	80.44	17.81	16.71	16.20	3 978	198	1 917	128.1
	100	**25.11**	**19.35**	**16.72**	**8 398**	**384**	**2 909**	**462.2**
1 191.48	78.06	14.45	13.89	13.63	3 545	191	2 151	131
	100	**21.48**	**15.67**	**13.03**	**8 421**	**312.4**	**2 950**	**459.8**
545.69	78.73	13.34	12.78	12.53	3 568	172	2 332	144.2
	100	**20.21**	**14.50**	**11.89**	**8 369**	**403.1**	**2 981**	**435.9**
353.54	81.58	13.12	12.33	11.96	3 849	183.9	2 429	140.5
	100	**19.87**	**14.17**	**11.57**	**8 353**	**360.1**	**2 974**	**456.8**

3.9 Comparison with the results obtained by Grid Hydrogen Production EMS

The performance obtained for the two proposed EMS are finally compared with the performance achieved considering hydrogen production exclusively with energy purchased form the grid. The compared values refer to the initial specific cost of the HG, as well as the LCOH value is considered without evaluating the sale of electricity to the grid. Since no green hydrogen production is produced in this case, the sole minimization of the LCOH is considered during the optimization process. The LCOH found in this case is 12.94 €/kg, with a HG of 1605 kW and a LPT of 106.5 m^3 (PV and BS are not present). A summary of the results found for each EMS is reported in Table 3.4, considering only the results obtained with the same specific cost of the HG and without considering a revenue for the energy sent to the grid.

In particular, the results obtained for the two objective functions are reported together with the sizing of the main microgrid component and the percentage of hydrogen produced by electricity from the grid. The table also reports the CO_2 emissions per year for the different cases, obtained by multiplying the annual amount of electricity purchased from the public grid with the average emissions factor for electricity production registered in Italy in 2023, equal to 0.413 kg CO_2/kWh [123].

Table 3.4 - Comparison Results between Green, Mixed and Grid EMS (same HG cost).

	SSR	LCOH	PV	BS	HG	LPT	SSR GRID	CO_2
	[%]	[€/kg]	[kW]	[kWh]	[kW]	[m^3]	[%]	[kt/y]
GREEN EMS	80.44	17.81	3 978	198	1 917	128.1	-	0.22
	99.04	23.49	7 420	300.5	2 886	445.4	-	0.29
	100	**25.11**	**8 398**	**384**	**2 909**	**462.2**	-	0.26
MIXED EMS	47.34	13.1	2 088	258.4	1 064	102.7	52.66	9.71
	80.44	15.79	3 778	248	1 889	218.4	19.56	4.01
	90.47	17.82	4 971	325.3	2 112	265.6	9.53	2.23
	100	**23.49**	**7 408**	**529.7**	**2 834**	**430.7**	**-**	**0.51**
GRID EMS	**-**	12.94	-	-	1 605	106.5	100	**16.7**

Considering the results obtained for the microgrid with a SSR equal to 100% (in bold), comparing the results obtained with a Green Hydrogen Production EMS (GREEN EMS) and with a Mixed one (MIXED EMS) the values found for the LCOH and for the components are similar, with a slightly lower LCOH value found for the case of MIXED EMS (23.49 €/kg vs 25.11 €/kg) due to the lower PV, HG and LPT size.

Looking at the results obtained for the lowest LCOH (first row of each case), also in this case the lowest value was found for the MIXED-EMS (13.1 €/kg vs 17.81 €/kg). However, the SSR for the MIXED-EMS is in this case lower than that found for the GREEN-EMS: in fact, while with the GREEN-EMS the SSR is about 80.44% (but the remaining 19.56% is not satisfied), for the MIXED EMS the value decreases up to 47.34%, while the remain HRS demand is satisfied with hydrogen produced by using the public grid (52.66%). Regarding the components size for the MIXED-EMS, excluding the BS these are lower, especially the PV size: this means that the lower cost of purchasing a smaller PV, HG and LPT system outweighs the cost of energy purchased from the grid.

Two other cases were analysed for the MIXED-EMS: one considering the microgrid configuration characterized by a LCOH close to the lowest value found for the GREEN-EMS (17.81 €/kg, in blue) and the other, similarly, considering the most similar lowest SSR (80.44%, in red). For the first case, the SSR is higher that the value found for the GREEN-EMS (90.47% vs 80.44%), due to the larger components size of all the components. Regarding the second case, with a SSR similar between the different EMS, this is characterized by a lower LCOH of the MIXED-EMS (15.79 €/kg vs 17.81 €/kg), due to the lower components size of PV and HG.

Finally, starting from the MIXED-EMS point with the greater LCOH of 23.49 €/kg, the point of the GREEEN-EMS with the same cost was analysed (in green): a SSR of 99.04% was therefore found. Considering the last SSR value found for GREEN-EMS acceptable for HRS, both parity was found in terms of LCOH and total SSR:

however, since the GREEN-EMS is characterized by the absence of CO_2 emissions, this solution is preferable.

As expected, the lowest LCOH is obtained by producing hydrogen directly from electricity purchased from the grid, i.e. 12.94 €/kg. In this case, the hydrogen generator is not limited by the capacity factor of the PV system and it can operate continuously, resulting in a downsizing of this component thanks to its greater utilization factor and a strong reduction of the hydrogen storage capacity required. However, as expected, this case is also characterized by higher emissions, 16.7 kt CO_2/y. Compared to the previously reported emissions of diesel buses, 36.84 kt CO_2/y, this means that replacing 21 diesel buses with hydrogen ones leads to a reduction of 20.14 kt CO_2/year (54.7%), despite the hydrogen is produced only from the grid. The percentage of emissions reduction increases to 73.6% with the lowest Green SSR in the Mixed EMS case, while with the highest Green SSR the reduction reaches 98.6%. The Green EMS case, on the other hand, is characterized by an average emissions reduction of 99.3%, considering all the cases reported. It should be noted that the residual emissions in the Green EMS are attributable to the use of grid electricity to meet the HRS's demand when renewable generation is insufficient.

A particular note must be made on the costs obtained. These, in fact, are higher than those commonly found in the literature: [124] reports a LCOH close to 8 €/kg for hydrogen production by PV and grid with a PEM HG, while [125] reports a LCOH between 3.5 €/kg ÷ 10.4 €/kg for hydrogen production from PV. However, some important aspects of the case study analysed should be underlined: the renewable-based microgrid is exclusively used for the HRS, thus the PV energy production is limited by the current HG demand. Furthermore, the cost is strongly influenced by the hydrogen production rate, which amounts to approximately 100 t/year. This relatively low annual output results in a limited utilization factor of the HG (2 919 h/y for the Green EMS, 3 009 h/y for the Mixed EMS and 3382 h/y for the Grid EMS considering a 100% SSR), which amplifies the impact of the initial investment on the overall cost.

A final analysis of the results concerns the comparison between the LCOH obtained by producing hydrogen exclusively from the public grid (12.94 €/kg, Table 3.4) and the corrected LCOH′ calculated considering the sale of surplus renewable electricity at the highest price (avg 25, Table 3.3). The results suggest that, under the cost scenarios expected for 2030 and 2050, hydrogen production based solely on renewable sources could become economically comparable to, or even more advantageous than, production based on grid electricity. Specifically, in 2030 the production cost is nearly equivalent (13.03 €/kg versus 12.94 €/kg from the grid), while in 2050 it decreases to 11.87 €/kg or 11.57 €/kg. This reduction is mainly attributable to the projected decrease in the specific investment cost of the electrolyzer and to the additional revenue derived from selling surplus renewable electricity. However, it should be emphasized that this projected cost reduction is based on the current national average electricity selling price for the first quarter of 2025. Therefore, the actual extent of the cost decrease will depend also on the future evolution of electricity market prices.

3.10 Results summary and conclusions

This chapter introduced the integration of the HRS studied in Chapter 2 into a renewable energy-based microgrid. A mathematical model was developed in Matlab to evaluate the microgrid performance under different Energy Management Strategies (EMS), each characterized by an increasing share of green hydrogen production. Three EMS were investigated: Green EMS, characterized by hydrogen production exclusively from renewable sources; Mixed EMS, which combines renewable and grid-based production; and Grid EMS, with hydrogen produced solely from the grid.

Each EMS was optimized to determine the optimal component sizing for two objective functions: maximizing the SSR and minimizing the LCOH. Initial results showed that, for 100% SSR, the Green EMS exhibited higher costs at 25.11 €/kg compared to 23.49 €/kg for the Mixed EMS.

These costs were significantly reduced when accounting for surplus electricity sales to the grid: considering the higher selling price (0.137 €/kWh), costs decreased to 16.72 €/kg (Green EMS) and 16.98 €/kg (Mixed EMS). For the Green EMS, a parametric analysis was conducted varying the specific HG cost, with projections to 2030 and 2050. Results showed a cost reduction to 11.57 €/kg by 2050, assuming current electricity selling prices remain stable.

PV systems dominate TCI at 46.5-36.8% for minimum LCOH scenarios, rising to 55.9-52.9% at 100% SSR as total investments increase by 75.8% (Green EMS) and 147% (Mixed EMS) due to oversized renewable capacity requirements.

Grid EMS showed production costs of approximately 13 €/kg considering the current specific HG cost. This indicates that by 2050, renewable-based hydrogen production could become more cost-competitive than grid-based production, provided that HG cost projections are met and selling prices remain relatively stable. Nowadays, however, an additional cost of approximately 3.8 €/kg must be considered for production from renewable sources, compared to that of production from the grid alone (higher energy sales price).

Regarding CO_2 emissions, the current fleet of 21 diesel buses is responsible for 36.84 kt CO_2/y. With hydrogen-powered vehicles, the Green EMS generates minimal emissions, limited to grid electricity used for HRS components when renewable sources are insufficient. Higher emissions were observed for the Mixed EMS (up to 9.71 kt CO_2/y) and the Grid EMS, characterized by 16.7 kt CO_2/y. This means that even with grid-only hydrogen production, FCEV adoption would reduce emissions by 54.7%, while the Green EMS would achieve a 99.3% reduction.

The next chapter will explore a different investigation, featuring a Hydrogen Storage System (HSS) for Heavy-Duty Vehicles operating at 70 MPa, from the dispenser to the onboard tanks.

4. Thermodynamic Modelling and Sensitivity Analysis of a 70 MPa Hydrogen Storage System for Heavy Duty Vehicles

While the previous chapters focused on the integration of a 35 MPa HRS within a renewable energy microgrid, this chapter shifts attention to a more detailed analysis of the hydrogen storage system itself. Specifically, this chapter examines a 70 MPa Hydrogen Storage System (HSS) for heavy-duty vehicles, encompassing the entire storage chain from the dispenser to the onboard tanks. The choice of 70 MPa pressure is driven by the desire to study storage of up to 100 kg of hydrogen in heavy-duty applications: given the space constraints typical of these vehicles, achieving such storage capacity at 35 MPa would not be feasible due to volume limitations.

A customizable and dynamic model in Matlab-Simulink that simulates both the vehicle storage system and the refueling infrastructure (dispenser) is proposed. The main objectives are threefold: first, to provide a customizable toolkit that reduces project development time, enables optimal sizing decisions (e.g., tank type and configuration), and ensures full, rapid, and safe refueling through a comprehensive dynamic model; second, to investigate the thermodynamic behaviour in all hydrogen tanks to identify the shortest refueling time (or highest mass flow rate) for heavy-duty vehicles storing up to 100 kg of hydrogen at 70 MPa, while maintaining compliance with SAE J2601-5 pressure and temperature limits; third, to compare results obtained by varying characteristic parameters of different HSS components (APRR, dispenser and ambient temperature, pipe length, and component diameter) to determine the optimal layout solution among different tank types (III to V) and configurations (5 to 7 tanks).

Since one of the key objectives is to identify the shortest possible refueling times for heavy-duty applications, the MCF-HF-G protocol at 70 MPa is adopted to evaluate whether a 300 g/s flow rate can successfully refuel different vehicle configurations while respecting temperature and pressure constraints. This scenario should be understood as a forward-looking benchmark, representative of potential system capabilities rather than existing commercial infrastructure and provides valuable insights into the development of next-generation hydrogen refueling systems for heavy-duty transportation.

4.1 Definition of different tanks and layouts

A first layout of a HSS for a generic heavy-duty vehicle has been considered. This configuration was developed starting from the technical specifications of a typical truck chassis, with the goal of maximizing the amount of hydrogen stored while adapting to the available space on board. In particular, the placement and number of tanks were defined to make the best use of the space behind the cabin and between the rear wheels, resulting in a total of 6 identical tanks: 4 positioned behind the cabin and 2 between the wheels. Figure 4.1 shows the simplified 6 tanks layout with all the components (pipes, elbows and T-pieces) in their indicative positions, while Figure 4.2 shows the already implemented scheme in the Matlab-Simulink model environment. For simplicity, in Figure 4.1 only the filling pipe was represented, while other infrastructure components such as the filling receptacle, fuelling nozzle, and dispenser were omitted. In Figure 4.2, the Dispenser section includes the dispenser, the filling hose, the fuelling nozzle, the filling receptacle and a pipe connected to the first T-piece. The latter is connected to the Tank Left Wheels space, TLW, while the second T-piece is connected to the Tank Right Wheels space, TRW, and to the block that includes all the Tanks Behind Cabin, TBC. All tanks are positioned at the end of a line consisting of pipes, elbows and T-pieces. These tanks are characterized by the same geometrical and material properties and are therefore able to store the same quantity of high-pressure hydrogen: 16.43 kg each, for a total of 98.58 kg at the Nominal Working Pressure (NWP) of 70 MPa. This value was chosen to closely match that reported in [126], as it represents the storage capacity currently regarded as necessary to achieve parity with conventional diesel trucks in terms of driving range and refueling time, while also addressing the requirements identified by manufacturers and engineers in the heavy-duty transport sector.

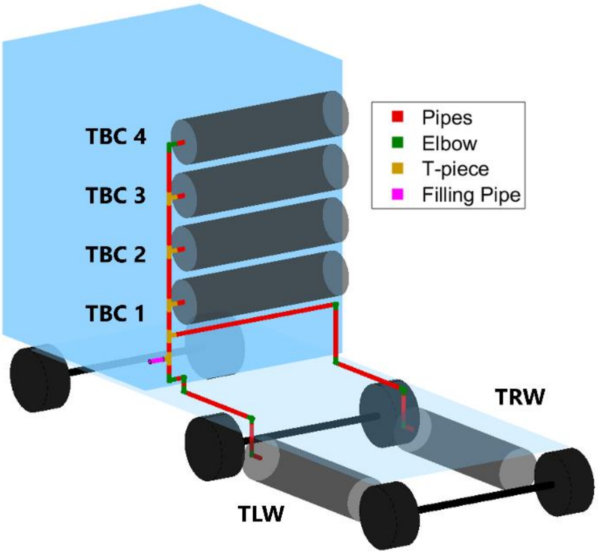

Figure 4.1 - Simplified scheme of the 6 tanks layout with all the components.

With the aim of investigating a possible advantage regarding the refueling time, evaluating different packaging configurations and analysing how splitting the hydrogen flow across a different number of tanks affects pressure and temperature variations, two other layouts were considered: one with a total of 5 tanks and one with a total of 7 tanks. In these layouts, the tanks between the wheels space are kept equal in number (2) and dimensions to the ones considered in the layout with 6 tanks (TLW and TRW), while the number of tanks behind the cabin changes to 3 and 5 tanks, respectively. Also, removing a tank means removing 2 pipes and 1 T-piece, while adding a tank means inserting the same number of components. For a better comparison between the layouts, the same total amount of hydrogen was stored in each configuration. Therefore, the geometry of the tanks behind the cabin had to be adapted accordingly. Since the tank length was kept constant across all layouts due to space constraints, the tank diameter was either increased (in the 3 TBC layout) or decreased (in the 5 TBC layout), as reported in Table 4.1. In this way, in all layouts the maximum quantity of hydrogen storable is close to 98.5 kg. Furthermore, as the diameter of the tank changes, the wall thickness must be adjusted accordingly. The new values were estimated using the Barlow formula (Equation (29)) [127], where t is the wall thickness, D_{inner} is the inner diameter of the tank considered and σ is the allowable stress, by preserving the ratio between diameter and wall thickness (D_{inner}/t) of the original reference tank. In this way, the calculated stress remains consistent across different diameters, avoiding the need to assume a specific material strength value.

$$t = \frac{NWP \cdot D_{inner}}{2 \cdot \sigma} \tag{29}$$

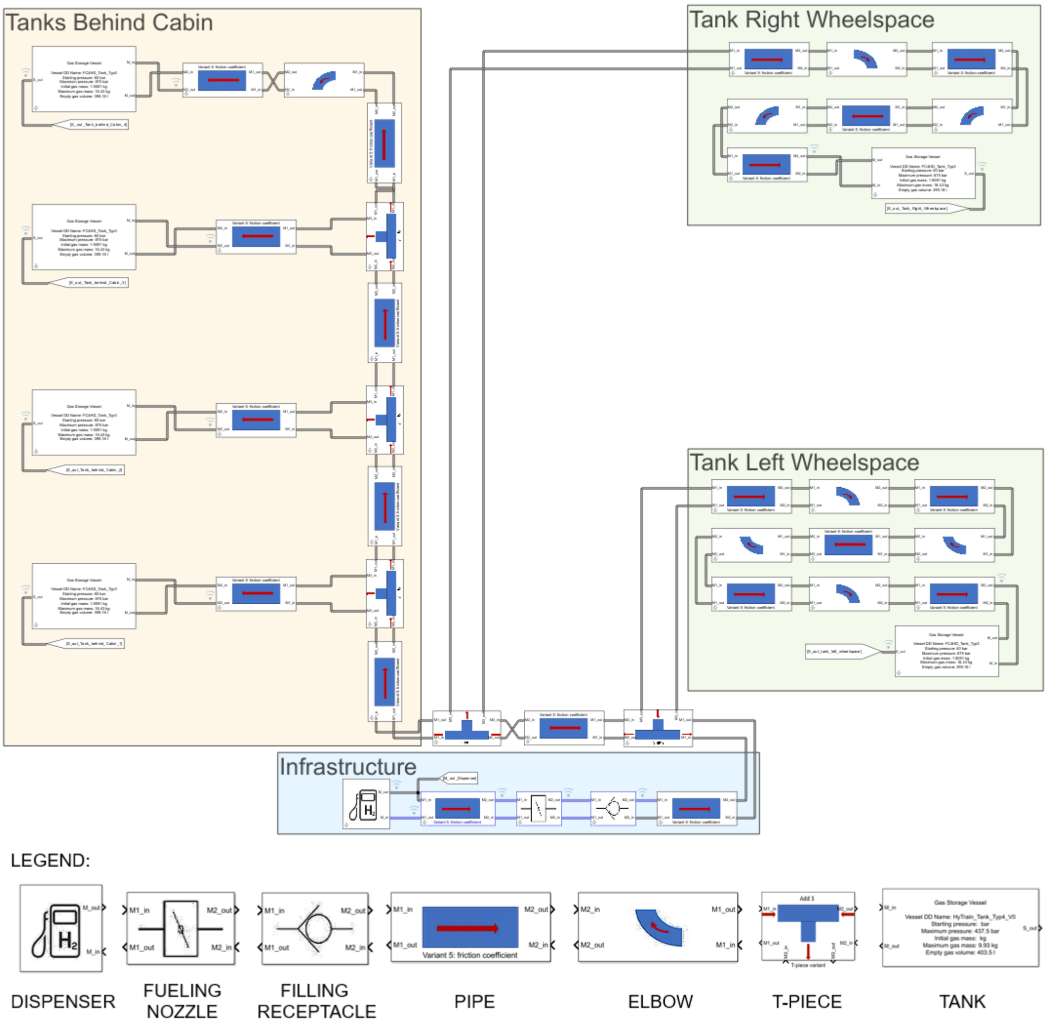

Figure 4.2 - Layout with 6 tanks implemented in Matlab-Simulink environment.

Table 4.1 - Geometric properties for the tanks considered.

		TLW TRW	3 TBC (5 Tanks)	4 TBC (6 Tanks)	5 TBC (7 Tanks)
Injector d	**[m]**	0.0054			
Inner Length	**[m]**	2.033	2.033	2.033	2.033
Inner Diameter	**[m]**	0.5	0.577	0.5	0.447
Wall thickness	**[m]**	0.023	0.0236	0.023	0.018
Initial gas mass	**[kg]**	1.85	2.47	1.85	1.48
Max. gas mass	**[kg]**	16.43	21.88	16.43	13.13
Empty gas volume	**[l]**	399.18	531.59	399.18	319.04

In this study, Type III to V tanks are considered, whose characteristics relating to material properties and their geometry are reported in Table 4.2 and Table 4.1, respectively. Specifically, the values reported in Table 3.1 are based on preliminary data from ongoing internal activities at HyCentA. The tanks were modelled using the approach presented in [128]. Regarding the material properties, the characteristics of the composite material were assumed identical for all tank types, while the liner material differs for type III (aluminium) and type IV (plastic) tanks. For type V, the latter is considered with the same properties as the composite layer: in fact, as already mentioned, type V tanks are characterized by a single composite layer. Concerning the tank geometry, as mentioned above, the tanks between the wheel space (TLW and TRW) always have identical dimension, while the tanks behind the cabin vary depending on the layout.

Table 4.2 - Characteristics and material properties for the tanks considered.

Common values for all tank types					
	Nominal Working Pressure (NWP)	**[MPa]**	70		
	Reynolds coefficient (*a*) / exponent (*b*)	**[-]**	0.04 / 0.67		
	Raileigh coefficient (*c*) / exponent (*d*)	**[-]**	0.01 / 0.352		
	Alpha outer (α_{out})	**[W/m^{2}K]**	10		
	A contact	**[m^2]**	0.05		
Boss	**Specific heat**	**[J/kgK]**	500		
	Density	**[kg/m^3]**	7 850		
	Lambda	**[W/mK]**	15		
	Mass	**[kg]**	3.9		
Material Properties for each tank type					
			Type III	**Type IV**	**Type V**
Composite	**Specific heat**	**[J/kgK]**	1 102	1 102	1 102
	Density	**[kg/m^3]**	1 560	1 560	1 560
	Lambda (λ)	**[W/mK]**	0.43	0.43	0.43
Liner	**Specific heat**	**[J/kgK]**	888	2 800	1 102
	Density	**[kg/m^3]**	2 700	1 047	1 560
	Lambda (λ)	**[W/mK]**	220	0.3	0.43

To calculate the Nusselt number, Nu [128], also related to the heat transfer coefficient α between the hydrogen gas and inner tank wall as indicated in Equation (2), the Reynolds and Rayleigh numbers were considered, while α_{out} in Table 4.2 indicates the heat transfer coefficient between the tank wall and external environment.

$$Nu = a \cdot Re^{b} + c \cdot Ra^{d} = \frac{\alpha \cdot D}{\lambda} \tag{2}$$

Where D is the diameter, since the tanks are horizontal, and λ is the thermal conductivity. In particular, Reynolds and Rayleigh exponents and coefficients are based on experimental data [128]. Regarding the empty gas volume of the tank, this was calculated considering the tank as a cylinder with the inner length and diameter indicated in Table 4.1.

4.2 Simulation settings and logic

The simulation model used in this study is based on the model implemented by [128]. In particular, the components considered were implement in a model library, which consists of a dispenser boundary condition, pipes, elbows, T-pieces, expansions/reductions, check valves, regulator valves, generic pressure loss components and storage tanks. Each component, modelled as a block, is connected to adjacent components via signal buses, and communicates its mass flow rate, pressure, temperature, and flow resistance with adjacent upstream and downstream components. These components were used to model the different layouts described above, from the dispenser to all on-board storage tanks.

No experimental data were available for direct validation of the model. Therefore, the boundary conditions and simulation setup were based on those reported in the reference study [128]. The hydrogen gas was modelled as a real gas, with temperature- and pressure-dependent thermophysical properties. The VT was initialized at a fixed pressure, while the internal pressure evolved dynamically during the filling process, depending on the APRR, which was set as initial and constant input. The final target pressure was set to the nominal full-fill value of 70 MPa. Although inlet boundary conditions, such as supply pressure, APRR and supply temperature were prescribed, the simulation was conducted in transient mode, allowing the internal state of the tank to respond dynamically to gas compression and heat generation. These modelling choices ensure physical realism while maintaining consistency with previous literature.

In order to compare the results in terms of refueling time, final pressure, mean tank temperature, maximum mass flow from the dispenser and pressure losses (this latter only for the tank characterized by the highest value), some input parameters were kept constant, while others were changed within a range, as reported in Table 4.3.

The parameters kept constant are the NWP, the safety margin for the temperature limit and the initial pressure inside all tanks, assumed at the beginning of the refueling with a State of Charge (SOC) lower than 10 % to study a nearly complete refueling process. The NWP was set to 70 MPa, as this value allows storing approximately 100 kg of hydrogen in the available onboard space in the heavy-duty vehicle considered. A safety margin of 5 °C limit was adopted in compliance with SAE J2601-5 [60].

Table 4.3 - Constant and changing input parameters for the simulation.

Parameter		Value	
Nominal Working Pressure	[MPa]	70	
Safety margin for Temperature limit	[°C]	5	
Initial Pressure for all Tanks	[MPa]	6	
Average pressure Ramp Rate	[MPa/min]	8 : 0.2 : 9.2	
Cold fill Dispenser Temperature	[°C]	-40 °C :10 :0 °C	
Ambient Temperature	[°C]	-20 °C :10 :40 °C	
Length changing in percentage	[%]	11.758 m (5 tanks) 12.497 m (6 tanks) 12.912 m (7 tanks)	-20 % :10 :10 %
Diameter changing in percentage	[%]	3/6/8 mm (all layouts)	0 % :10 :50 %
Tank Type		III – IV – V	
Total number of Tanks		5 – 6 – 7	

According to SAE J2601-5 protocol (MCF-HF-G), the dispenser temperature was varied between -40 °C and 0 °C, since these are the limits present in the protocol. While the temperature of -40 °C is technically achievable using active pre-cooling technologies, it may not always be maintained under real-world conditions, especially at high station throughput or in warmer climates. Therefore, the assumption of −40 °C represents an idealized condition that enables performance benchmarking under optimal thermal management. The results obtained under this assumption should be interpreted as best-case estimates, with practical deviations expected in real-world applications.

The APRR values were selected based on multiple simulation runs aimed at minimizing the refueling time while still complying with the pressure and temperature constraints imposed by SAE J2601-5 protocol. The lower limit of 8 MPa/min was set because lower values resulted in disproportionately longer refueling times without improving temperature or pressure performance. For this reason, such cases were not considered relevant to the objective of this study.

Regarding the pipe network, pipe length variations reflect differences among the three tank layouts considered (5, 6, and 7 tanks), with total lengths computed as the sum of all pipe sections per configuration. These values are reported in Table 4.3 and ordered by increasing total length. The pipe diameters, on the other hand, are constant across configurations and vary only along the flow path: the largest diameter (8 mm) is assigned to the dispenser line to accommodate the higher mass flow, 6 mm to the TLW line, and the smallest diameter (3 mm) to the TRW and TBC lines at the periphery. The variation percentages shown in Table 4.3 apply uniformly across all pipe segments (3, 6, and 8 mm). It is important to note that both length and diameter values should be considered as minimum design estimates, based on the physical constraints of vehicle packaging and with the aim of reducing pressure losses. Any simulated reduction below these values is to be interpreted as a theoretical sensitivity analysis to evaluate the effects on refueling performance. The variation in tank number affects not only the pipe layout but also the overall space, weight, and safety profile of the storage system. A 5-tank configuration typically involves larger-diameter tanks, which may be more difficult to integrate into constrained vehicle spaces. In contrast, 6- or 7-tank layouts allow for more modular placement but increase the complexity of piping and mounting. Additionally, larger tanks or a greater number of tanks increase total hydrogen mass and stored energy, with implications for safety and structural integration that merit future investigation.

Finally, to identify the acceptable range of input parameters that allow full refueling within the SAE J2601-5 limits for pressure and temperature, the model is set to stop only when a SOC of 100 % is reached in all tanks.

To systematically identify the optimal combination of input parameters that ensures full refueling within the SAE J2601-5 limits, an iterative procedure was implemented as illustrated in Figure 4.3. For each tank type have been performed successive refueling simulations by varying one input at a time within the defined range (Table 4.3), while keeping the others constant. After each simulation, the resulting final pressure and temperature in all tanks are checked against the SAE limits. Only simulations that result in 100 % SOC across all tanks and remain within these limits are considered valid. The process continues until all feasible input combinations have been tested, enabling the identification of the best-case scenario, or the one yielding the minimum refueling time (or maximum mass flowrate) while respecting the pressure and the temperature limits. The choice to vary one parameter at a time was made to isolate its individual impact and represent the results as a function of the percentage change of each input. This approach allows a simple interpretation of how each parameter individually affects the system outputs, facilitating a direct comparison between scenarios. However, this method does not consider potential interactions between parameters, which could lead to trade-offs or combined effects not captured by the variation of a single parameter.

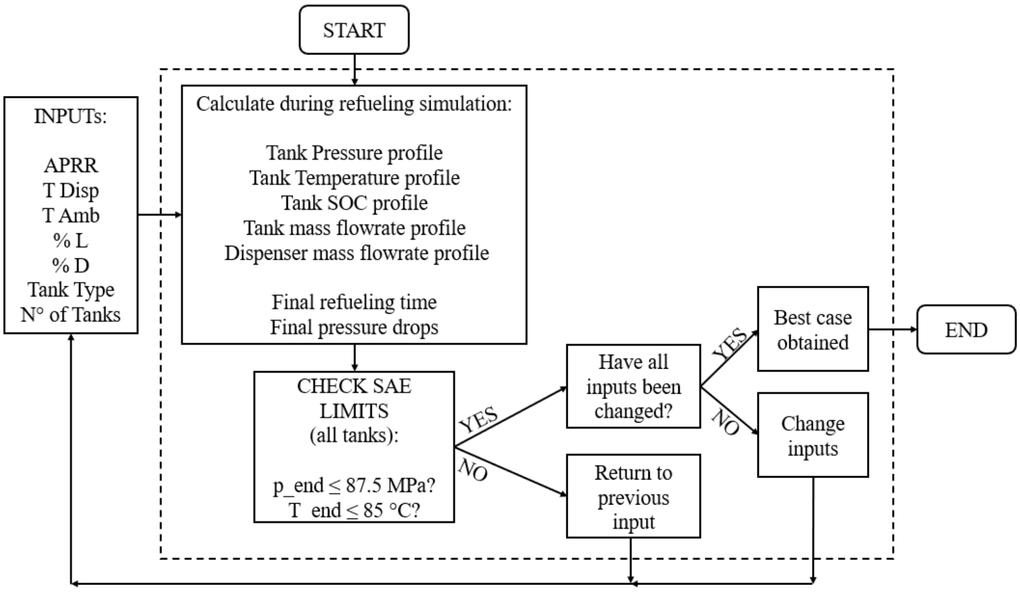

Figure 4.3 - Methodology used to identify the best case for each tank type.

4.3 Results of the thermodynamic modelling

This section presents the results obtained from the simulation of the vehicle refueling process, starting with the layout with 6 tanks. Subsequently, the results obtained by varying the inputs (e.g. APRR, dispenser and ambient temperature, length and diameter dimensions, tank type and layout) are described.

Several simulations were carried out to identify the input parameters that ensured the highest APRR, and consequently the highest mass flow rate delivered by the dispenser and the shortest refueling time, while complying with the SAE limits for pressure and temperature. The main input assumed and results obtained for all tank types are summarized in Table 4.4, while the trends of pressure, temperature, SOC, and hydrogen mass flow rate are shown in Figure 4.4. In particular, these results were taken as the base case for the parametric analyses reported below, since they are the points that guarantee the lowest refueling time when varying the tank type, while ensuring all SAE limits.

Table 4.4 - Input and principal results – layout with 6 tanks.

		Type III	**Type IV**	**Type V**
INPUT				
APRR	[MPa/min]	9	8.8	8.6
Dispenser T	[°C]	- 40 °C	- 40 °C	- 40 °C
Ambient T	[°C]	20 °C	20 °C	20 °C
Length	[m]	10	10	10
Diameter	[mm]	3.6 / 7.2 / 9.6	3.6 / 7.2 / 9.6	3.6 / 7.2 / 9.6
RESULTS				
Max. pressure	[MPa]	87.25	87.48	87.16
Max. temperature	[°C]	70.69	73.27	73.44
Max. dispenser mass flow rate	[g/s]	216.11	210.94	206.21
Refueling time	[min]	10.38	10.52	10.64
TOT Pressure Drops – Max MF	[MPa]	25.96	25.14	24.54
TOT Pressure Drops – End	[MPa]	16.27	14.88	13.70

The only input parameter that varies with the type of tank is the APRR, while the other parameters were kept constant. Specifically, the APRR decreases with the tank type in order to ensure compliance with SAE pressure and temperature limits. This effect is related to the different thermal insulation properties of the tank materials, which influence the heat transfer during refueling. As a result, certain tank types experience higher temperature increases when filled at the same rate. The dispenser temperature was set equal to the lowest value specified by the standard, while the ambient temperature was assumed to be 20 °C. Pipe lengths and component diameters were decreased and increased by 20 %, respectively, compared to the minimum values reported in Table 4.3.

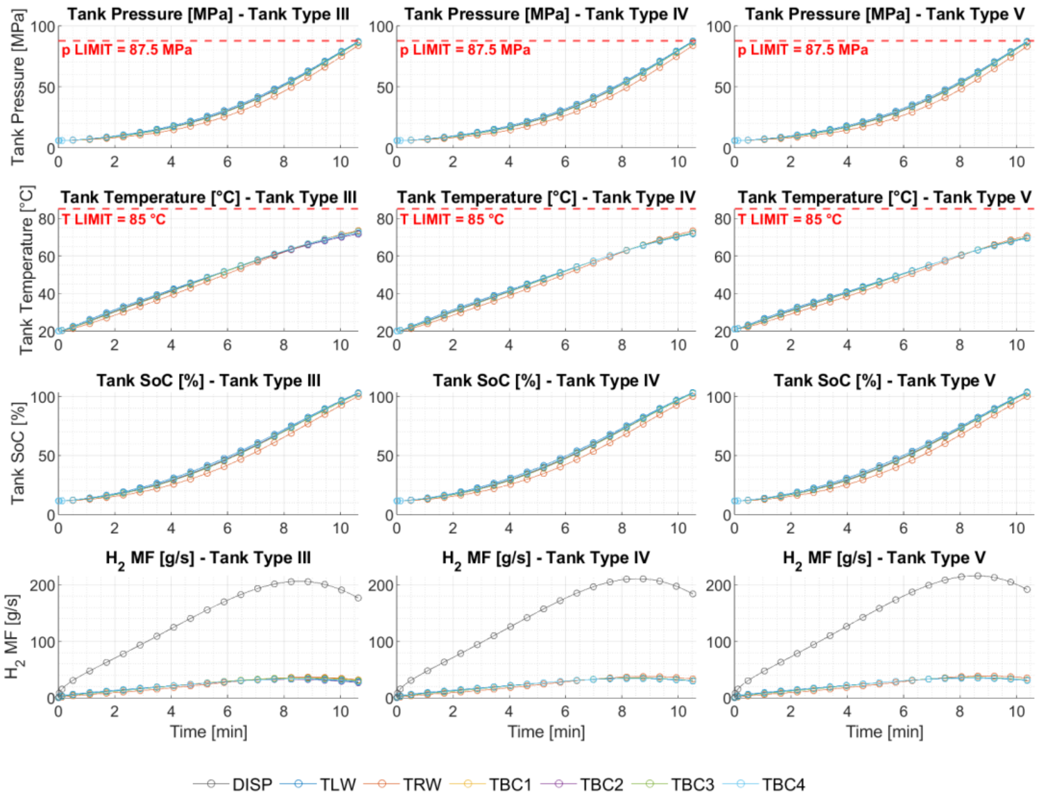

Figure 4.4 - Pressure, temperature, SOC and mass flow rate during the refueling of 6 tanks layout (all tank types).

The results show refueling times of 10.38 min (Type III tanks), 10.52 min (Type IV tanks), and 10.64 min (Type V tanks). As expected from the initially assigned APRR values, the refueling time increases slightly. Pressure values (slightly above 87 MPa) and temperature values (ranging from 70.7 to 73.44 °C) comply with SAE limits as required. The peak hydrogen mass flow rate from the dispenser decreases from 216.11 g/s to 206.21 g/s, in line with the reduction of APRR. However, in order to respect pressure and temperature constraints, this value remains below the 300 g/s limit specified by the SAE standard and by [126], which is considered ambitious and difficult to achieve with current refueling hardware (e.g., hoses, valves, nozzles). Finally, the total pressure drops were calculated both at the end of the refueling and at the point where the pressure drops reach their maximum value, corresponding to the point where the inlet mass flow rate in each tank is at its peak. As expected, the pressure drops decrease when moving from Type III to Type V tanks, due to their different thermal and mechanical characteristics, with higher pressure drops occurring at peak flow. The final pressure inside each tank was determined by subtracting the pressure drop (calculated at the end of the refueling) from the pressure measured at the dispenser outlet. This accounts for line losses and reflects the actual pressure experienced by the tank.

With regard to the graphical trends shown in Figure 4.4, these are similar across all tank types and individual tanks, with the TRW tank showing slight deviations in the pressure and SOC plots, as well as in the early stages of the temperature curve.

Moreover, as previously mentioned, the model stops once a 100 % SOC is reached in each tank.

4.5 Results of the sensitivity analysis

To assess the influence of input parameter variations on system performance, a sensitivity analysis was conducted. Starting from the input values defined for each tank type (as shown in Table 4.4), these parameters were subsequently varied as previously described in Table 4.3. The resulting influence on the main output parameters (refueling time, maximum pressure, mean temperature, maximum dispenser mass flow rate, and pressure drop) is presented below, considering all tank types and the 6 tanks layout as the baseline configuration. It is important to clarify the values chosen for pipe lengths and diameters. As shown in Table 4.4, the baseline values differ from the minimum values reported in Table 4.3. This is because, after several simulations, shorter refueling times were observed for reduced pipe lengths and increased diameters, as will be discussed in detail later. Therefore, the baseline length was set to approximately 10 m, while the baseline diameters to 3.6, 7.2, and 9.6 mm for the respective lines. Based on these, pipe lengths were varied between 10 m and 13.75 m, while component diameters were varied from 3 mm to 4.5 mm, from 6 mm to 9 mm and from 8 mm to 12 mm for the line furthest, in the middle and closest to the dispenser respectively.

4.5.1 Influence on the refueling time by varying the input parameters

The trends of the refueling time results for each tank type are shown in Figure 4.5. The results show better performance compared to the baseline was obtained for lower ambient temperatures than the initial value (20 °C), for higher APRR values (although these do not comply with the maximum pressure limits, as will be discussed later), and for larger component diameters. The lowest refueling times (excluding those achieved with increased APRR) are 10.11 min, 10.27 min, and 10.4 min, respectively. Variations in the other parameters, on the other hand, lead to an increase in refueling time. This is particularly evident with higher dispenser temperatures (which reduce the temperature gradient between the incoming hydrogen and the tank wall, which weakens the convective heat transfer and limits the allowable refueling rate imposed by thermal constraints), longer pipe lengths (which increase pressure losses along the flow path due to greater frictional resistance, which reduces the effective pressure at the nozzle and thus limits the mass flow rate during refueling), lower APRR values (which directly limit the allowable mass flow rate) and smaller component diameters (which introduce higher flow resistance due to reduced cross-sectional area, which increases fluid velocity and pressure drop, ultimately decreasing the refueling rate). The maximum refueling time recorded is 11.33 min for the Type V tank. Interestingly, the variation in the number of tanks does not have a significant impact on the overall refueling time. This suggests that, under the simulation conditions, the refueling system is not substantially affected by how the total storage volume is distributed among multiple tanks. This result may be attributed to the fact that the flow is regulated primarily by upstream parameters (such as pressure, temperature, and component dimensions) rather than the number of parallel storage tank behind the cabin. Although the number of tanks does not significantly affect refueling time, a slight increase is observed when moving from Type III to Type V tanks. This trend can be attributed to the thermal properties of the liner materials. Type III tanks incorporate an aluminium liner with high thermal conductivity (220 W/mK), which promotes rapid heat dissipation during refueling. In contrast, Type IV tanks use a polymer liner with lower conductivity (0.3 W/mK), and Type V tanks are liner less, relying solely on the composite material. As a result, the reduced ability to dissipate heat in Types IV and V leads to slower allowable refueling rates, and thus slightly longer refueling times. Overall, the trends in the results appear to be nearly linear and consistent across the different tank types. Finally, the fact that the refueling time does not increase significantly when the type of tank varies is due to the fact that the parameters have been varied to a limited extent, especially as regards the APRR. For APRR values, values higher than those reported were not considered in the results. These, in fact, were excluded as they led to a final pressure higher than the limit imposed by the SAE protocol during the refueling simulations. Furthermore, the fact that the variation is small implies that with the variation of only one parameter at a time, the only one that influences the final refueling time is the APRR, while all the other parameters have a negligible effect.

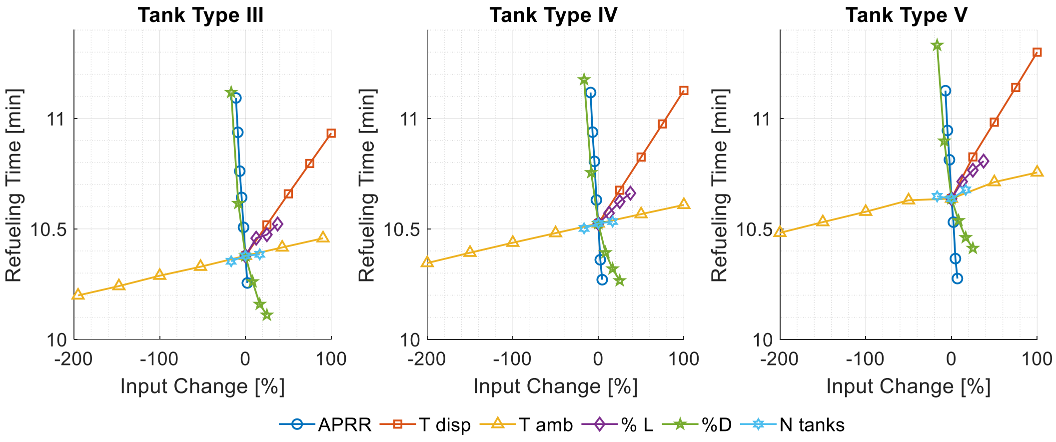

Figure 4.5 - Influence on the refueling time by changing the inputs (all tank types, 6 tanks layout).

4.5.2 Influence on the final pressure by varying the input parameters

This section presents the influence of input variations on the final pressure results. The results (Figure 4.6) are shown with reference to the tank that first reaches 100 % SOC, namely the TLW, which is characterized by the shortest pipe length. As illustrated in the figure, all values above the red dashed line must be excluded, as they do not comply with the SAE pressure limit of 87.5 MPa. In particular, conditions with higher ambient and dispenser temperatures, smaller diameters, and longer pipe lengths must be excluded. Therefore, lower ambient temperatures, larger diameters, and lower APRR values are preferable, although the latter lead to an increase in refueling time. As in previous cases, the results obtained from the variation of individual input parameters show an almost linear behaviour and are consistent across the different tank types. Additionally, the variation in the total number of tanks has only a marginal effect on the final pressure outcome.

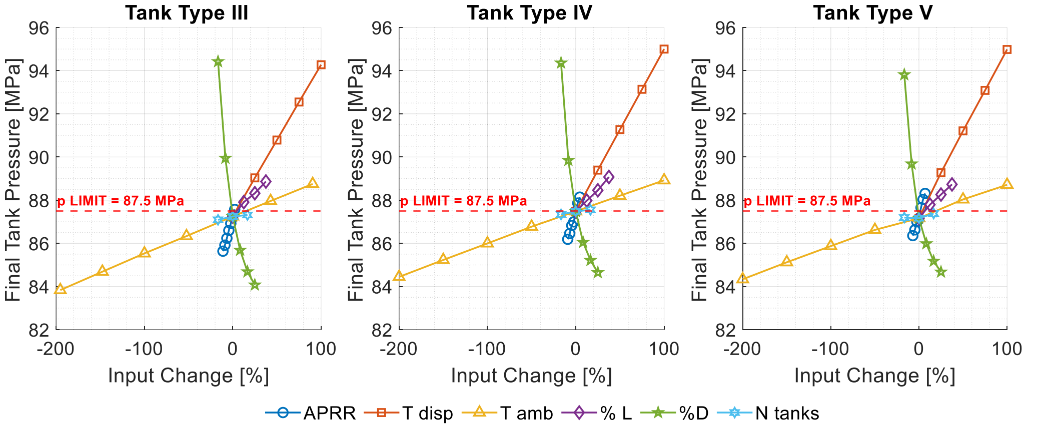

Figure 4.6. - Influence on the final pressure by changing the inputs (all tank types, 6 tanks layout).

4.5.3 Influence on the mean tank temperature by varying the input parameters

Figure 4.7 shows the results regarding the influence of input parameters on the average temperature inside the tanks during the refueling. As expected, the parameters that most significantly affect this outcome are the dispenser and ambient temperatures. A decrease in ambient temperature leads to a reduction in the average tank temperature, as the initial thermal conditions enhance the heat absorption capacity of the system. Conversely, increasing the dispenser and ambient temperatures result in higher the average tank temperatures, with the dispenser temperature having a more pronounced effect due to its direct role in determining the enthalpy of the incoming gas. This behaviour is consistent with findings previously reported in the literature, which have demonstrated a linear correlation between ambient temperature and gas temperature rise during fast filling processes [129].

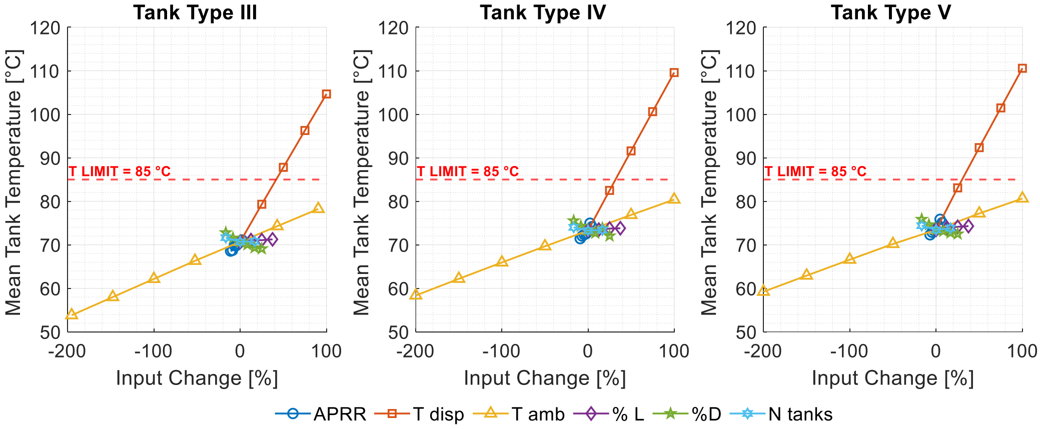

Figure 4.7 - Influence on the mean tank temperature by changing the inputs (all tank types, 6 tanks layout).

Furthermore, as indicated by the red dashed line, the SAE temperature limit of 85 °C is exceeded for dispenser temperature values ranging approximately from -

20 °C (Type III tanks) to just above -30 °C (Type V tanks). Also in this case, the variation in results shows an approximately linear trend and remains consistent across different tank types.

4.5.4 Influence on the maximum dispenser mass flow rate by varying the input parameters

With regard to the influence on the maximum mass flow rate delivered by the dispenser, the results are shown in Figure 4.8. The maximum flow rate increases for ambient temperatures lower than the base value, with increasing APRR (which, however, leads to pressures that exceed the SAE limit), and with larger component diameters, as well as when using the 7 tanks layout. Conversely, higher dispenser temperatures and lower APRR values result in a noticeable decrease in the maximum dispenser mass flow rate. In general, the results show a decreasing trend with the transition from Type III to Type V tanks. This behaviour is primarily due to the lower thermal conductivity and reduced heat capacity of Type V tanks, which lead to a faster internal temperature rise during refueling, thereby triggering earlier flow limitations to avoid surpassing safety thresholds. This trend is significant, as it highlights how tank material properties can directly influence refueling performance and system design. Almost all trends maintain an approximately linear and consistent behaviour across the different tank types. Although the trend observed for the variation of diameter appears approximately linear within the analysed range, it is likely of higher-order polynomial nature, as suggested by the curvature visible at the upper end of the range. This apparent linearity is a consequence of the limited number of data points considered, constrained by practical design limitations that restrict the feasibility of further increasing the pipe diameter.

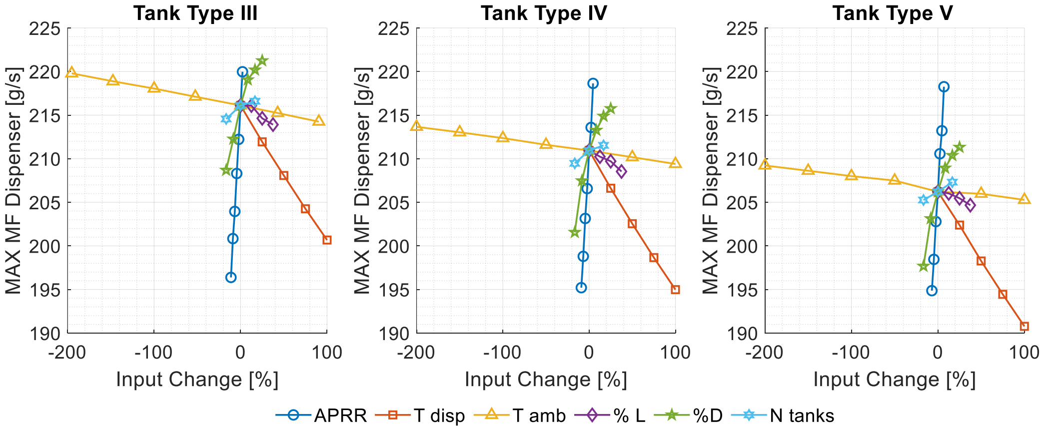

Figure 4.8 - Influence on the maximum dispenser mass flow rate by changing the inputs (all tank types, 6 tanks layout).

4.5.5 Influence on the pressure drops by varying the input parameters

The last influence analysed concerns the results of the total pressure losses. As previously mentioned, the total pressure drops were calculated both at the end of refueling and when the inlet mass flow rate to each tank reaches its peak (approximately between minutes 8 and 10, as shown in Figure 4.4). Figure 4.9

shows an example of the pressure drops calculation for tank TRW, Type III in the 6 tanks layout (the input data used in the model were reported in Table 4.3). The TRW tank was selected because it is characterized by the highest pressure drops, being positioned at the end of the longest line in the refueling piping layout. This approach was consistently applied to evaluate pressure drops for all tanks in the system. The figure also includes the results for the tank with the lowest pressure drops, TLW. Specifically, the left side of the figure shows the pressure drops at the end of refueling, while the right side presents the pressure drops corresponding to the point of maximum inlet flow rate to the tank. Furthermore, the tank indicated in the legend refers to the results obtained for the same tank, distinguishing between pressures and pressure drops of the components reported on the x-axis. When the results obtained are different depending on the tank, these can be easily identified by following the reference colours (blue - red for the TRW and green - yellow for the TLW).

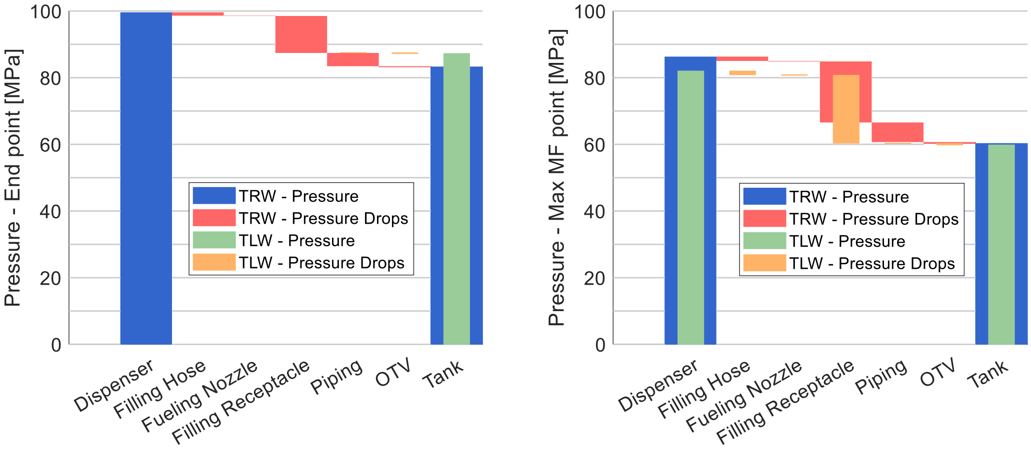

Figure 4.9 - Pressure drops calculation: example for type III tank, layout with 6 tanks.

As for the results obtained at the end of the refueling, the pressure measured in the dispenser (first column, 99.5 MPa) and the pressure drops calculated in the filling hose (0.792 MPa), in the fuelling nozzle (0.0984 MPa), in the filling receptacle (characterized by the highest losses, 11.08 MPa) are the same for all the tanks present in the layout. On the contrary, the pressure drops in the piping between the receptacle and the tank (3.98 MPa for the TRW and 0.0543 MPa for the TLW) and in the valve inside the tank (OTV, 0.31 MPa for the TRW and 0.227 MPa for the TLW) are different. These last values lead, as can also be seen graphically, to different results for the total pressure drops (16.27 MPa for the TRW and 12.26 MPa for the TLW). Consequently, the final pressures are 83.23 MPa (TRW) and 87.25 MPa (TLW). The pressure drops of the remaining tanks, relative to the case analysed, are to be considered in total terms included between the results obtained for the TLW and the TRW, just as the final pressure varies between the maximum obtained for TLW and the minimum relative to TRW. The elevated dispenser pressure is primarily due to the model forcing a full 100% SOC in each tank. In practice, such a target is rarely reached because safety mechanisms—such as valve limits and overpressure protections—typically restrict the maximum allowable pressure, preventing a complete fill.

To evaluate the pressure drops at the peak flowrate for each tank, the moment when the total dispenser mass flow rate reaches its maximum (around minute 8 and 10) was considered. Since each tank reaches its individual peak at slightly different times, the pressure values differ accordingly. In particular, the dispenser pressure varies from 86.21 MPa (TRW) to 82 MPa (TLW), while the corresponding tank pressures are 60.26 MPa and 59.82 MPa, respectively. This results in total pressure drops of 25.95 MPa for TRW and 22.18 MPa for TLW. In detail, the filling hose, fuelling nozzle and OTV show similar pressure drops (around 1.1 MPa, 0.148 MPa and 0.48 MPa respectively), while pressure drops in the filling receptacle and in the piping vary more. In fact, the former goes from 18.32 MPa (TRW) to 20.38 MPa (TLW), while the latter vary from 5.88 MPa (TRW) to 0.089 MPa. The total pressure drops of the remaining tanks are included between the maximum TRW value and the minimum TLW. Overall, these differences highlight that tanks are not filled uniformly, and pressure drops vary depending on tank position and flow path. As shown in the figure, the impact of leakage varies across components. The most significant losses occur at the receptacle, followed by the contributions from the piping. In contrast, leakage from the filling hose, nozzle, and on-tank valve (OTV) is comparatively minor.

The influence of input variations on the total pressure drops results is presented in Figure 4.10.

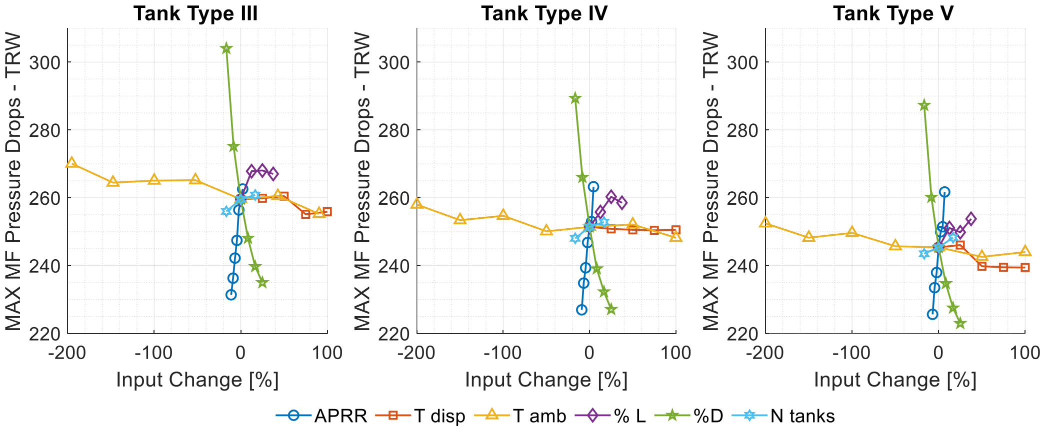

Figure 4.10 - Influence on the pressure drops for TRW by changing the inputs (all tank types, 6 tanks layout).

Since the pressure drops at the end of refueling are useful for calculating the final pressures but do not reflect the maximum values reached during the refueling, the sensitivity analysis was conducted considering only the point at which the losses are at their peak, or when the mass flow rate reaches its maximum. As in previous analyses, the tank with the highest losses (TRW) was selected as the reference case. As shown, pressure losses increase with decreasing ambient temperature and components diameter, as well as with increasing APRR, pipe length, and the number of tanks. For all other parameter variations, pressure losses tend to decrease. Overall, losses are highest for Type III tanks and progressively decrease for Type IV and Type V tanks. In particular, the losses due to dispenser temperature variation show a more linear behaviour for Type IV tanks compared to the others, while the losses associated with the variation in line length differ noticeably among the three tank types. As a result, the overall trends exhibit higher variability compared to the previous cases. This behaviour can be attributed to the fact that variations in input parameters affect the flow rate profiles, altering the timing of the peak values. Consequently, each data point in the graph corresponds to a different time step, in contrast to the earlier results, which were all extracted at the end of the simulation.

4.6 Comparative Analysis of Results

Table 4.5 shows the general trends of the sensitivity analysis results, similar for each type of tank as seen previously. The central column lists the input parameters that were varied from the baseline configuration, while the left and right columns show the corresponding trends in the results as each input decreases or increases, respectively. These trends are represented by arrows having the same directions as the curves in the graphs, with the numerical maximum or minimum value obtained indicated below. The coloured cells refer to the different tank types: green for Type III, orange for Type IV, and yellow for Type V. The input values and the related results obtained with the base case points are reported in Table 4.4. For both in percentage length and dispenser temperature variations, only increases from the base point were considered. Therefore, no values are reported on the left side of the corresponding columns.

Table 4.5 - Input and principal results – layout with 6 tanks.

Results variation for lower input					**INPUT**	**Results variation for higher input**				
p drops	**Disp. MF**	**Mean T**	**Final p**	**Ref. time**		**Ref. time**	**Final p**	**Mean T**	**Disp. MF**	**p drops**
MPa	g/s	°C	MPa	min		min	MPa	°C	g/s	MPa
↙	↙	↙	↙	↖	APRR	↘	↗	↗	↗	↗
22.6	195	68.6	85.6	11.1		10.3	88.3	75.9	220	26.3
					T disp	↖	↖	↖	↙	↙
						11.3	95	111	191	23.9
↖	↖	↙	↙	↙	T amb	↗	↗	↗	↘	↘
27	220	53.8	83.8	10.2		10.8	88.9	80.6	205.	24.2
					% L	↗	↗	↗	↘	↗
						10.8	89.1	74.3	205	26.8
↖	↙	↖	↖	↖	% D	↘	↘	↘	↗	↘
30.4	198	75.9	94.4	11.3		10.1	84.1	69.1	221.	22.3
↙	↙	↖	↙	↙	N tanks	↗	↗	↘	↗	↗
24.4	205	74.4	87.1	10.4		10.7	87.6	70.7	217	26.1

An increase in APRR compared to the baseline value for each tank type leads, as expected, to a reduction in refueling time and an increase in the mass flow rate delivered by the dispenser. However, this also results in higher pressure and temperature peaks, which must be carefully evaluated with respect to the SAE limits. Total pressure drops also increase.

Analysing the influence of temperatures, an increase in even just one of them leads to an increase in the values of the refueling time, the final pressure and the temperature, and should therefore be avoided, especially to comply with regulatory limits.

When considering percentage increases in pipe lengths and component diameters, their effects on the results are opposite. Specifically, increasing pipe length produces similar effects to a temperature rise (longer refueling times and higher final pressures and temperatures), while increasing diameters leads to higher mass flow rates, improving system performance by reducing pressure losses. However, larger diameters imply greater material and manufacturing costs and must also be compatible with the limited installation space available on board, which makes proper sizing a crucial design trade-off.

The removal of one tank from the layout, resulting in an increase in the volume of each single tank located behind the cabin, leads to a slight rise in internal tank temperature. This effect is not directly due to the change in the number of tanks, but rather to the associated changes in mass flow distribution and heat transfer conditions, such as reduced splitting of the flow and a larger surface area exposed to thermal exchange. Additionally, a lower overall system thermal inertia and longer refueling times for the larger tanks may also contribute to this effect. However, the increase remains within the SAE-compliant range. Moreover, the number of tanks is the parameter with the least influence on the overall results.

Summarizing the values that do not respect the pressure limit, as also visible from the results in red, values higher than the base value of dispenser temperature, ambient temperature, length and number of tanks, as well as smaller diameter values, must be excluded. To respect the temperature limit, however, it is sufficient not to consider values higher than the dispenser temperature (starting from the values indicated in Figure 4.7). Finally, given the results of the refueling time and the maximum flow rate delivered, the type III tank appears to be the one that best guarantees the desired results, even if the maximum flow rate obtained, 221.2 g/s, differs from the value of 300 g/s indicated in the SAE protocol and by [126]. Type III tank also guarantee lower values for pressure and temperature.

As shown, this study focused on evaluating the influence of individual parameters on the refueling process. However, it is acknowledged that several parameters are likely to interact in non-linear ways, and multivariate effects were not explicitly modelled in the current work. Based on the observed trends, a combination of high APRR and low ambient/dispenser temperatures would likely increase refueling speed and flow rate but would also raise final tank pressure and temperature, potentially exceeding safety thresholds unless counterbalanced by design factors such as increased component diameter or improved thermal dissipation. For example, increasing the line diameter improves flow rate without negatively affecting temperature or pressure, and could therefore help mitigate the thermal effects of a higher APRR. Similarly, optimizing the number of VTs or the layout could further influence dynamic pressure buildup and losses. These interdependencies are complex and merit a dedicated sensitivity or design study, which is planned as future work.

4.7 Results summary and conclusions

In this study, a customizable and dynamic model of a HSS for a generic heavy-duty vehicle has been developed, considering all components from the refueling dispenser to the onboard storage tanks. The model provides a flexible and customizable tool that reduces project development time, supports optimal sizing decisions (e.g., tank type and configuration), and ensures a complete, fast, and safe refueling process in compliance with SAE pressure and temperature limits.

A layout comprising 6 tanks (2 in the wheelbase area and 4 behind the cabin) was used as a reference configuration. Multiple simulations were conducted by varying the most significant input parameters (APRR, dispenser and ambient temperatures, pipe length and diameter, tank type and number) in order to identify configurations that minimize refueling time, while respecting pressure and temperature limits. Major pressure drops were also analysed and identified at the point of maximum inlet mass flow rate in each individual tank.

Based on the best performing conditions found for each tank type, a sensitivity analysis was performed with respect to the input parameters variation. The results showed better performance for Type III tanks, which exhibited shorter refueling times (10.11 min) and higher mass flow rates (221 g/s). These values, however, do not differ much from those found for Type IV and V tanks, with refueling times no greater than around one minute for the proposed values. In addition, Type III tanks are the heaviest among those proposed: this compromise must therefore be considered when choosing a tank. The influence of input variations was generally similar across the different tank types. Specifically, increasing APRR led to shorter refueling times; however, care must be taken to avoid exceeding SAE limits for pressure and temperature. Higher dispenser and ambient temperatures resulted in increased refueling times, pressures, and temperatures, and should therefore be avoided. Increasing pipe length produced effects similar to higher temperatures, while larger diameters led to improvements in refueling time, pressure, and temperature. Lastly, variations in the number of tanks compared to the original 6 tanks layout did not result in significant differences in system performance.

Conclusions

In today's context, characterized by a high percentage of emissions in the transport sector, this study proposed the dynamic modelling of HRS at 35 and 70 MPa in Matlab-Simulink, designed for refueling hydrogen heavy-duty vehicles according to the SAE J2601-5 protocol. Specifically, the 35 MPa HRS was studied under different operational scenarios: a parametric analysis, to identify the maximum number of possible refuelings by varying the APRR, and a more realistic simulation, based on the hydrogen demand of an urban bus fleet. To promote emission reductions in the sector, the integration of the 35 MPa HRS into a renewable microgrid was also analysed, with components optimized to limit costs while increasing the self-sufficiency rate of the entire system (HRS + microgrid). Three energy management strategies were proposed, modelled in Matlab, with increasing production and use of green hydrogen. Costs were subsequently adjusted through a techno-economic analysis, investigating the potential reduction in hydrogen production costs by considering both the sale of surplus electricity to the grid and the expected decrease in the specific cost of the hydrogen generator in the coming years. A further analysis was conducted regarding environmental sustainability, evaluating the reduction in CO_2 emissions for each proposed strategy and the emissions avoided through the use of hydrogen vehicles compared to the current diesel buses in the fleet considered. Regarding the 70 MPa investigation, a hydrogen storage system was modelled in Matlab-Simulink, considering all components from the dispenser to the vehicle tanks (pipes, elbows, etc.). By proposing different layout configurations (with varying numbers of tanks for the same hydrogen storage capacity) and different tank types, the impact on results was studied as a function of the main operational parameters.

In the first investigation, related to the modelling of the 35 MPa HRS, the results obtained by the parametric analysis showed optimized input parameters for increasing numbers of refuelings from 5 to 8, considering initially empty vehicles (SOC = 10%). The refueling times found ranged between 3.45 and 7.15 minutes, while tank pressure and temperature values complied with the SAE J2601-5 protocol. The realistic operation instead involved the modification of some input parameters according to the hydrogen demand of the bus fleet. The results, obtained from the most demanding refueling block, showed shorter refueling times (3÷4 minutes) and pressure and temperature values within limits for all days of the year, following a seasonal analysis. To achieve ambient temperature recovery after idle periods, a precooling temperature of -40°C must be considered, along with potential additional strategies during cold seasons, to prevent exceeding temperature limits in the long term.

The integration of the 35 MPa HRS into a renewable microgrid showed higher costs in the case of production exclusively from renewable sources (25.11 €/kg), for the same self-sufficiency level (100%). Considering mixed production, costs decreased to 23.49 €/kg, while with grid-only production the result was 12.94 €/kg.

The costs of the first two strategies were then adjusted: considering the higher selling price (0.137 €/kWh), costs decreased to 16.72 €/kg (Green EMS) and 16.98 €/kg (Mixed EMS). For the Green EMS, a parametric analysis was conducted varying the specific HG cost, with projections to 2030 and 2050. Results showed a cost reduction to 11.57 €/kg by 2050, assuming current electricity selling prices remain stable. This indicates that by 2050, renewable-based hydrogen production could become more cost-competitive than grid-based production, provided that HG cost projections are met and selling prices remain relatively stable. Currently, however, an additional cost of approximately 3.8 €/kg must be considered for production from renewable sources compared to grid-only production (with higher energy sales prices). In particular, PV dominates the TCI result, being characterized by the highest costs.

Regarding CO_2 emissions, the current fleet of 21 diesel buses is responsible for 36.84 kt CO_2/y. With FCEVs, the Green EMS generates minimal emissions, limited to grid electricity used for HRS components when renewable sources are insufficient. Higher emissions were observed for the Mixed EMS (up to 9.71 kt CO_2/y) and the Grid EMS, characterized by 16.7 kt CO_2/y. This means that even with grid-only hydrogen production, FCEV adoption would reduce emissions by 54.7%, while the Green EMS would achieve a 99.3% reduction.

Regarding the last investigation (70 MPa HSS), following the comparison between different layouts and tank types, the results showed better performance for Type III tanks, which exhibited shorter refueling times (10.11 min) and higher mass flow rates (221 g/s). These values, however, do not differ substantially from those found for Type IV and V tanks, with refueling time differences no greater than approximately one minute for the proposed configurations. Additionally, Type III tanks are the heaviest among those considered: this trade-off must therefore be considered when selecting a tank type. The influence of input parameter variations was generally similar across different tank types. Specifically, increasing APRR led to shorter refueling times; however, care must be taken to avoid exceeding SAE limits for pressure and temperature. Higher dispenser and ambient temperatures resulted in increased refueling times, pressures, and temperatures, and should therefore be avoided. Increasing pipe length produced effects similar to higher temperatures, while larger diameters led to improvements in refueling time, pressure, and temperature. Lastly, variations in the number of tanks compared to the original 6-tank layout did not result in significant differences in system performance.

In summary, this thesis demonstrated that:

- Each model is flexible and adaptable to different case studies;
- SAE J2601-5 pressure and temperature limits are consistently respected in all scenarios;
- Refueling times are aligned with current operational standards: 3-4 minutes for H_2 buses and 10 minutes for H_2 trucks, depending on onboard storage capacity;
- LCOH for green hydrogen production increases by 3.78 €/kg compared to grid-based production (considering higher prices for surplus energy sales);
- LCOH for green hydrogen production will become more competitive than grid-based production by 2050, considering the decrease in HG costs (with current energy selling prices);
- The replacement of current diesel buses with FCEVs leads to a 54.7% reduction in CO_2 emissions considering grid-based hydrogen production, while the percentage increases to 99.3% with renewable-based production;
- Type III tanks exhibit better performance compared to Type IV and V tanks, although they are characterized by greater weight;

- Variations in the number of onboard tanks do not significantly affect performance and internal tank thermodynamics.

Overall, the study presented demonstrates the feasibility and potential of integrating hydrogen refueling stations into renewable-based microgrids, providing valuable insights into both technical performance and economic viability. The developed dynamic models proved to be reliable tools for analysing complex hydrogen systems, accurately capturing the thermodynamic behaviour of components and adaptable to different configurations and operational strategies.

In addition to the techno-economic and environmental aspects, future research should address practical and safety-related considerations. In particular, further studies should investigate the management of transient conditions in the hydrogen transmission line and refueling systems, as well as the effects of repeated thermal and pressure cycles on material integrity. The implementation of advanced monitoring and control systems, based on predictive algorithms, could enhance operational safety, improve refueling efficiency, and extend component lifetimes. Furthermore, the study of hydrogen demand by different vehicles, both light and heavy, in the same HRS should be further investigated.

In conclusion, this research contributes to advancing the understanding of hydrogen infrastructure design and its interaction with renewable energy systems, offering a solid foundation for future studies and real-world implementations aimed at achieving a low-carbon, safe, and sustainable transport sector.

References

[1] Csalódi R, Czvetkó T, Sebestyén V, Abonyi J. Sectoral Analysis of Energy Transition Paths and Greenhouse Gas Emissions. Energies 2022, Vol 15, Page 7920 2022;15:7920. https://doi.org/10.3390/EN15217920.

[2] Filonchyk M, Peterson MP, Yan H, Gusev A, Zhang L, He Y, et al. Greenhouse gas emissions and reduction strategies for the world's largest greenhouse gas emitters. Science of The Total Environment 2024;944:173895. https://doi.org/10.1016/J.SCITOTENV.2024.173895.

[3] Lamb WF, Wiedmann T, Pongratz J, Andrew R, Crippa M, Olivier JGJ, et al. A review of trends and drivers of greenhouse gas emissions by sector from 1990 to 2018. Environmental Research Letters 2021;16:073005. https://doi.org/10.1088/1748-9326/ABEE4E.

[4] Intergovernmental Panel On Climate Change (IPCC). AR6 Synthesis Report: Climate Change 2023 — IPCC 2023. https://doi.org/10.59327/IPCC/AR6-9789291691647.

[5] United Nations. Kyoto Protocol To The United Nations Framework Convention On Climate Change 1998. https://unfccc.int/resource/docs/convkp/kpeng.pdf (accessed August 28, 2025).

[6] United Nations. The Paris Agreement 2016. https://unfccc.int/sites/default/files/resource/parisagreement_publication.pdf (accessed August 28, 2025).

[7] Conference of the Parties (COP) | UNFCCC n.d. https://unfccc.int/process/bodies/supreme-bodies/conference-of-the-parties-cop (accessed August 26, 2025).

[8] Crippa Monica, Guizzardi Diego, Pagani Federico, Banja Manjola, Muntean Marilena, Schaaf Edwin, et al. GHG emissions of all world countries 2024 2024:273. https://doi.org/doi:10.2760/4002897.

[9] Istituto superiore per la protezione e la ricerca ambientale (ISPRA). Emissioni totali di gas serra | Indicatori ambientali n.d. https://indicatoriambientali.isprambiente.it/it/pon/linea-2/emissioni-totali-di-gas-serra (accessed August 5, 2025).

[10] Istituto superiore per la protezione e la ricerca ambientale (ISPRA). Emissioni Di Gas A Effetto Serra Del Settore Energetico | Indicatori Ambientali n.d. https://indicatoriambientali.isprambiente.it/it/pon/linea-1/emissioni-di-gas-effetto-serra-del-settore-energetico (accessed August 6, 2025).

[11] Istituto superiore per la protezione e la ricerca ambientale (ISPRA). Emissioni Di Gas A Effetto Serra Da Trasporti | Indicatori Ambientali n.d. https://indicatoriambientali.isprambiente.it/it/pon/linea-1/emissioni-di-gas-effetto-serra-da-trasporti (accessed August 6, 2025).

[12] Istituto superiore per la protezione e la ricerca ambientale (ISPRA). Emissioni Di Gas A Effetto Serra In Agricoltura | Indicatori Ambientali n.d. https://indicatoriambientali.isprambiente.it/it/pon/linea-1/emissioni-di-gas-effetto-serra-agricoltura (accessed August 6, 2025).

[13] Intergovernmental Panel On Climate Change (IPCC). AR6 Climate Change 2022: Mitigation of Climate Change — IPCC 2022.

https://www.ipcc.ch/report/sixth-assessment-report-working-group-3/ (accessed June 18, 2025).

[14] Istituto superiore per la protezione e la ricerca ambientale (ISPRA). Le emissioni nazionali di gas serra Settore Trasporti-2023 Dipartimento per la valutazione, i controlli e la sostenibilità ambientale 2023. https://emissioni.sina.isprambiente.it/wp-content/uploads/2025/05/Emissioni-Trasporti-Anno-2023_def.pdf (accessed August 29, 2025).

[15] European Commission. The European Green Deal 2019. https://eur-lex.europa.eu/resource.html?uri=cellar:b828d165-1c22-11ea-8c1f-01aa75ed71a1.0002.02/DOC_1&format=PDF (accessed August 22, 2025).

[16] European Commission. REPowerEU Plan 2022. https://eur-lex.europa.eu/resource.html?uri=cellar:fc930f14-d7ae-11ec-a95f-01aa75ed71a1.0001.02/DOC_1&format=PDF (accessed August 22, 2025).

[17] European Investment Bank - EIB. EIB Board of Directors approves €12.8 billion new financing for transport, energy and business investment n.d. https://www.eib.org/en/press/all/2024-212-eib-board-of-directors-approves-eur12-8-billion-new-financing-for-transport-energy-and-business-investment (accessed August 22, 2025).

[18] Governo Italiano. PNRR: infrastrutture per una mobilità sostenibile n.d. https://www.governo.it/it/approfondimento/pnrr-infrastrutture-una-mobilit-sostenibile/16704 (accessed August 22, 2025).

[19] Pnrr: al Mims 62 miliardi di euro per mobilità, infrastrutture e logistica sostenibili, il 56% al Sud | Ministero delle infrastrutture e dei trasporti n.d. https://www.mit.gov.it/comunicazione/news/pnrr-al-mims-62-miliardi-di-euro-per-mobilita-infrastrutture-e-logistica?utm_source=chatgpt.com (accessed September 6, 2025).

[20] International Energy Agency. Energy Technology Perspectives 2020. https://iea.blob.core.windows.net/assets/7f8aed40-89af-4348-be19-c8a67df0b9ea/Energy_Technology_Perspectives_2020_PDF.pdf (accessed August 6, 2025).

[21] Global Fuel Economy Initiative. Trends In The Global Vehicle Fleet 2023 Managing The Suv Shift And The Ev Transition 2023. https://www.globalfueleconomy.org/media/na1pjian/gfei-trends-in-the-global-vehicle-fleet-2023-spreads.pdf (accessed August 22, 2025).

[22] European Automobile Manufacturers' Association (ACEA). Vehicles on European Roads 2024. https://www.acea.auto/files/ACEA-Report-Vehicles-on-European-roads-.pdf (accessed August 22, 2025).

[23] Gürbüz H. Analysis of the operating characteristics of hydrogen PEM fuel cell and battery onelectric vehicle in different driving cycles. Environ Prog Sustain Energy 2023;42:e14146. https://doi.org/10.1002/EP.14146.

[24] Pergamalis C, Tsampasis E, Dedes IC, Elias C. Hydrogen Fuel Cell Electrical Vehicles (FCEV) - Battery Electric Vehicles (BEV) - Comparison and Future Challenges. 2024 13th Mediterranean Conference on Embedded Computing, MECO 2024 2024. https://doi.org/10.1109/MECO62516.2024.10577907.

[25] Aguilar PA, Groß B. Battery Electric Vehicles and Fuel Cell Electric Vehicles, an Analysis of Alternative Powertrains as a Mean to Decarbonise

the Transport Sector. SSRN Electronic Journal 2022. https://doi.org/10.2139/SSRN.4112184.

[26] Alternative Fuels Data Center: All-Electric Vehicles n.d. https://afdc.energy.gov/vehicles/electric-basics-ev (accessed October 27, 2025).

[27] Alternative Fuels Data Center: How Do Fuel Cell Electric Vehicles Work Using Hydrogen? n.d. https://afdc.energy.gov/vehicles/how-do-fuel-cell-electric-cars-work (accessed October 27, 2025).

[28] International Energy Agency. Global Hydrogen Review 2024. https://iea.blob.core.windows.net/assets/89c1e382-dc59-46ca-aa47-9f7d41531ab5/GlobalHydrogenReview2024.pdf (accessed July 21, 2025).

[29] International Energy Agency. Global Electric Vehicles Outlook 2025. https://iea.blob.core.windows.net/assets/7ea38b60-3033-42a6-9589-71134f4229f4/GlobalEVOutlook2025.pdf (accessed July 21, 2025).

[30] Endiz MS. A Comparison of Battery and Hydrogen Fuel Cell Electric Vehicles for Clean Transportation. Orclever Proceedings of Research and Development 2023;2:10–7. https://doi.org/10.56038/OPRD.V2I1.230.

[31] De Wolf D, Smeers Y. Comparison of Battery Electric Vehicles and Fuel Cell Vehicles. World Electric Vehicle Journal 2023, Vol 14, Page 262 2023;14:262. https://doi.org/10.3390/WEVJ14090262.

[32] Guandalini G, Campanari S. Well-to-wheel driving cycle simulations for freight transportation: Battery and hydrogen fuel cell electric vehicles. 2018 International Conference of Electrical and Electronic Technologies for Automotive, AUTOMOTIVE 2018 2018. https://doi.org/10.23919/EETA.2018.8493216.

[33] Rivard E, Trudeau M, Zaghib K. Hydrogen Storage for Mobility: A Review. Materials 2019, Vol 12, Page 1973 2019;12:1973. https://doi.org/10.3390/MA12121973.

[34] Mulky L, Srivastava S, Lakshmi T, Sandadi ER, Gour S, Thomas NA, et al. An overview of hydrogen storage technologies – Key challenges and opportunities. Mater Chem Phys 2024;325:129710. https://doi.org/10.1016/J.MATCHEMPHYS.2024.129710.

[35] Ni M. An overview of hydrogen storage technologies. Energy Exploration and Exploitation 2006;24:197–209. https://doi.org/10.1260/014459806779367455;REQUESTEDJOURNAL:JOURNAL:EEAA.

[36] Mehr AS, Phillips AD, Brandon MP, Pryce MT, Carton JG. Recent challenges and development of technical and technoeconomic aspects for hydrogen storage, insights at different scales; A state of art review. Int J Hydrogen Energy 2024;70:786–815. https://doi.org/10.1016/J.IJHYDENE.2024.05.182.

[37] Bosu S, Rajamohan N. Recent advancements in hydrogen storage - Comparative review on methods, operating conditions and challenges. Int J Hydrogen Energy 2024;52:352–70. https://doi.org/10.1016/J.IJHYDENE.2023.01.344.

[38] Mark D. Allendorf RH. Assessment of tank designs for hydrogen storage on heavy duty vehicles using metal hydrides. Sandia Report 2023.

[39] Alenezi M, Alarbeed B, Alqaheem Y. METAL HYDRIDES AND METAL-ORGANIC FRAMEWORKS FOR HYDROGEN STORAGE IN AUTOMOTIVE APPLICATIONS: A REVIEW n.d. https://doi.org/10.32737/2221-8688-2024-1-76-94.

[40] Wang Q, Li J, Bu Y, Xu L, Ding Y, Hu Z, et al. Technical assessment and feasibility validation of liquid hydrogen storage and supply system for heavy-duty fuel cell truck. 2020 4th CAA International Conference on Vehicular Control and Intelligence, CVCI 2020 2020:555–60. https://doi.org/10.1109/CVCI51460.2020.9338639.

[41] Austin R. Baird EH, Brian D. Ehrhart AM. Liquid Hydrogen Heavy-Duty Vehicle Safety Review and Refueling Facility Design . Sandia Report 2022. https://www.osti.gov/servlets/purl/1885100/ (accessed August 23, 2025).

[42] Ahluwalia RK, Roh HS, Peng JK, Papadias D, Baird AR, Hecht ES, et al. Liquid hydrogen storage system for heavy duty trucks: Configuration, performance, cost, and safety. Int J Hydrogen Energy 2023;48:13308–23. https://doi.org/10.1016/J.IJHYDENE.2022.12.152.

[43] Ahluwalia RK, Peng JK, Roh HS, Papadias D, Wang X, Aceves SM. Liquid hydrogen storage system for heavy duty trucks: Capacity, dormancy, refueling, and discharge. Int J Hydrogen Energy 2023;48:34120–31. https://doi.org/10.1016/J.IJHYDENE.2023.05.113.

[44] Ha SK; KA, Araya S, Vincenzo L, Shin HK, Ha SK. A Review on the Cost Analysis of Hydrogen Gas Storage Tanks for Fuel Cell Vehicles. Energies 2023, Vol 16, Page 5233 2023;16:5233. https://doi.org/10.3390/EN16135233.

[45] Ma N, Zhao W, Wang W, Li X, Zhou H. Large scale of green hydrogen storage: Opportunities and challenges. Int J Hydrogen Energy 2024;50:379–96. https://doi.org/10.1016/J.IJHYDENE.2023.09.021.

[46] Klymyshyn NA, Brooks K, Barrett N. Methods for Estimating Hydrogen Fuel Tank Characteristics. Journal of Pressure Vessel Technology, Transactions of the ASME 2024;146. https://doi.org/10.1115/1.4063884/1169791.

[47] Jaber M, Yahya A, Arif AF, Jaber H, Alkhedher M. Burst pressure performance comparison of type V hydrogen tanks: Evaluating various shapes and materials. Int J Hydrogen Energy 2024;81:906–17. https://doi.org/10.1016/J.IJHYDENE.2024.07.315.

[48] Gómez JA;, Santos DMF, Salkuti R, Zhu D, Gómez JA, Santos DMF. The Status of On-Board Hydrogen Storage in Fuel Cell Electric Vehicles. Designs 2023, Vol 7, Page 97 2023;7:97. https://doi.org/10.3390/DESIGNS7040097.

[49] Sapre S, Pareek K, Vyas M. Investigation of structural stability of type IV compressed hydrogen storage tank during refueling of fuel cell vehicle. Energy Storage 2020;2:e150. https://doi.org/10.1002/EST2.150.

[50] Li M, Bai Y, Zhang C, Song Y, Jiang S, Grouset D, et al. Review on the research of hydrogen storage system fast refueling in fuel cell vehicle. Int J Hydrogen Energy 2019;44:10677–93. https://doi.org/10.1016/J.IJHYDENE.2019.02.208.

[51] Infinite Composites Pressure Vessels n.d. https://www.infinitecomposites.com/infinite-composite-pressure-vessels#APPS (accessed August 23, 2025).

[52] Mikroni M, Koutsoukis G, Vlachos D, Kostopoulos V, Vavouliotis A, Trakakis G, et al. Design, Analysis, and Testing of a Type V Composite Pressure Vessel for Hydrogen Storage. Polymers 2024, Vol 16, Page 3576 2024;16:3576. https://doi.org/10.3390/POLYM16243576.

[53] Couteau A, Dimopoulos Eggenschwiler P, Jenny P. Heat transfer analysis of high pressure hydrogen tank fillings. Int J Hydrogen Energy 2022;47:23060–9. https://doi.org/10.1016/J.IJHYDENE.2022.05.127.

[54] Oh SJ, Yoon JH, Jeon KS, Choi JJ. A numerical study on characteristics of heat transfer in hydrogen filling storage vessel by charging conditions. Int J Hydrogen Energy 2022;47:25679–95. https://doi.org/10.1016/J.IJHYDENE.2022.05.306.

[55] Bourgeois T, Ammouri F, Baraldi D, Moretto P. The temperature evolution in compressed gas filling processes: A review. Int J Hydrogen Energy 2018;43:2268–92. https://doi.org/10.1016/J.IJHYDENE.2017.11.068.

[56] Li JQ, Chen Y, Ma YB, Kwon JT, Xu H, Li JC. A study on the Joule-Thomson effect of during filling hydrogen in high pressure tank. Case Studies in Thermal Engineering 2023;41:102678. https://doi.org/10.1016/J.CSITE.2022.102678.

[57] Fragiacomo P, Martorelli M, Genovese M, Piraino F, Corigliano O. Thermodynamic modelling, testing and sensitive analysis of a directly pressurized hydrogen refuelling process with a compressor. Renew Energy 2024;226:120410. https://doi.org/10.1016/J.RENENE.2024.120410.

[58] Sgaramella A, Lo Basso G, de Santoli L. How the cylinder initial conditions affect the HCNG refuelling process - A thermodynamic analysis to determine the most effective filling parameters. Int J Hydrogen Energy 2024;51:559–75. https://doi.org/10.1016/J.IJHYDENE.2023.07.323.

[59] Sapre S, Vyas M, Pareek K. Impact of refueling parameters on storage density of compressed hydrogen storage Tank. Int J Hydrogen Energy 2021;46:16685–92. https://doi.org/10.1016/J.IJHYDENE.2020.08.136.

[60] High-Flow Prescriptive Fueling Protocols for Gaseous Hydrogen Powered Medium and Heavy-Duty Vehicles. SAE J2601/5_202402 2024. https://doi.org/10.4271/J2601/5_202402.

[61] Genovese M, Fragiacomo P. Hydrogen refueling station: Overview of the technological status and research enhancement. J Energy Storage 2023;61:106758. https://doi.org/10.1016/J.EST.2023.106758.

[62] Pratt J, Terlip D, Ainscough C, Kurtz J, Elgowainy A. H2FIRST Reference Station Design Task 2015. https://research-hub.nrel.gov/en/publications/h2first-reference-station-design-task-project-deliverable-2-2/ (accessed October 28, 2025).

[63] De Miguel N, Ortiz Cebolla R, Acosta B, Moretto P, Harskamp F, Bonato C. Compressed hydrogen tanks for on-board application: Thermal behaviour during cycling. Int J Hydrogen Energy 2015;40:6449–58. https://doi.org/10.1016/J.IJHYDENE.2015.03.035.

[64] Molkov V, Dadashzadeh M, Makarov D. Physical model of onboard hydrogen storage tank thermal behaviour during fuelling. Int J Hydrogen

Energy 2019;44:4374–84. https://doi.org/10.1016/J.IJHYDENE.2018.12.115.

[65] Deng S, Xiao J, Bénard P, Chahine R. Determining correlations between final hydrogen temperature and refueling parameters from experimental and numerical data. Int J Hydrogen Energy 2020;45:20525–34. https://doi.org/10.1016/J.IJHYDENE.2019.12.225.

[66] Liu J, Zheng S, Zhang Z, Zheng J, Zhao Y. Numerical study on the fast filling of on-bus gaseous hydrogen storage cylinder. Int J Hydrogen Energy 2020;45:9241–51. https://doi.org/10.1016/J.IJHYDENE.2020.01.033.

[67] Fragiacomo P, Martorelli M, Genovese M. Numerical modeling for analysis and improvement of hydrogen refueling process for heavy-duty vehicles. Appl Energy 2025;380:125092. https://doi.org/10.1016/J.APENERGY.2024.125092.

[68] Luo H, Xiao J, Bénard P, Yuan C, Tong L, Chahine R, et al. Thermodynamic modeling and analysis of cascade hydrogen refuelling with three-stage pressure and temperature for heavy-duty fuel cell vehicles. Int J Hydrogen Energy 2024;63:103–13. https://doi.org/10.1016/J.IJHYDENE.2024.03.060.

[69] Xiao J, Xu N, Cai W, Zhou X, Bénard P, Chahine R, et al. Thermodynamic and heat transfer models for refueling hydrogen vehicles: Formulation, validation and application. Int J Hydrogen Energy 2024;52:172–90. https://doi.org/10.1016/J.IJHYDENE.2023.06.081.

[70] Tun H, Reddi K, Elgowainy A, Poudel S. Thermodynamic parametric analysis of refueling heavy-duty hydrogen fuel-cell electric vehicles. Int J Hydrogen Energy 2023;48:28869–81. https://doi.org/10.1016/J.IJHYDENE.2023.04.075.

[71] Fragiacomo P, Martorelli M, Genovese M, Piraino F, Corigliano O. Thermodynamic modelling, testing and sensitive analysis of a directly pressurized hydrogen refuelling process with a compressor. Renew Energy 2024;226:120410. https://doi.org/10.1016/J.RENENE.2024.120410.

[72] Stops L, Siebe D, Stary A, Hamacher J, Sidarava V, Rehfeldt S, et al. Generalized thermodynamic modeling of hydrogen storage tanks for truck application. Cryogenics (Guildf) 2024;139:103826. https://doi.org/10.1016/J.CRYOGENICS.2024.103826.

[73] Saferna A, Saferna P, Kuczyński S, Łaciak M, Szurlej A, Włodek T. Effects of Hydrogen, Methane, and Their Blends on Rapid-Filling Process of High-Pressure Composite Tank. Energies 2024, Vol 17, Page 1130 2024;17:1130. https://doi.org/10.3390/EN17051130.

[74] Caponi R, Ferrario AM, Bocci E, Bødker S, del Zotto L. Single-tank storage versus multi-tank cascade system in hydrogen refueling stations for fuel cell buses. Int J Hydrogen Energy 2022;47:27633–45. https://doi.org/10.1016/J.IJHYDENE.2022.06.100.

[75] Galassi MC, Baraldi D, Acosta Iborra B, Moretto P. CFD analysis of fast filling scenarios for 70 MPa hydrogen type IV tanks. Int J Hydrogen Energy 2012;37:6886–92. https://doi.org/10.1016/J.IJHYDENE.2012.01.041.

[76] Li JQ, Li JCL, Park K, Kwon JT. Investigation on the changes of pressure and temperature in high pressure filling of hydrogen storage tank. Case

Studies in Thermal Engineering 2022;37:102143. https://doi.org/10.1016/J.CSITE.2022.102143.

[77] Hall C, Ramasamy V. Modelling the conjugate heat transfer during the fast-filling of high-pressure hydrogen vessels for vehicular transport. International Journal of Thermofluids 2024;21:100527. https://doi.org/10.1016/J.IJFT.2023.100527.

[78] Hossain Bhuiyan MM, Siddique Z. Hydrogen as an alternative fuel: A comprehensive review of challenges and opportunities in production, storage, and transportation. Int J Hydrogen Energy 2025;102:1026–44. https://doi.org/10.1016/J.IJHYDENE.2025.01.033.

[79] Grazieschi G, Zubaryeva A, Sparber W. Energy and greenhouse gases life cycle assessment of electric and hydrogen buses: A real-world case study in Bolzano Italy. Energy Reports 2023;9:6295–310. https://doi.org/10.1016/J.EGYR.2023.05.234.

[80] Fragiacomo P, Genovese M, Piraino F, Massari F, Boroomandnia M. Analysis of a distributed green hydrogen infrastructure designed to support the sustainable mobility of a heavy-duty fleet. Int J Hydrogen Energy 2024;51:576–94. https://doi.org/10.1016/J.IJHYDENE.2023.08.047.

[81] Okonkwo PC, Mansir IB, Barhoumi EM, Emori W, Radwan AB, Shakoor RA, et al. Utilization of renewable hybrid energy for refueling station in Al-Kharj, Saudi Arabia. Int J Hydrogen Energy 2022;47:22273–84. https://doi.org/10.1016/J.IJHYDENE.2022.05.040.

[82] Parsibenehkohal R, Jamil M, Khan AA. A multi-stage framework for coordinated scheduling of networked microgrids in active distribution systems with hydrogen refueling and charging stations. Int J Hydrogen Energy 2024;71:1442–55. https://doi.org/10.1016/J.IJHYDENE.2024.05.364.

[83] Ancona MA, Catena F, Ferrari F. Optimal design and management for hydrogen and renewables based hybrid storage micro-grids. Int J Hydrogen Energy 2023;48:20844–60. https://doi.org/10.1016/J.IJHYDENE.2022.10.204.

[84] Şafak B, Çiçek A. Multi-Objective Optimal Energy Management Strategy for Grid-Interactive Hydrogen Refueling Stations in Rural Areas. Sustainability 2025, Vol 17, Page 2663 2025;17:2663. https://doi.org/10.3390/SU17062663.

[85] Sun W, Harrison GP. Active Load Management of Hydrogen Refuelling Stations for Increasing the Grid Integration of Renewable Generation. IEEE Access 2021;9:101681–94. https://doi.org/10.1109/ACCESS.2021.3098161.

[86] Al-Sharafi A, Al-Buraiki AS, Al-Sulaiman F, Antar MA. Hydrogen refueling stations powered by hybrid PV/wind renewable energy systems: Techno-socio-economic assessment. Energy Conversion and Management: X 2024;22:100584. https://doi.org/10.1016/J.ECMX.2024.100584.

[87] Rizk-Allah RM, Hassan IA, Snasel V, Hassanien AE. An optimal standalone wind-photovoltaic power plant system for green hydrogen generation: Case study for hydrogen refueling station. Results in Engineering 2024;22:102234. https://doi.org/10.1016/J.RINENG.2024.102234.

[88] Di Micco S, Minutillo M, Perna A, Jannelli E. On-site solar powered refueling stations for green hydrogen production and distribution: performances and costs. E3S Web of Conferences 2022;334:01005. https://doi.org/10.1051/E3SCONF/202233401005.

[89] Barhoumi EM, Okonkwo PC, Ben Belgacem I, Zghaibeh M, Tlili I. Optimal sizing of photovoltaic systems based green hydrogen refueling stations case study Oman. Int J Hydrogen Energy 2022;47:31964–73. https://doi.org/10.1016/J.IJHYDENE.2022.07.140.

[90] Bahou S. Techno-economic assessment of a hydrogen refuelling station powered by an on-grid photovoltaic solar system: A case study in Morocco. Int J Hydrogen Energy 2023;48:23363–72. https://doi.org/10.1016/J.IJHYDENE.2023.03.220.

[91] Hussain S, Daneshmand SV, Zareipour H, Layzell D, Khan A. Optimal Sizing of a Stand-alone Renewable-Powered Hydrogen Fueling Station. 2022 IEEE International Autumn Meeting on Power, Electronics and Computing, ROPEC 2022 2022. https://doi.org/10.1109/ROPEC55836.2022.10018821.

[92] Kavadias KA, Kosmas V, Tzelepis S. Sizing, Optimization, and Financial Analysis of a Green Hydrogen Refueling Station in Remote Regions. Energies 2022, Vol 15, Page 547 2022;15:547. https://doi.org/10.3390/EN15020547.

[93] Gu Y, Chen Q, Xue J, Tang Z, Sun Y, Wu Q. Comparative techno-economic study of solar energy integrated hydrogen supply pathways for hydrogen refueling stations in China. Energy Convers Manag 2020;223:113240. https://doi.org/10.1016/J.ENCONMAN.2020.113240.

[94] Tang O, Rehme J, Cerin P. Levelized cost of hydrogen for refueling stations with solar PV and wind in Sweden: On-grid or off-grid? Energy 2022;241:122906. https://doi.org/10.1016/J.ENERGY.2021.122906.

[95] HyCentA Research GmbH | Wasserstoff als Lösung für Energiespeicher n.d. https://www.hycenta.at/ (accessed September 5, 2025).

[96] Klopčič N, Regenfelder R, Hafner T, Winkler F, Rasche C, Rink M, et al. Refuelling tests of a hydrogen tank for heavy-duty applications. Int J Hydrogen Energy 2024;49:1237–49. https://doi.org/10.1016/J.IJHYDENE.2023.09.109.

[97] Bell IH, Wronski J, Quoilin S, Lemort V. Pure and Pseudo-pure Fluid Thermophysical Property Evaluation and the Open-Source Thermophysical Property Library CoolProp 2014. https://doi.org/10.1021/ie4033999.

[98] Tatti R, Klopčič N, Radner F, Petrollese M. Thermodynamic Modelling And Analysis Of A Hydrogen Refueling Station Using Matlab-Simulink. 38th International Conference On Efficiency, Cost, Optimization, Simulation And Environmental Impact Of Energy Systems (ECOS)) 2025;29.

[99] Xiao J, Bénard P, Chahine R. Estimation of final hydrogen temperature from refueling parameters. Int J Hydrogen Energy 2017;42:7521–8. https://doi.org/10.1016/J.IJHYDENE.2016.05.213.

[100] Baglioni Group. Hydrogen - Baglioni Group Products n.d. https://baglionispa.com/en/hydrogen/# (accessed September 8, 2025).

[101] Safra Group. HYCITY ®: Hydrogen bus - Safra n.d. https://safra.fr/en/hycity-2/ (accessed September 3, 2025).

[102] Rothuizen E, Rokni M. Optimization of the overall energy consumption in cascade fueling stations for hydrogen vehicles. Int J Hydrogen Energy 2014;39:582–92. https://doi.org/10.1016/J.IJHYDENE.2013.10.066.

[103] Caponi R, Ferrario AM, Bocci E, Bødker S, del Zotto L. Single-tank storage versus multi-tank cascade system in hydrogen refueling stations for fuel cell buses. Int J Hydrogen Energy 2022;47:27633–45. https://doi.org/10.1016/J.IJHYDENE.2022.06.100.

[104] Xiao L, Chen J, Wu Y, Zhang W, Ye J, Shao S, et al. Effects of pressure levels in three-cascade storage system on the overall energy consumption in the hydrogen refueling station. Int J Hydrogen Energy 2021;46:31334–45. https://doi.org/10.1016/J.IJHYDENE.2021.07.007.

[105] Manoharan Y, Hosseini SE, Butler B, Alzhahrani H, Senior BTF, Ashuri T, et al. Hydrogen Fuel Cell Vehicles; Current Status and Future Prospect. Applied Sciences 2019, Vol 9, Page 2296 2019;9:2296. https://doi.org/10.3390/APP9112296.

[106] American Petroleum Institute. Reciprocating Compressors for Petroleum, Chemical, and Gas Industry Services 2007. https://myprecise.petronas.com/eForms/sparta/SKG%2012/API%20618%202016.pdf (accessed September 8, 2025).

[107] Smith R. Chemical Process - Design and Integration 2005. https://archive.org/details/chemicalprocessd0000smit_f5r6 (accessed September 8, 2025).

[108] Poudel S, Tun H, Reddi K, Elgowainy A. Investigation of precooling unit design options in hydrogen refueling station for heavy-duty fuel-cell electric vehicles. Int J Hydrogen Energy 2024;61:493–502. https://doi.org/10.1016/J.IJHYDENE.2024.02.197.

[109] Hyundai launches hydrogen bus with 960 km of range | HyBus n.d. https://hybus.eu/hyundai-launches-hydrogen-bus-with-960-km-of-range/ (accessed October 5, 2025).

[110] Tatti R, Petrollese M, Cau G. TECHNO-ECONOMIC ANALYSIS AND OPTIMIZATION OF A HYDROGEN REFUELING STATION INTEGRATED IN A RENEWABLE-BASED MICROGRID. n.d. https://doi.org/10.52202/077185-0008.

[111] Cengel Y.A., Ghajar A. J. Heat and Mass Transfer: Fundamentals and Applications. 5th ed. 2015.

[112] Meteonorm n.d. https://meteonorm.com/en/ (accessed October 15, 2025).

[113] SunPower Maxeon 3 Home Solar Panel More Lifetime Energy Uncompromising Durability n.d. www.sunpower.maxeon.com/int/PVInstallGuideIEC. (accessed October 15, 2025).

[114] Duffie JA, Beckman WA. Solar Engineering of Thermal Processes: Fourth Edition. Solar Engineering of Thermal Processes: Fourth Edition 2013. https://doi.org/10.1002/9781118671603.

[115] Serra F, Lucariello M, Petrollese M, Cau G. Optimal Integration of Hydrogen-Based Energy Storage Systems in Photovoltaic Microgrids: A Techno-Economic Assessment. Energies 2020, Vol 13, Page 4149 2020;13:4149. https://doi.org/10.3390/EN13164149.

[116] Micena RP, Llerena-Pizarro OR, de Souza TM, Silveira JL. Solar-powered Hydrogen Refueling Stations: A techno-economic analysis. Int J Hydrogen Energy 2020;45:2308–18. https://doi.org/10.1016/J.IJHYDENE.2019.11.092.

[117] Elgowainy A, Reddi K, Lee DY, Rustagi N, Gupta E. Techno-economic and thermodynamic analysis of pre-cooling systems at gaseous hydrogen refueling stations. Int J Hydrogen Energy 2017;42:29067–79. https://doi.org/10.1016/J.IJHYDENE.2017.09.087.

[118] MATLAB gamultiobj - Find Pareto front of multiple fitness functions using genetic algorithm n.d. https://uk.mathworks.com/help/gads/gamultiobj.html (accessed October 30, 2025).

[119] Pagamenti Ritiro Dedicato: calcolo, fatture e dichiarazioni fiscali n.d. https://www.gse.it/servizi-per-te/fotovoltaico/ritiro-dedicato/regolazione-economica-del-servizio#consultare (accessed October 10, 2025).

[120] GSE. Prezzi medi mensili per fascia oraria e zona di mercato 2025.

[121] Reksten AH, Thomassen MS, Møller-Holst S, Sundseth K. Projecting the future cost of PEM and alkaline water electrolysers; a CAPEX model including electrolyser plant size and technology development. Int J Hydrogen Energy 2022;47:38106–13. https://doi.org/10.1016/J.IJHYDENE.2022.08.306.

[122] IRENA. Green Hydrogen Cost Reduction: Scaling up Electrolysers to Meet the 1.5^{0}C Climate Goal, International Renewable Energy Agency. Irena 2020:105. https://www.irena.org/publications/2020/Dec/Green-hydrogen-cost-reduction (accessed October 9, 2025).

[123] Dati Statistici della generazione | Dati Terna Driving Energy n.d. https://dati.terna.it/generazione/dati-statistici#produzione/lorda-emissioni (accessed October 14, 2025).

[124] Bhandari R, Shah RR. Hydrogen as energy carrier: Techno-economic assessment of decentralized hydrogen production in Germany. Renew Energy 2021;177:915–31. https://doi.org/10.1016/J.RENENE.2021.05.149.

[125] Future costs of hydrogen: a quantitative review - Sustainable Energy & Fuels (RSC Publishing) DOI:10.1039/D4SE00137K n.d. https://pubs.rsc.org/en/content/articlehtml/2024/se/d4se00137k (accessed October 14, 2025).

[126] Public information on the Horizon Europe RHeaDHy project n.d. https://rheadhy.eu/ (accessed October 15, 2025).

[127] Zhu XK, Wiersma B, Johnson WR, Sindelar R. Burst Pressure Solutions of Thin and Thick-Walled Cylindrical Vessels. J Press Vessel Technol 2023;145. https://doi.org/10.1115/1.4062334.

[128] Klopčič N, Esser K, Rauh JF, Sartory M, Trattner A. Modelling hydrogen storage and filling systems: A dynamic and customizable toolkit. Int J Hydrogen Energy 2024;49:1180–95. https://doi.org/10.1016/J.IJHYDENE.2023.08.036.

[129] Sapre S, Vyas M, Pareek K. Impact of refueling parameters on storage density of compressed hydrogen storage Tank. Int J Hydrogen Energy 2021;46:16685–92. https://doi.org/10.1016/J.IJHYDENE.2020.08.136.